NASA CR-134620

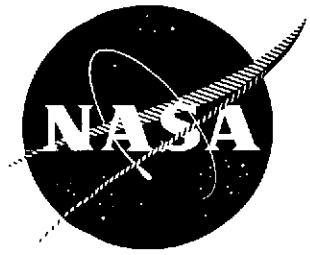

AN INVESTION OF THE OPEN-LOOP AMPLIFICATION OF A REYNOLDS NUMBER DEPENDENT PROCESS BY WAVE DISTORTION

by

Marie B. Ventrice and Kenneth R. Purdy

Department of Mechanical Engineering
Tennessee Technological University
Cookeville, Tennessee 38501

prepared for

NATIONAL AERONAUTICS AND SPACE ADMINISTRATION

NASA Lewis Research Center
Contract NGR 43-003-015
Richard J. Priem, Project Manager

1. Report No.	2. Government Accession No.	3. Recipient's Catalog No.
CR-134620		

4. Title and Subtitle	5. Report Date
AN INVESTIGATION OF THE OPEN-LOOP AMPLIFICATION OF A REYNOLDS NUMBER DEPENDENT PROCESS BY WAVE DISTORTION	May 1974
	6. Performing Organization Code

7. Author(s)	8. Performing Organization Report No.
Marie B. Ventrice and Kenneth R. Purdy	
	10. Work Unit No.

9. Performing Organization Name and Address	11. Contract or Grant No.
Department of Mechanical Engineering Tennessee Technological University Cookeville, Tennessee 38501	NGR 43-003-015
	13. Type of Report and Period Covered
12. Sponsoring Agency Name and Address	Contractor Report June 1973 - Dec. 1973
National Aeronautics and Space Administration Washington, D. C. 20546	14. Sponsoring Agency Code

15. Supplementary Notes

Project Manager, Richard J. Priem, Chemical Propulsion Division, NASA Lewis Research Center, Cleveland, Ohio

16. Abstract

The response of a constant-temperature hot-wire anemometer to sinusoidal and distorted sinusoidal acoustic oscillations is examined. The output of the anemometer is dependent upon the Reynolds number of the flow over the wire. The response is a measure of the interaction between the anemometer output and the acoustic pressure in the neighborhood of the wire. It is an open-loop prediction of the characteristics of actual closed-loop operation of a system. If the open-loop response is large enough, unstable closed-loop operation is predicted.

The study was motivated by a need to investigate the stability limits of liquid-propellant rockets when perturbed by pressure oscillations. This is a very difficult process to study experimentally. The combustion process in a liquid-propellant rocket can be modeled as being Reynolds number dependent. The sinusoidal and distorted sinusoidal acoustic oscillations used for this study are the same as those characteristic of unstable rocket combustion.

Both an analytical and an experimental study of the anemometer's response was performed. Qualitatively, the results of each are similar--the response of the system to pure sinusoidal acoustic vibration of the fluid surrounding the wire is small, even when the magnitude of the acoustic pressure is quite large; but the response can be increased by as much as an order of magnitude with respect to the sinusoidal case by the addition of distortion. The amplitude and phase of the distortion component, relative to the fundamental component, are the dominant factors in the increase in the response.

17. Key Words (Suggested by Author(s))	18. Distribution Statement
Combustion instability Resonance Acoustics Nonlinear response	Unclassified - Unlimited

19. Security Classif. (of this report)	20. Security Classif. (of this page)	21. No. of Pages	22. Price*
Unclassified	Unclassified	181	12.25

* For sale by the National Technical Information Service, Springfield, Virginia 22151

FOREWORD

This report is a semi-annual status report covering research conducted during the six-month period ending December 31, 1973. The investigations described herein were sponsored by the National Aeronautics and Space Administration, Lewis Research Center, Cleveland, Ohio 44135, under grant NGR 43-003-015. It was administered under the technical cognizance of Dr. Richard J. Priem, Head of the Rocket Combustion Section. Dr. Priem's interest in the work is deeply appreciated.

The work is the doctoral research of Marie B. Ventrice and was conducted under the supervision of Dr. Kenneth R. Purdy, the principal investigator. The research was initiated in January 1972 -- the starting date of the NASA grant -- and was guided during the first eight months by Dr. Allan E. Hribar, the grant's original principal investigator.

Support was also given to the project by the Department of Mechanical Engineering of Tennessee Technological University. In addition to the authors, Jih-Chin Fang, Graduate Instructor in the Department of Mechanical Engineering at Tennessee Tech, has made many valuable contributions to this research.

ABSTRACT

The response of a constant-temperature hot-wire anemometer to sinusoidal and distorted sinusoidal acoustic oscillations is examined. The output of the anemometer is dependent upon the Reynolds number of the flow over the wire. The response is a measure of the interaction between the anemometer output and the acoustic pressure in the neighborhood of the wire. It is an open-loop prediction of the characteristics of actual closed-loop operation of a system. If the open-loop response is large enough, unstable closed-loop operation is predicted.

The study was motivated by a need to investigate the stability limits of liquid-propellant rockets when perturbed by pressure oscillations. This is a very difficult process to study experimentally. The combustion process in a liquid-propellant rocket can be modeled as being Reynolds number dependent. The sinusoidal and distorted sinusoidal acoustic oscillations used for this study are the same as those characteristic of unstable rocket combustion.

Both an analytical and an experimental study of the anemometer's response was performed. Qualitatively, the results of each are similar--the response of the system to pure sinusoidal acoustic vibration of the fluid surrounding the wire is small, even when the magnitude of the acoustic pressure is quite large; but the response can be increased by as much as an order of magnitude with respect to the sinusoidal case

by the addition of distortion. The amplitude and phase of the distortion component, relative to the fundamental component, are the dominant factors in the increase in the response.

TABLE OF CONTENTS

Chapter Page

Chapter Page

LIST OF FIGURES

Figure Page

Figure Page

Figure Page

LIST OF TABLES

NOMENCLATURE

A_w	hot-wire surface area
A, B, N	dimensionless hot-wire constants
$\hat{A}$, $\hat{B}$, $\hat{C}$	functions defined by (16)
A,B,C,D,F,G	constants
b	constant
c_∞	speed of sound at T_∞
c_1	constant
D	diameter of test section
D_w	hot-wire diameter
E	hot-wire bridge voltage
$\hat{E}$	total energy
h	heat transfer coefficient
H	pressure analog voltage
I	hot-wire current
K	hot-wire sensitivity to flow parallel to its axis
k	thermal conductivity of air or wave number
k_r	radial wave number, $k_r = \alpha_{mn}\pi/R$
k_z	longitudinal wave number, $k_z = n_z\pi/L$
L	length of test section
L_w	hot-wire length
m	Reynolds number exponent for burning
M	wire Mach number
m	tangential mode number (integer)

Nu	Nusselt number (hD_w/k)
n	radial mode number (integer)
n_z	longitudinal mode number (integer)
P	local air pressure
$\hat{P}$	maximum value of time-dependent component of pressure
P_∞	ambient air pressure
P'_{rms}	rms pressure amplitude $\left[\frac{1}{2} \sum_{n=1}^{\infty} p_n^2\right]^{0.5} P_\infty$
p_n	harmonic pressure perturbation coefficient
Q	heat
R	correlation coefficient or cylinder radius
R_a	gas constant for air
R_g	gas constant
R_{cbl}	cable resistance
Re	Reynolds number ($\rho VD/\mu$)
R_p	probe resistance
R_s	standard resistance
R_w	hot-wire resistance at T_w
R_∞	hot-wire resistance at T_∞
R_{nl}	nonlinear in-phase response factor
S	entropy
T	local air temperature
T_f	film temperature, $[T_w + T]/2$
T_∞	ambient air temperature
T_n	harmonic temperature perturbation coefficient
T_o	reference temperature, 0°C
T_w	hot-wire temperature

t	time
U	relative drop velocity
u,v,w	cartesian components of velocity (x,y,z)
u_{ℓ}	axial drop velocity
V	velocity
V_c	wire cooling velocity, $[(u')^2 + (Kv')^2 + (\overline{w} + w')^2]^{0.5}$
v_θ, v_r, v_z	cylindrical conponents of velocity
v_n	harmonic transverse air velocity coefficient
v_t	transverse air velocity
W	work
w	burning rate
x,y,z	cartesian coordinates
$\theta,r,z,$	cylindrical coordinates

Greek Symbols

α	hot-wire resistance
$\hat{\alpha}$	hot-wire angle of inclination to radius vector
α_{n0}	eigen value
$\alpha_{mn}\pi$	eigen values of equation (A.34)
β	general property or an arbitrary phase angle
γ	ratio of specific heats
Γ,Υ,Ω	functions
θ_n	harmonic phase angle for velocity-pressure relation
ρ	air density
$\hat{\rho}$	maximum value of time-dependent component of density
ρ_n	harmonic density perturbation coefficient
ϕ_n	harmonic phase angle for pressure perturbation

μ	viscosity
ω	radian frequency

Superscripts and Overmarks

'	time-dependent component
—	time-mean component
~	dimensionless property
→	vector
^	distinguishes between constants

Subscripts

f	evaluated at the film temperature
o	value at $T = T_o = 0°C$
σ	without oscillations
∞	undisturbed value
1	evaluated at 1 m/sec

Chapter 1

INTRODUCTION AND BACKGROUND

INTRODUCTION

The need exists for a more accurate understanding of the nonlinear instability limits of rocket engines. These limits are currently one of the least understood properties of combustion instability. The causes of instability and the factors determining the instability limits are of major importance to the design of high performance rocket engines.

Setting

Steady combustion in liquid propellant rockets is assumed to be vaporization limited -- a velocity sensitive or Reynolds number dependent process. Priem and Heidmann [1] have shown that quantitative agreement exists between theory and experiment for this mode. Vaporization limited combustion is also expected for unstable combustion and this has been qualitatively confirmed.

Recently, Heidmann [2, 3] has shown analytically that distorted acoustic oscillations affect the open-loop response of vaporization limited combustion. The open-loop response is a prediction of the stability of the process during closed-loop operation; it indicates whether the acoustic gains of the system are sufficient to overcome the acoustic losses and cause instability. Response factors that were an order of magnitude greater than those obtained for pure sinusoidal

excitation were found for some conditions, and these response factors were high enough that unstable combustion was definitely predicted.

The validity of Heidmann's results has not been tested experimentally due to the difficulties associated with making measurements in a burning rocket, the very short period between the onset of instability and the destruction of the rocket and the concomitant existence of many other uncontrolled variables.

For the vaporization model used in references [2] and [3] it was assumed that the burning rate was proportional to the drop Reynolds number raised in a power. Such a model is characteristic of other processes such as those involving convective heat and mass transfer; hence, it appears that the same type of analysis could be performed for these processes.

Scope

In an effort to extend the significance of Heidmann's analysis and to confirm the results experimentally, another Reynolds number dependent process was selected and analyzed in the same manner as that done by Heidmann, and an experimental system was designed and used to test the results. The choice of the analogous process was primarily influenced by its amenability to experimental investigations. To facilitate comparison both the analytical and experimental studies, the imposed acoustic oscillations were the same type as those used by Heidmann -- pure sinusoidal and distorted sinusoidal spinning transverse acoustic oscillations. Heidmann was particularly interested in the distorted sinusoidal oscillations since they are the most frequently encountered mode of unstable combustion [3]. Variations in the overall intensity and the proportion and phase angle of the distortion component

were considered. In addition, changes in the through-flow velocity were considered analytically but not experimentally. The open-loop results were then used to assess some of the conditions and mechanisms necessary for sustained closed-loop operation. In both Heidmann's analysis and this analysis, it was desired to see if the addition of distortion to sinusoidal acoustic perturbations of the Reynolds number dependent process involved would increase the response and drive the process to instability.

BACKGROUND

There has been considerable interest in studies of rocket combustion instability, expecially by NASA and the military. Combustion instability has been a problem to all modern rocket engine development programs from the German V-2's to the present [4]. At this time there is no way of reliably predicting whether or not a rocket design will be stable or unstable before actually building and testing it. Sometimes during the operation of a developmental rocket the system will become unstable. Vibrations build up which, if allowed to continue, could destroy the rocket. These vibrations are easily detected by the loud screeching or screaming noise generated.

Retrospect

Up to the present time, the design procedure has been to create a rocket which is predicted to give the desired performance, then to test it to see if it will operate stably. If it does not, various modifications are available which may be able to create stability. The primary methods are the insertion of baffles or acoustic liners into the combustion chamber [5]. These devices may damp out the generated vibrations

or prevent them from occurring at all; however, they may also have other effects on engine performance which may not be desirable.

Many types of tests are used to check a new design. Scale model testing can be done; however, results from these tests are not always reliable. Sometimes the small model will be stable but the full-sized version will not be, and vice-versa. Static tests are also used in which the rocket engine is held stationary during operation while small explosions are set off inside the combustion chamber. In most cases the engine will remain stable up to a particular level of explosion, and self-sustained vibrations are triggered above that. These results again are not completely reliable. Sometimes low level explosions will trigger instability when more powerful ones will not. The type of explosion and its location also affect the results [3]. Hence, the only reliable way to determine stability is to actually flight test the full scale model. Since NASA sometimes has a human payload, the need exists to get as close to absolute reliability as possible. This becomes very expensive in both time and money; it would therefore be very desirable to develop some insight into why instabilities occur so they can be avoided.

To try to better understand the causes of instabilities and the effects of various design parameters on them, many different types of studies have been initiated. These studies include the combustion process itself, the means and rate of fuel vaporization, the methods of injecting fuel and oxidizer into a liquid propellant system, the effect of the shape of solid fuel, the fuel/oxidizer ratio, the effect of nozzle configuration, the relative dimensions, and many others. Attempts have also been made to write the governing equations for the processes

inside a rocket; however, the system is so complex that no method has been satisfactory [6].

An approach to an understanding of the problem is suggested in some of Lord Rayleigh's work, which was originally published in 1878. He said that if an oscillatory heat source had a component of its rate in phase with an acoustic oscillation, the acoustic oscillation would be amplified [7]. This statement, coupled with the observation that certain definite patterns of vibration occur during instability, leads to a study of the interaction of the combustion process and the natural acoustic modes of vibration of the system.

A liquid propellant rocket combustion chamber is basically a closed-ended cylinder through which a flow can pass. There are small holes in one end of the chamber for the injection of liquid fuel and oxidizer. At the opposite end of the chamber there is a nozzle through which the gases resulting from combustion pass out of the system. The nozzle is supersonic so that what goes on downstream of the throat section does not affect the chamber; however, there is a coupling between the nozzle and the chamber. Because of a rocket's close similarity to a closed-ended cylinder, this configuration has been used in this investigation.

Inviscid Acoustic Fields of a Cylindrical Enclosure

A knowledge of the characteristics of the solution of the inviscid wave equation for a cylindrical enclosure is necessary to an understanding of both the theoretical and experimental analysis. The assumptions, boundary conditions, equations and details of the solution are given in Appendix A. The solution is a modification of the presentations given in references [8] and [9].

The solution yields the frequencies of the natural modes of vibration of a closed-ended cylinder and determines the equations for the pressure, velocity, and density variations when excited at these frequencies. The equations show that there are three basic modes of vibration, each having an infinite number of permissible resonant frequencies. Also, one of these modes can occur in either of two ways -- as a standing wave or as a spinning wave. Combination modes are also possible.

The pressure, velocity and density can each be expressed as the sum of a time-mean and a time-dependent component

$$\begin{aligned} P(r,\theta,z,t) &= \bar{P}(r,\theta,z) + P'(r,\theta,z,t) \\ \vec{V}(r,\theta,z,t) &= \bar{\vec{V}}(r,\theta,z) + \vec{V}'(r,\theta,z,t) \\ \rho(r,\theta,z,t) &= \bar{\rho}(r,\theta,z) + \rho'(r,\theta,z,t) \end{aligned} \qquad (A.7)$$

where the bar superscript denotes the time-mean value and the prime denotes the deviation from the mean value. From Appendix A the equations for the time-dependent components of pressure, velocity, and density are

$$P'_{mnn_z} = \hat{P}'_{mnn_z} \frac{J_m(\alpha_{mn}\pi r/R)}{J_m(\alpha_{mn}\pi)} \cos(n_z\pi z/L)\cos(m\theta)\sin(\omega_{mnn_z}t + \beta_{mnn_z}) \qquad (A.44a)$$

$$V'_{r_{mnn_z}} = \frac{\hat{P}_{mnn_z}\alpha_{mn}\pi J'_m(\alpha_{mn}\pi r/R)}{\rho_\infty \omega_{mnn_z} R} \frac{}{J_m(\alpha_{mn}\pi)} \cos(n_z\pi z/L)\cos(m\theta)\cos(\omega_{mnn_z}t+\beta_{mnn_z}) \qquad (A.44b)$$

$$V'_{\theta_{mnn_z}} = -\frac{\hat{P}_{mnn_z} m}{\rho_\infty \omega_{mnn_z} r} \frac{J_m(\alpha_{mn}\pi r/R)}{J_m(\alpha_{mn}\pi)} \cos(n_z\pi z/L)\sin(m\theta)\cos(\omega_{mnn_z}t+\beta_{mnn_z}) \qquad (A.44c)$$

$$V'_{z_{mnn_z}} = -\frac{\hat{P}_{mnn_z} n_z\pi}{\rho_\infty \omega_{mnn_z} L} \frac{J_m(\alpha_{mn}\pi r/R)}{J_m(\alpha_{mn}\pi)} \sin(n_z\pi z/L)\cos(m\theta)\cos(\omega_{mnn_z}t+\beta_{mnn_z}) \qquad (A.44d)$$

$$\rho'_{mnn_z} = \frac{\hat{P}_{mnn_z} J_m(\alpha_{mn}\pi r/R)}{c_\infty^2 \, J_m(\alpha_{mn}\pi)} \cos(n_z \pi z/L)\cos(m\theta)\cos(\omega_{mnn_z} t + \beta_{mnn_z}) \qquad (A.44e)$$

The first pure mode of vibration is a longitudinal type for which m and n are zero. The resonant frequencies of this mode are whole multiples of the fundamental frequency of this mode. The pressure and velocity distributions for the first three resonant frequencies at quarter cycle intervals of time are shown in figure 1. The drawings above the pressure distributions combine the pressure and velocity into one picture. The denser the dots, the greater the pressure and density of the gas. The arrows indicate the net motion of the molecules in both direction and magnitude. Both the pressure and velocity vary sinusoidally along the length of the chamber, but are ninety degrees out of phase with each other in time and space. There is no variation in pressure or velocity either radially or tangentially.

The next two modes of vibration are transverse types where the variations in pressure and velocity can occur tangentially and/or radially but not longitudinally. The resonant frequencies of these modes are not whole multiples of a fundamental. The frequencies are in part determined by the zeros of a Bessel function, which is not a true periodic function.

The first transverse type is a pure radial mode; there is no tangential variation in pressure or velocity. For this mode m and n_z are zero. The pressure distributions at $\omega t = 0$ and π for the first three radial modes are shown in figure 2. The radial variation in pressure is a first order Bessel function; the variation with time at a particular location is sinusoidal. Figure 3 includes the velocity distribution

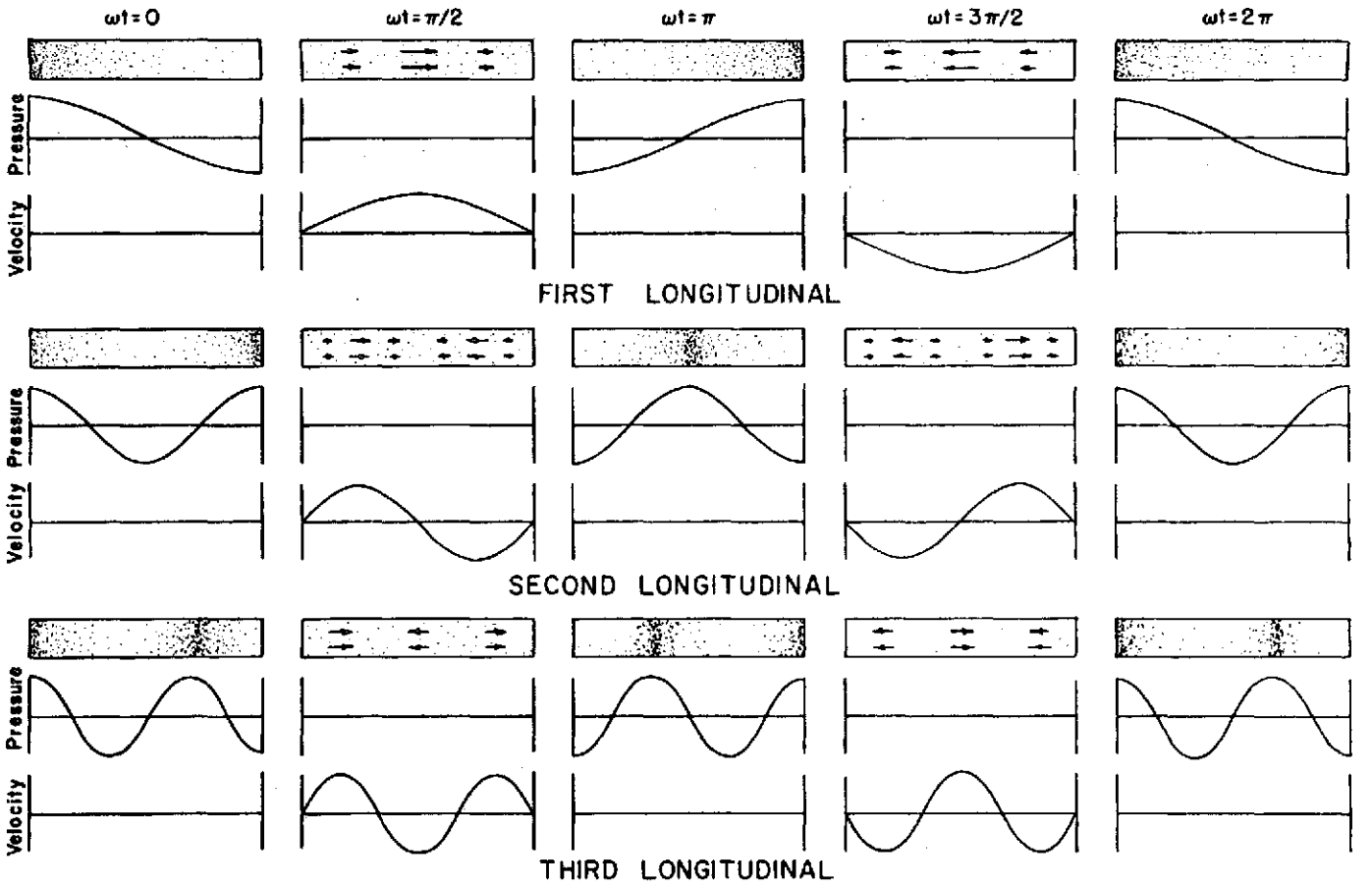

Figure 1. Pressure and Velocity Fluctuations for the First Three Longitudinal Modes of Resonance

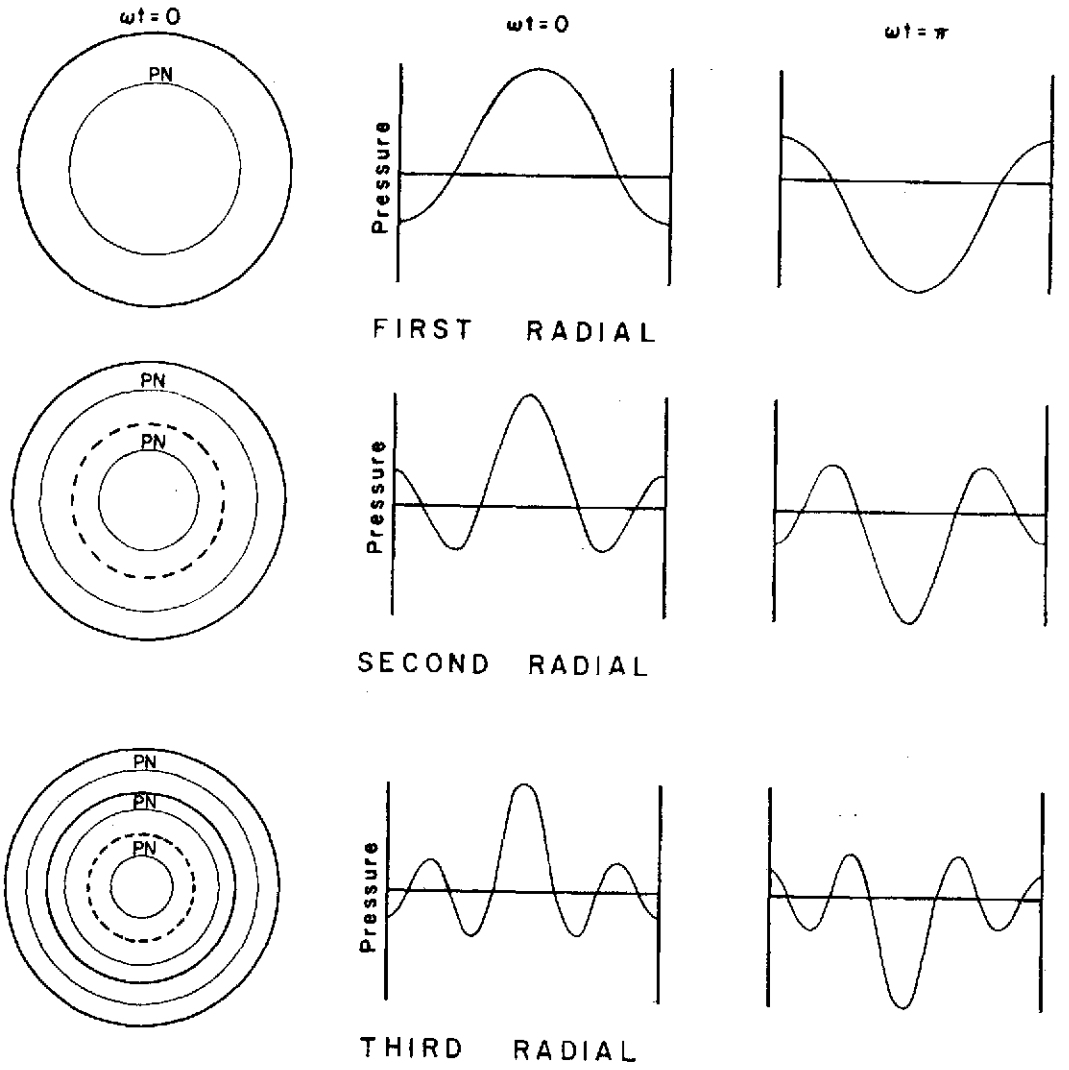

Figure 2. Pressure Distributions for the First Three Radial Modes of Resonance (PN = Pressure Node)

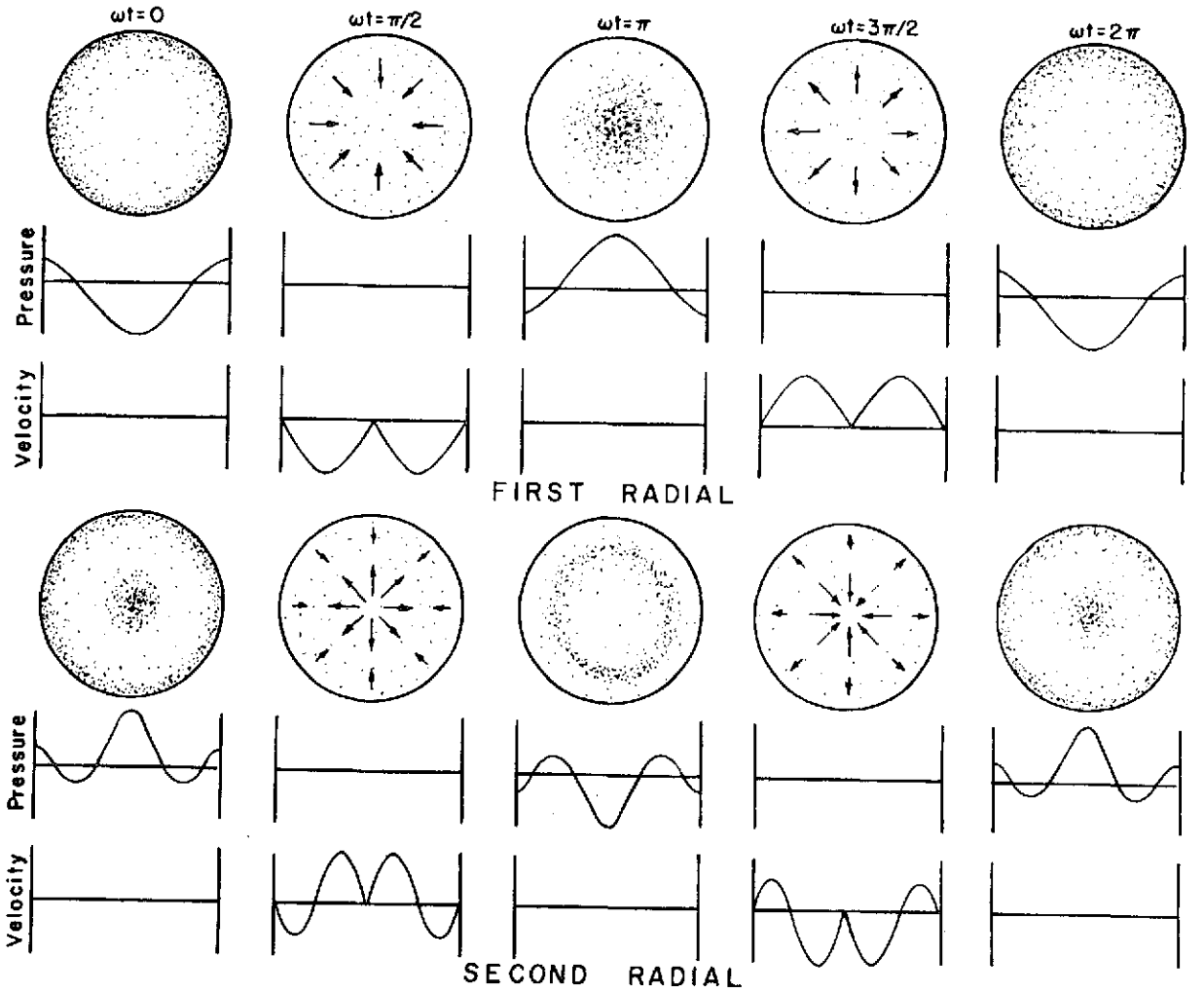

Figure 3. Pressure and Velocity Fluctuations for the First Two Radial Modes of Resonance

and drawings which pictorially show how the pressure and velocity vary. The maximum velocities occur at pressure nodes. The overall velocity effect is movement of the gas molecules in and out along radial lines. The pressure and velocity are a quarter cycle out of phase with each other in time.

The third mode of vibration is the tangential one which has both radial and tangential variations in velocity and pressure. For this mode n and n_z are zero. It can occur in two forms -- standing and spinning. The standing tangential is illustrated in figure 4. The pressure distribution is a Bessel function -- the first standing tangential having a first order Bessel function variation, the second having a second order Bessel function variation, etc. The pressure in the first varies from high on one side of the chamber to low on the other side, then reverses itself. This causes the gas in the chamber to "slosh" back and forth across the chamber. When the pressure distribution has reached a maximum, the velocity distribution is zero, and vice versa. The pressure and velocity are ninety degrees out of phase with each other.

In the second standing tangential the "sloshing" is between quadrants rather than from one side to the other. As the mode number increases, the number of pressure nodal lines increases; hence, the number of segments into which the chamber is divided becomes greater.

The spinning tangential mode has the same resonant frequencies, the same Bessel function distributions in pressure, and the same velocity distributions as the standing one; but their orientation changes (spins) around the chamber at the resonant frequency. The equations have a slightly different form, namely

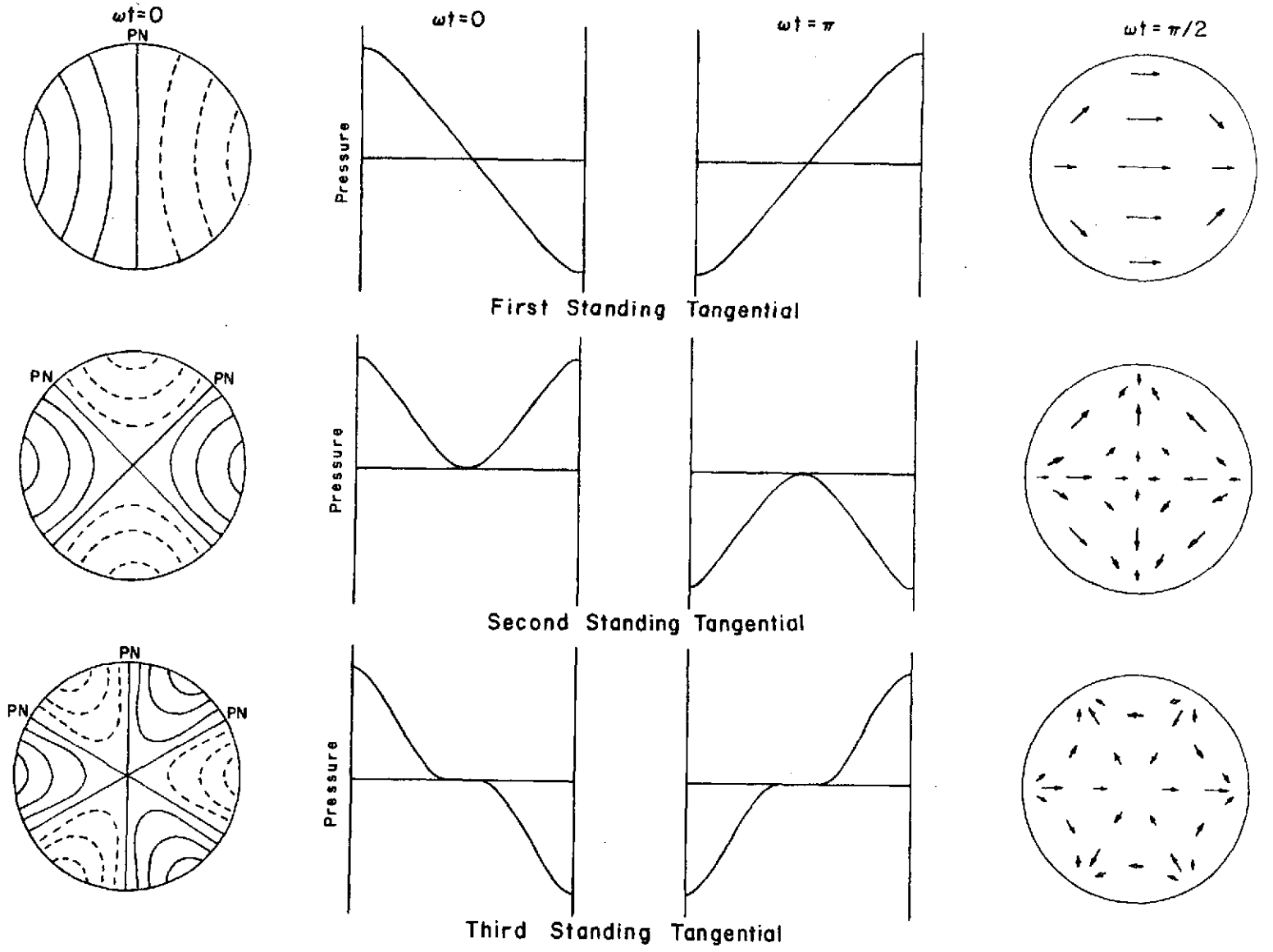

Figure 4. Pressure Distributions and Schematic Velocity Distributions for the First Three Standing Modes of Vibration (PN = Pressure Node)

$$p'_{mnn_z} = \hat{p}_{mnn_z} \frac{J_m(\alpha_{mn}\pi r/R)}{J_m(\alpha_{mn}\pi)} \cos(n_z\pi z/L)\sin(m\theta-\omega_{mnn_z}t-\eta_{mnn_z}) \tag{A.48a}$$

$$v'_{r_{mnn_z}} = \frac{\hat{p}_{mnn_z}\alpha_{mn}\pi}{\rho_\infty\omega_{mnn_z}R} \frac{J_m(\alpha_{mn}\pi r/R)}{J_m(\alpha_{mn}\pi)} \cos(n_z\pi z/L)\cos(m\theta-\omega_{mnn_z}t-\eta_{mnn_z}) \tag{A.48b}$$

$$v'_{\theta_{mnn_z}} = -\frac{\hat{p}_{mnn_z}m}{\rho_\infty\omega_{mnn_z}r} \frac{J_m(\alpha_{mn}\pi r/R)}{J_m(\alpha_{mn}\pi)} \cos(n_z\pi z/L)\sin(m\theta-\omega_{mnn_z}t-\eta_{mnn_z}) \tag{A.48c}$$

$$v'_{z_{mnn_z}} = -\frac{\hat{p}_{mnn_z}n_z\pi}{\rho_\infty\omega} \frac{J_m(\alpha_{mn}\pi r/R)}{J_m(\alpha_{mn}\pi)} \sin(n_z\pi z/L)\cos(m\theta-\omega_{mnn_z}t-\eta_{mnn_z}) \tag{A.48d}$$

$$\rho'_{mnn_z} = \frac{\hat{p}_{mnn_z}}{c_\infty^2} \frac{J_m(\alpha_{mn}\pi r/R)}{J_m(\alpha_{mn}\pi)} \cos(n_z\pi z/L)\sin(m\theta-\omega_{mnn_z}t-\eta_{mnn_z}) \tag{A.48e}$$

There is an interchangability in the effect of time and angular position. The standing and spinning tangential modes are compared in figure 5. There are no longer any pressure nodal lines -- there is a nodal point in the center. At any location in the chamber the maximum pressure and maximum tangential velocity occur at the same time -- they are in phase. But the pressure and radial velocity are out of phase by ninety degrees.

What particular mode or modes of vibration will develop in a chamber, and how intense they will be, depends on the nature of the driving mechanism. The driving mechanism needs to be located in the vicinity of a pressure antinode for the particular mode being driven. Referring to figure 1, the driver should be placed near either end to create the first longitudinal mode. To create the second longitudinal

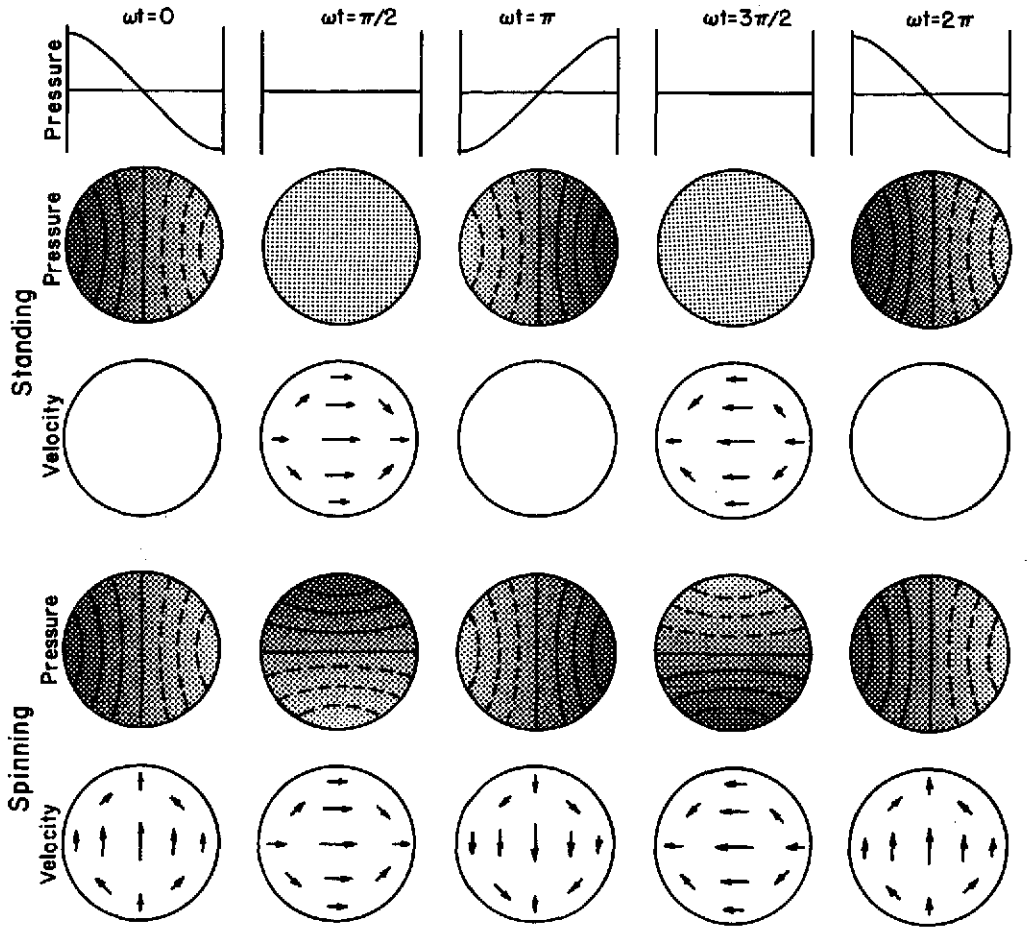

Figure 5. Comparison of Standing and Spinning First Tangential Modes of Vibration

mode, the driver could be placed near either end or the middle. To confirm that the location of the driving mechanism affects which mode will develop in a rocket, experiments have been performed in which various modes of instability were generated by changing the location of propellant injection [10]. Also, examinations of rockets which have developed an unstable pattern of combustion during actual operation indicate that strong spinning transverse modes of acoustic oscillations are dominant.

An effective location for pressure and velocity probes can also be determined by the pressure and velocity distributions. For example, a pressure probe at the center of the chamber would not detect any variations due to the first longitudinal mode since that is the location of a pressure node; however, a velocity probe at the center would detect maximum velocity variations for the first longitudinal mode.

Response Factor

As was mentioned earlier, Lord Rayeigh suggested that the interaction between an oscillatory heat source (e.g., a combustion process) and acoustic oscillations could amplify the oscillations [7]. To measure this coupling between the combustion process in a rocket engine and the pressure variations associated with the acoustic vibrations, nonlinear, in-phase response factor has been developed [11] and is defined as

$$R_{n\ell} = \frac{\int_0^{2\pi} \tilde{w}' \, \tilde{P}' \, d(\omega t)}{\int_0^{2\pi} (\tilde{P}')^2 \, d(\omega t)} \qquad (1.1)$$

where $\tilde{\omega}'$ = perturbation in the normalized burning rate

$\tilde{P}'$ = perturbation in the pressure

The notation being used here is of particular significance. As was done earlier, the conventions of acoustics are being used in that the value of a property is expressed as the sum of a time-mean value and a perturbation about the mean, i.e.,

$$\beta = \overline{\beta} + \beta' \tag{1.2}$$

where the bar over the property indicates the time-mean component and the prime designates the time-dependent component. Further, the time-dependent component can be expressed in terms of a non-dimensional component $\tilde{\beta}'$,

$$\tilde{\beta}' = \frac{\beta'}{\overline{\beta}} \tag{1.3}$$

Using this notation, $\tilde{\beta}'$ represents a percentage, or fractional, deviation about the mean value. Substituting equation (1.3) into equation (1.2) and regrouping, β becomes

$$\beta = \overline{\beta}\,(1 + \tilde{\beta}') \tag{1.4}$$

It is the perturbation about the mean value $\tilde{\beta}'$ which is of interest, not the mean value itself. It has been shown that unstable combustion for sinusoidal oscillations will occur when the in-phase response factor is greater than some value between 0.8 and 1.0; that is, the oscillations will grow with time [3]. A nonlinear out-of-phase response factor, $I_{n\ell}$ has also been developed, but its role is not entirely clear at this time.

Studies have shown that although vibrations in a combustion chamber may start out as sinusoidal, they change with time and develop into a distorted wave form [12]. Realizing this, Heidmann of NASA's Lewis Research Center analytically calculated response factors for distorted sinusoidal wave forms [3]. He used as a model of the combustion process

$$w = c_1(R_e)^m = c_1\left[\frac{\rho DU}{\mu}\right]^m \tag{1.5}$$

where w = burning rate (energy release per unit time and volume)

c_1 = constant of proportionality

Re = propellant drop Reynolds number

ρ = gas density

D = diameter of the propellant drops

U = magnitude of the relative velocity of the drops compared to the gas

μ = gas viscosity

m = Reynolds number exponent which characterizes the particular type of burning

This Reynolds number dependency is characteristic of many combustion mechanisms and in particular is appropriate for the drop vaporization process in a liquid propellant rocket [13]. Assuming that burning takes place immediately upon vaporization of the propellants, and that $m = 0.5$ is typical of the drop vaporization process, the burning rate for vaporization limited combustion, using equation (1.5), is

$$w = c_1\left[\frac{\rho DU}{\mu}\right]^{0.5} \tag{1.6}$$

It is this expression for the burning rate which Heidmann used in his analysis. From it he created a normalized burning rate W such that

$$W = \frac{w}{w_o} \tag{1.7}$$

where w = burning rate with oscillations

w_o = burning rate without oscillations

To expand W, an expression is needed for the relative velocity of the drops in terms of steady and oscillatory components. It was assumed that the droplets have only a steady axial component of velocity. Then the magnitude of the relative velocity of a drop compared to the local gas velocity is given by

$$U^2 = |\bar{u}_\ell - \bar{v}_z|^2 + v_\theta'^2 + v_r'^2 \tag{1.8}$$

where $\bar{u}_\ell$ = axial velocity of a drop

$\bar{v}_z$ = axial velocity of the gas

v_θ' = tangential velocity of the gas

v_r' = radial velocity of the gas

The axial velocity difference is defined as $\overline{\Delta V}$

$$\overline{\Delta V} = |\bar{u}_\ell - \bar{v}_z| \tag{1.9}$$

and is assumed constant. The velocity components v_θ' and v_r' represent the acoustic perturbations of the gas; the perturbations occur only in the transverse directions. They are combined into one term v_t' defined by

$$v_t'^2 \equiv v_\theta'^2 + v_r'^2 \tag{1.10}$$

From equations (1.8), (1.9) and (1.10),

$$U = \overline{\Delta V}\left[1 + \left(\frac{v_t'}{\overline{\Delta V}}\right)^2\right]^{0.5} \tag{1.11}$$

Writing ρ in terms of its time-mean and time-dependent components, using equation (1.11) to express the velocity, and equation (1.5) for the burning rate, one obtains

$$W = \frac{w}{w_o} = \frac{c_1 \bar{\rho}^m (1+\tilde{\rho}')^m \left(\frac{D}{\mu}\right)^m \overline{\Delta V}^m \left[1 + \left(\frac{v_t'}{\overline{\Delta V}}\right)^2\right]^{m/2}}{c_1 \left(\frac{\rho D \overline{\Delta V}}{\mu}\right)^m}$$

Simplifying, this becomes

$$W = (1 + \tilde{\rho}')^m \left[1 + \left(\frac{v_t'}{\overline{\Delta V}}\right)^2\right]^{m/2} \tag{1.12}$$

The perturbations in density and velocity can be expressed as Fourier series as follows:

$$\tilde{\rho}' = \sum_{n=1}^{\infty} \rho_n \cos(n\omega t - \phi_n) \tag{1.13}$$

$$v_t' = \sum_{n=1}^{\infty} c_\infty v_n \cos(n\omega t - \phi_n - \theta_n) \tag{1.14}$$

where the ϕ_n's specify the phase relationships between the harmonic components, and the θ_n's specify the phase relationships between the density and velocity. As was discussed in Appendix A, for a spinning situation $\theta_n = 0$.

Heidmann devised these expressions to reflect the observation that the oscillations which occur during unstable combustion seem to be predominantly composed of a spinning tangential oscillation at a fundamental frequency distorted by a spinning tangential oscillation at the second harmonic frequency, plus other lesser contributions at higher harmonics. The expressions are modifications of those obtained from the solution of the wave equation, equations (A.48). (The dependence on position does not appear in the equations since the calculations are carried out for a representative location. Also, the density has been normalized.) The major difference between Heidmann's equations and equations (A.48) lies in the characterization of the frequencies. Heidmann characterized them as being whole multiples of the fundamental frequency since this was what was observed in actual rockets; however, the spinning tangential resonant frequencies obtained from the wave equation are not whole multiples of the fundamental due to their dependence on a Bessel function. This point will be discussed in more detail later.

Substituting $\tilde{\rho}'$ and v_t' into equation (1.12), expanding and rearranging terms, an expression for the normalized burning rate can be obtained in the form

$$w = \overline{w}\ (1 + \tilde{w}') \tag{1.15}$$

$\tilde{w}'$ can be written as the harmonic series,

$$\tilde{w}' = \sum_{n=1}^{\infty} \sum_{r=1}^{\infty} A_{n,r} \cos(n\omega t + \alpha_{n,r}) \tag{1.16}$$

where the $A_{n,r}$'s are the harmonic coefficients for burning rate perturbations

and the $\alpha_{n,r}$'s are the harmonic phase angles for burning rate perturbations.

The pressure perturbations can also be expressed as a series,

$$\tilde{P}' = \sum_{n=1}^{\infty} p_n \cos(n\omega t - \phi_n) \qquad (1.17)$$

$\tilde{W}'$ and $\tilde{P}'$ can then be substituted into equation (1.1) for $R_{n\ell}$ and integrated to obtain the response. Instead of carrying out these rather involved calculations, numerical methods can also be used to obtain the response. (Heidmann used both techniques and found good agreement between them.)

The last part of this analysis is only outlined here since the actual expressions involved are very long and complex, and it is not the purpose here to give a detailed explanation of Heidmann's work but rather to give an outline of his procedures and results so that they can be compared to the procedures used for this research.

Heidmann calculated $R_{n\ell}$ for various combinations of harmonic content, phase angles, relative drop velocity, and other variables. He found that the system is predicted to be relatively insensitive to sinusoidal perturbations; however, adding varying amounts of distortion could increase $R_{n\ell}$ by an order of magnitude. Unstable combustion was definitely predicted for some conditions. The relative axial drop velocity was also shown to affect the stability.

Experimental confirmation of these results was desired but could not be obtained due to the problems associated with making measurements in a burning rocket, the very short period between the onset of instability and the destruction of the rocket and the concomitant existence of many other uncontrolled variables.

PURPOSE AND SCOPE

The purpose of this work is to select a Reynolds number dependent process which is amenable to experimental investigation, to perform a Heidmann-type analysis of it to determine if it is qualitatively the same and to perform an experimental study for the same conditions examined theoretically -- insofar as is possible within experimental limitations. The results of the above studies will then be compared and used to determine if the addition of distortion to sinusoidal acoustic perturbations of the process involved will increase the response and possibly drive it to instability. These open-loop results will then be used to explain the mechanisms necessary for sustained closed-loop operation.

Chapter 2

ANALYTICAL INVESTIGATIONS

INTRODUCTION

To extend the significance of Heidmann's analysis and to have a basis of comparison for the experimental work, another Reynolds number dependent process was selected and analyzed in the same manner as that by Heidmann. To facilitate comparison, the same type acoustic oscillations were imposed -- pure sinusoidal and distorted sinusoidal spinning transverse acoustic oscillations. Heidmann was particularly interested in the distorted sinusoidal oscillations since they are the most frequently encountered mode of unstable combustion [3]. The choice of the analogous process was primarily influenced by its amenability to experimental investigation. In both Heidmann's analysis and this analysis, it was desired to see if the addition of distortion to sinusoidal acoustic perturbations of the Reynolds number dependent process involved would increase the response and drive the process to instability. Variations in the through-flow velocity and the amplitude and phase angle of the distortion component were considered. The analytical investigations presented are based on reference [14].

THE ANALOG

A qualitative description of the drop vaporization process will provide a basis for choosing a suitable analog. In the combustion

process a liquid droplet exists at a temperature close to its saturation temperature corresponding to the partial pressure of its vapor. The gas mixture, which surrounds the droplet, moves relative to it and has a temperature which is often significantly higher than the droplet's. Much of the energy transfer from the gas mixture to the droplet is by forced convection and, under steady-state conditions, results in vaporization of the droplet liquid.

Assuming the drop vaporization process to be convection dominated, a reasonable analog of this process is that of forced convection heat transfer from a hot wire to a cool gas. Since the constant-temperature hot-wire anemometer provides an excellent means for experimentally determining the instantaneous energy transfer rate from a hot wire, it is used as the analog process.

To provide a controlled unsteady environment for the hot wire, a reasonant sound field with forced mean gas motion is used. Before giving a detailed description of the wire's environment, the physics of a constant-temperature hot wire in an unsteady gas flow will be developed.

The physical system is shown in figure 6. It is assumed that there exists a steady mean flow $\overline{w}$, that unsteady perturbations in the flow may exist in any direction, and that the wire is oriented such that its axis is normal to the mean-flow direction. For the cartesian coordinate system shown in figure 6, the z-axis is in the mean-flow direction and the y-axis is parallel to the cylinder.

Energy is electrically supplied to the wire such that its temperature is constant; the constant-temperature anemometer provides the needed energy and controls. A natural limitation for constant

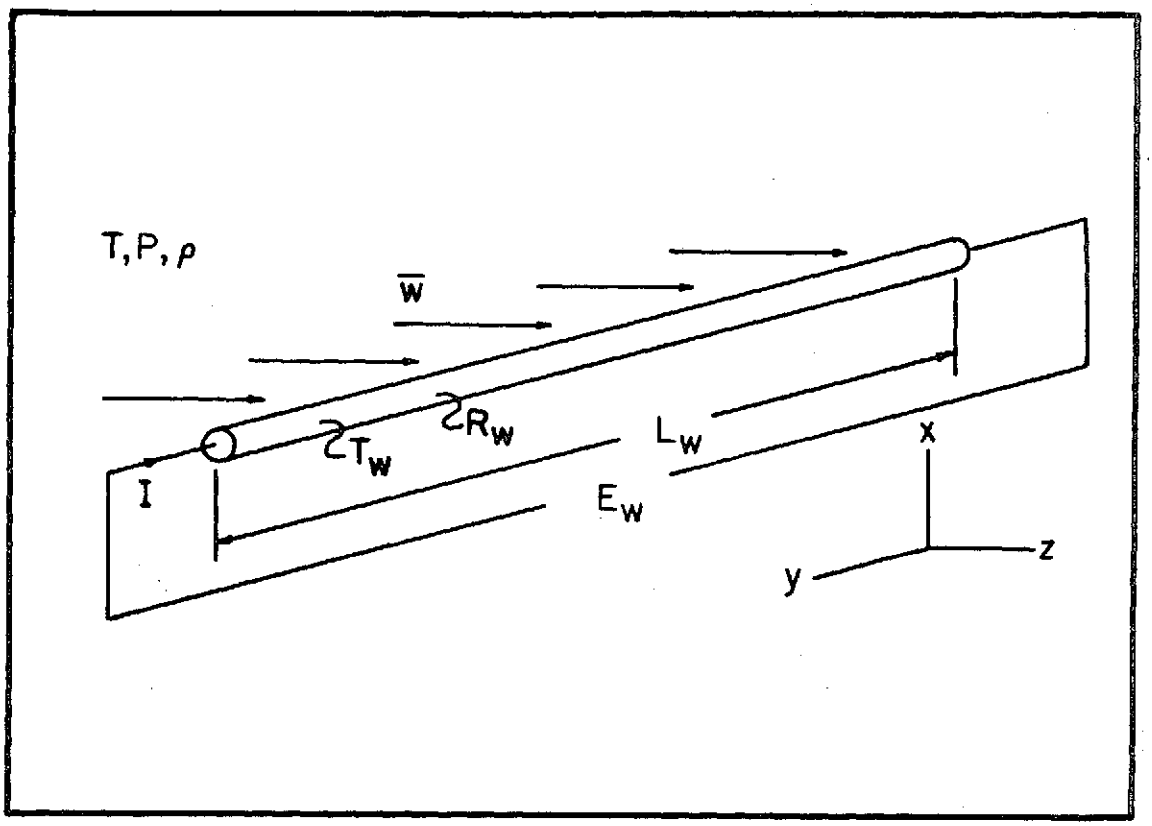

Figure 6. Schematic Diagram of the Hot Wire and Its Environment

temperature operation is that the gas temperature must not exceed the normal operating temperature of the wire.

Taking the hot wire to be a closed system, the first law of thermodynamics is

$$\frac{dQ}{dt} = \frac{d\hat{E}}{dt} + \frac{dW}{dt} \tag{2.1}$$

For constant temperature operation the total energy of the wire is constant and equation (2.1) becomes

$$\frac{dQ}{dt} = \frac{dW}{dt} \tag{2.2}$$

The rate of electrical work done by the system is

$$\frac{dW}{dt} = -I^2R_w \tag{2.3}$$

Three modes of energy transfer as heat exist; however, radiation is small enough to be neglected, conduction and convection are lumped together, and Newton's law of cooling is used to express the heat transfer rate. Thus

$$\frac{dQ}{dt} = - hA_w[T_w - T] \tag{2.4}$$

Introducing the Nusselt number,

$$Nu_f = \frac{hD_w}{k_f} \tag{2.5}$$

equations (2.2), (2.3) and (2.4) reduce to

$$I^2R_w = \pi k_f L_w Nu_f[T_w - T] \tag{2.6}$$

Certain auxiliary relations are now introduced to permit equation (2.6) to be expressed in terms of the properties normally measured and/or known.

The electrical resistance of the wire is a linear function of temperature in the range being considered; therefore, its operating resistance R_w can be expressed as a function of its "cold" resistance R_∞ and the temperature difference between the atmosphere and the wire when it is in operation

$$R_w = R_\infty + [T_w - T] \tag{2.7}$$

Since in the Disa anemometer system the potential drop across the wire is not directly measured, it is necessary to express the current in equation (2.6) in terms of the Disa bridge properties. For the bridge network shown in figure 7, the hot-wire current is

$$I = \frac{E}{R_s + R_{cbl} + R_p + R_w} \tag{2.8}$$

There are a number of possible correlations that could be used to express the Nusselt number Nu_f in terms of the flow field variables. King [15], in 1914, was the first to develop such a correlation. Recently Andrews, Bradley and Hundy [16] brought together the many different correlations which have been proposed by various investigators since then and compared them to each other and to some extensive work of their own. They found that the most reliable correlation for low Reynolds number flows ($0.02 < Re_f < 44$) is that of Collis and Williams [17], namely

$$Nu_f = [A + B\, Re_f^{\,N}][T_f/T_\infty]^{0.17} \tag{2.9}$$

where A, B and N are determined by actual calibration of the hot wire

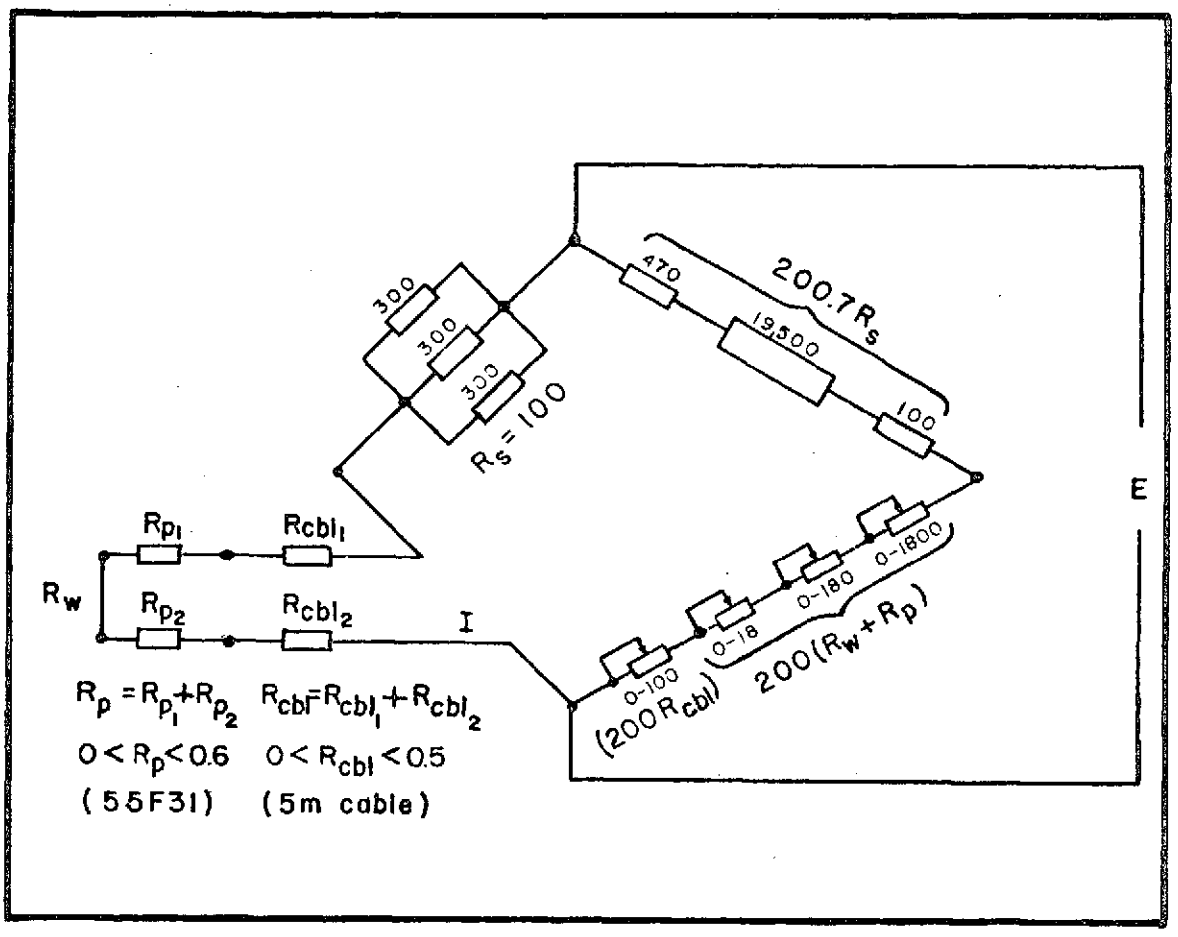

Figure 7. Disa Hot-Wire Bridge Network

used and T_f is the film temperature defined as $T_f = (T_w + T_\infty)/2$. (The calibration procedure is described in Chapter 3.)

Since the experiments used atmospheric air at room temperature and pressure, the viscosity and thermal conductivity data are taken from Hilsenrath [18] and the density is computed from the ideal gas relation, namely

$$\rho = \frac{P}{R_a T} \tag{2.10}$$

The Hilsenrath data in the temperature range of interest ($273.15°K < T < 473.15°K$), can be accurately approximated by

$$k = k_o[T/T_o]^{0.877} \tag{2.11}$$

and

$$\mu = \mu_o[T/T_o]^{0.757} \tag{2.12}$$

The relationship between the hot-wire bridge voltage and the flow properties is obtained by combining equations (2.6), (2.8), (2.9), (2.10), (2.11) and (2.12). This gives

$$E^2 = \left[\frac{[R_s + R_{cbl} + R_p + R_w]^2}{R_w}\right][\pi L_w k_o]\left[A + B\ Re_{f_1}{}^N\ (\tilde{V}^2)^{N/2}\right]$$

$$\left[\frac{T_f}{T_\infty}\right]^{0.17}\left[\frac{T_f}{T_o}\right]^{0.877}[T_w - T] \tag{2.13}$$

where

$$Re_{f_1} = \frac{P\ V_1\ D_w}{R_a T_f \mu_o [T_f/T_o]^{0.757}} \tag{2.14}$$

and

$$\tilde{V}^2 = [(u')^2 + (Kv')^2 + (\bar{w} + w')^2]/V_1^2 \qquad (2.15)$$

K represents the sensitivity of the hot wire to flow parallel to its axis and is approximately equal to zero. (The wire is primarily sensitive to the components of the flow normal to its axis; it is a two-dimensional sensor. Also, the wire cannot distinguish direction. A velocity of $\vec{V} = V\vec{i}$ generates the same response as a velocity of $\vec{V} = V\vec{k}$. This means the wire cannot distinguish between positive and negative flows either. A velocity of $\vec{V} = V_o \sin \omega t \, \vec{i}$ will appear to the wire as the rectified speed, $V = |V_o \sin \omega t|$.)

Since the empirical relationship for Nu_f, equation (2.9), was obtained for steady-state, steady-flow conditions, its applicability to unsteady flow may be questionable; however, it is customary to assume that it holds for unsteady flows if instantaneous values are substituted for the fluid properties [19]. This is done here and it constitutes a major assumption.

Noting that the leading coefficient in equation (2.13) is constant during normal operation and that it depends on the wire temperature, it can be rewritten in a simpler form by defining dimensional forms of A and B, namely

$$\hat{A} = \hat{C}(T_w)A \qquad (2.16a)$$

$$\hat{B} = \hat{C}(T_w)B \qquad (2.16b)$$

where

$$\hat{C}(T_w) = \pi L_w k_o \left[\frac{[R_w + R_{cbl} + R_p + R_w]^2}{R_w}\right]$$

With this nomenclature the final form of equation (2.13) is

$$E = \left\{\left[\hat{A} + \hat{B}\, Re_{f_1}{}^N (\tilde{V}^2)^{N/2}\right]\left[\frac{T_f}{T_\infty}\right]^{0.17}\left[\frac{T_f}{T_o}\right]^{0.877}[T_w - T]\right\}^{0.5} \qquad (2.17)$$

E is a function of the pressure, velocity and temperature; to determine E the wire must be calibrated and the flow field properties must be known.

During the steady-state, steady-flow calibration of the wire all quantities in equation (2.17) are constant except the velocity; hence, equation (2.17) reduces to

$$E = \left[A + B\, \tilde{V}^N\right]^{0.5} \qquad (2.18)$$

where

$$A = \hat{A}\left[\frac{T_f}{T_\infty}\right]^{0.17}\left[\frac{T_f}{T_o}\right]^{0.877}[T_w - T] \qquad (2.19a)$$

and

$$B = \hat{B}\, R_{e_{f_1}}{}^N\left[\frac{T_f}{T_\infty}\right]^{0.17}\left[\frac{T_f}{T_o}\right]^{0.877}[T_w - T] \qquad (2.19b)$$

The calibration determines the constants, A, B and N, from which $\hat{A}$ and $\hat{B}$ and then A and B can be determined.

FLOW FIELD PROPERTIES

The wire's environment and orientation are schematically shown in figure 8. (The wire is no longer oriented parallel to the y-axis

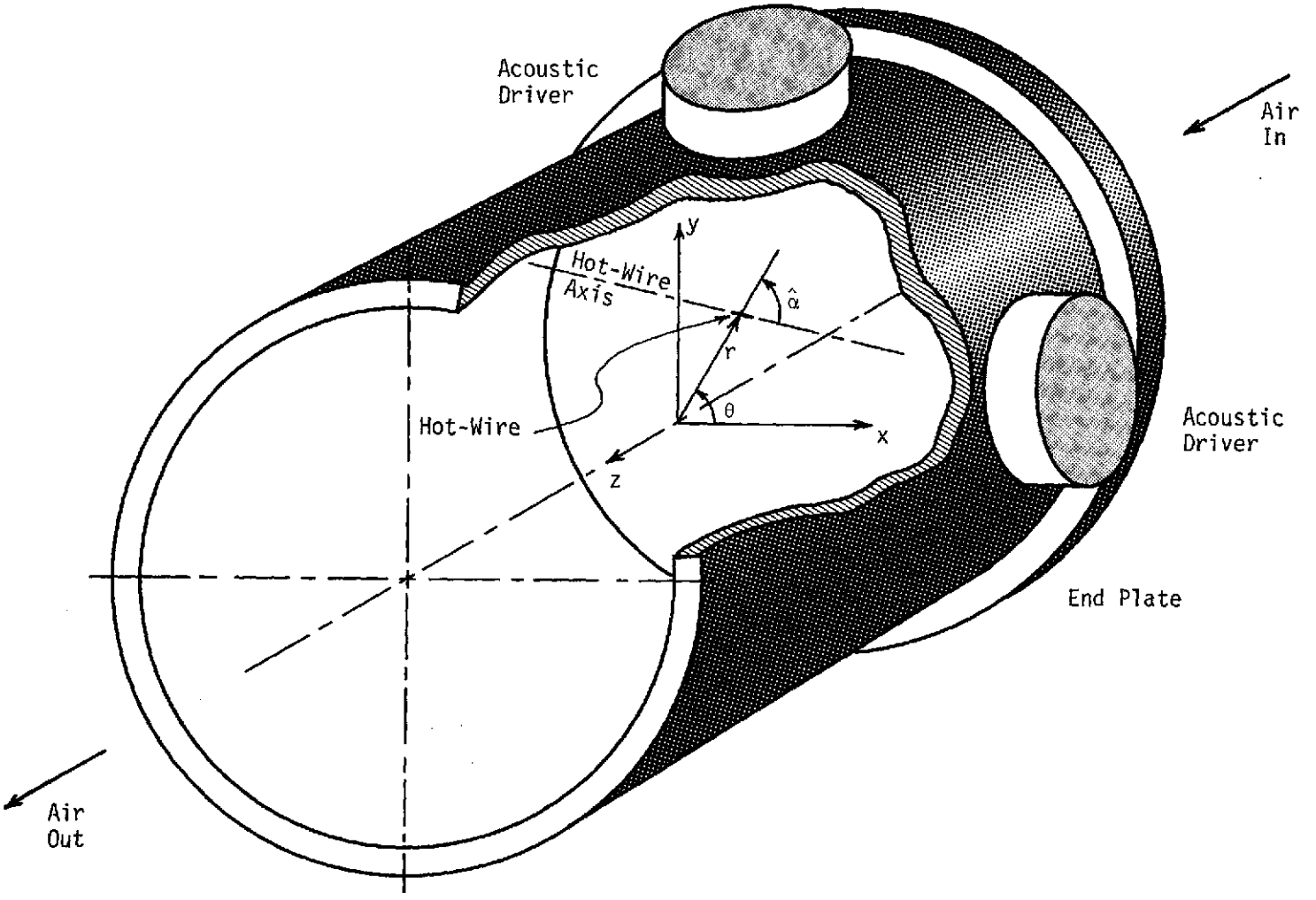

Figure 8. Schematic Diagram of the Hot-Wire in its Cylindrical Enclosure (One End Plate Is Not Shown)

as it was in figure 6.) The wire is surrounded by a cylindrical enclosure, with inside diameter D and length L, which is acoustically closed but permits a uniform forced flow in the axial direction. (This can be accomplished experimentally by the use of perforated end-plates.) The wire is located in a transverse plane.

With proper excitation of the enclosure, acoustic velocity oscillations in any of the three vector directions can be obtained; but, as was described in Chapter 1, Heidmann [3] restricted his analysis to transverse-velocity oscillations "because of the greater interest in transverse-mode instability in rocket combustors." Considering only transverse oscillations to exist, the velocity at any point in the chamber can be expressed as the sum of a constant axial velocity $\bar{v}_z$ and an oscillating transverse velocity v'_t, i.e.,

$$V^2 = \bar{v}_z^2 + v_t'^2 \tag{2.20}$$

where

$$v_t'^2 = v_r'^2 + v_\theta'^2 \tag{1.9}$$

The wire is oriented such that it makes an angle $\hat{\alpha}$ with the radius vector (figure 8). As has been stated previously, the wire is not sensitive to flow parallel to its axis, therefore the wire cooling velocity V_c, expressed in terms of the enclosure's cylindrical system, is

$$V_c^2 = \bar{v}_z^2 + (v_r' \sin \hat{\alpha} + v_\theta' \cos \hat{\alpha})^2$$

Nondimensionalizing this with V_1^2, gives

$$\tilde{V}_c^2 = [\bar{v}_z^2 + (v_r' \sin \hat{\alpha} + v_\theta' \cos \hat{\alpha})^2]/V_1^2 \tag{2.21}$$

For the coordinate system shown in figure 8, $\tilde{V}_c^2$ is used instead of $\tilde{V}^2$ in equation (2.17), the equation for E.

The equations for the acoustic pressure and particle velocity are those obtained in Appendix A, equations (A.48). The acoustic temperature is related to the acoustic pressure. Since the process is assumed to be isentropic,

$$p^{(1-\gamma)}T^{\gamma} = b \tag{2.22}$$

Expressing P and T in terms of their time-mean and fluctuating components, equation (2.22) becomes

$$(\overline{P} + P')^{(1-\gamma)}(\overline{T} + T')^{\gamma} = b \tag{2.23}$$

Expanding the terms on the left-hand side of equation (2.23) by use of a binomial expansion, using equation (2.22) for b and eliminating higher order terms yields

$$\gamma \frac{T'}{\overline{T}} + (1-\gamma) \frac{P'}{\overline{P}} = 0 \tag{2.24}$$

In terms of $\tilde{P}'$ and $\tilde{T}'$, equation (2.24) is

$$\tilde{T}' = \left(\frac{\gamma-1}{\gamma}\right) \tilde{P}' \tag{2.25}$$

The equations for the oscillations in pressure, velocity and temperature are

$$P'_{mnn_z} = \hat{P}_{mnn_z} \frac{J_m(\alpha_{mn}\pi r/R)}{J_m(\alpha_{mn}\pi)} \cos(n_z\pi z/L)\sin(m\theta-\omega_{mnn_z}t-\eta_{mnn_z}) \tag{A.48a}$$

$$V'_{r_{mnn_z}} = \frac{\hat{P}_{mnn_z}\alpha_{mn}\pi}{\rho_\infty \omega_{mnn_z} R} \frac{J_m'(\alpha_{mn}\pi r/R)}{J_m(\alpha_{mn}\pi)} \cos(n_z\pi z/L)\cos(m\theta-\omega_{mnn_z}t-\eta_{mnn_z}) \qquad (a.48b)$$

$$V'_{\theta_{mnn_z}} = -\frac{\hat{P}_{mnn_z} m}{\rho_\infty \omega_{mnn_z} r} \frac{J_m(\alpha_{mn}\pi r/R)}{J_m(\alpha_{mn}\pi)} \cos(n_z\pi z/L)\sin(m\theta-\omega_{mnn_z}t-\eta_{mnn_z}) \qquad (A.48c)$$

$$T'_{mnn_z} = \frac{\overline{T}}{\overline{P}} \left(\frac{\gamma-1}{\gamma}\right)\hat{P}_{mnn_z} \frac{J_m(\alpha_{mn}\pi r/R)}{J_m(\alpha_{mn}\pi)} \cos(n_z\pi z/L)\sin(m\theta-\omega_{mnn_z}t-\eta_{mnn_z}) \qquad (2.26)$$

where $\overline{T} = T_\infty$ and $\overline{P} = P_\infty$.

NONLINEAR RESPONSE FACTOR

Exposing a constant-temperature hot-wire to a mean flow perturbed by acoustic oscillations results in an unsteady hot-wire voltage E. Expressed in terms of its mean and fluctuating components, E is

$$E = \overline{E} + E' \qquad (2.27)$$

or

$$E = \overline{E}[1 + \tilde{E}'] \qquad (2.28)$$

with

$$\tilde{E}' = E'/\overline{E}. \qquad (2.29)$$

A nonlinear, in-phase response factor can be formed for this process just as was done for the combustion process, i.e.,

$$R_{n\ell} = \frac{\int_0^{2\pi} \tilde{E}'\,\tilde{P}'\,d(\omega t)}{\int_0^{2\pi} (\tilde{P}')^2\,d(\omega t)} \qquad (2.30)$$

It is a measure of the portion of $\tilde{E}'$ which is in phase with the acoustic pressure $\tilde{P}'$.

To evaluate $R_{n\ell}$, $\tilde{E}'(\omega t)$ must be related to the sound field given by equations (A.48a), (A.48b), (A.48C) and (2.26) as follows:

- Certain constants of the anemometer and the environment must be determined. These include R_s, R_{cbl}, R_p, P_∞, T_∞, k_o and μ_o.
- A hot wire is selected and its operating temperature determined. This establishes T_w, T_w, L_w and D_w.
- The hot wire is calibrated under steady-state, steady-flow conditions. From the calibration, equation (2.18) is obtained. From this, the constants $\hat{A}$ and $\hat{B}$ can be calculated.
- The hot wire's environment is specified. This includes $\overline{v}_z$, P' and the wire's location in the chamber.
- All the above values are substituted into equation (2.17), thereby producing $E(\omega t)$. (When the above quantities have been specified, the only variable remaining is ωt.)
- The time-mean value of $E(\omega t)$, $\overline{E}$, is obtained from

$$\overline{E} = \frac{1}{2\pi} \int_0^{2\pi} E(\omega t) d(\omega t) \qquad (2.31)$$

  Actual mathematical integration of $E(\omega t)$ is difficult; therefore, the integration is performed numerically.
- The desired $\tilde{E}'(\omega t)$ is given by

$$\tilde{E}'(\omega t) = [E(\omega t)/\overline{E}] - 1 \qquad (2.32)$$

- With $\tilde{E}'$ given by equation (2.32) and $\tilde{P}'$ given by equation (A.48a) nondimensionalized over P_∞, $R_{n\ell}$ is obtained from (2.30).

As before, the integration of $E(\omega t)$ is done numerically. The nature of the nonlinear response factor is best illustrated by numerical examples.

NUMERICAL EXAMPLES

The numerical examples to be presented are based on the following hot-wire and environmental properties:

- Wire and Bridge Properties

$$L_w = 1.02 \text{ mm}$$
$$D_w = 5 \ \mu\text{m}$$
$$\alpha = 0.0126 \text{ ohm/K}^\circ$$
$$R_p = 0.40 \text{ ohm}$$
$$R_{cbl} = 0.30 \text{ ohm}$$
$$R_s = 100 \text{ ohms}$$
$$R_w - R_\infty = 1.40 \text{ ohms}$$
$$R_\infty = 3.59$$
$$A = 0.521$$
$$B = 0.673$$
$$N = 0.444$$

- Basic Air Properties

$$T_o = 273.15^\circ\text{K}$$
$$k_o = 2.413 \times 10^{-2} \text{ kg-m/(sec}^3\text{-K}^\circ\text{)}$$
$$\mu_o = 1.716 \times 10^{-5} \text{ kg/(sec-m)}$$
$$R_a = 287.1 \text{ m}^2\text{/(sec}^2\text{-K}^\circ\text{)}$$
$$\gamma = 1.4$$

● Wire Environmental Properties

$T_\infty = 298.3°K$

$P_\infty = 735.0$ mm Hg

$L = 31.30$ cm

$D = 20.49$ cm

With these properties specified, the main variables are the hot-wire Mach number $M = \bar{v}_z/c_\infty$, the acoustic oscillations and the location and orientation of the wire.

The equations used to express the acoustic oscillations have to be compatible with those used by Heidmann and those obtained from the solution of the inviscid wave equation. As was mentioned in Chapter 1, Heidmann assumed the frequencies involved where all whole multiples of the fundamental frequency since that was what has been observed in actual rockets. He regarded the acoustic oscillations as the sum of a fundamental (n = 1) plus distortion components (n = 2,3,...). In his calculations he used only one distortion component since, in actual rockets, the contribution from the higher harmonics is very small.

From equation (A.38)

$$f_{mnn_z} = \frac{\omega_{mnn_z}}{2\pi} = \frac{c_\infty}{2}\left[\left(\frac{\alpha_{mn}}{R}\right)^2 + \left(\frac{n_z}{L}\right)^2\right]^{0.5} \qquad (A.38)$$

which expresses the resonant frequencies as derived from the inviscid wave equation, it is clear that the resonant frequencies of pure spinning tangential waves are not whole multiples of the fundamental; however, by proper choice of the L/D ratio of the chamber, a combination

mode can be forced to have twice the frequency of the pure mode. This was done here. A more complete discussion of this is given in Chapter 3.

With L and D as given, the frequency of the second-spinning, second-longitudinal combination mode (hereafter referred to as the (202) mode) is twice the frequency of the first-spinning pure tangential mode (hereafter referred to as the (100) mode). The (202) mode has a time-dependent component of longitudinal velocity v_z'; however, a longitudinal velocity node exists for this mode at the central cross-section of the chamber. Because of this, the spatial behavior of the (202) mode, at the center of the chamber, is the same as that of a second spinning pure tangential mode (hereafter referred to as the (200) mode). Hence, the longitudinal location of the wire is chosen as $z = L/2$.

To have agreement with Heidmann in the form of the velocity equations, the wire is chosen to be oriented such that $\alpha = 0$ (the wire's axis is parallel to the radius vector) and $\theta = 0$. In this way only the tangential component of velocity affects the wire and the form of the velocity equation agrees with that of Heidmann. The radial position of the wire is taken as $r = 0.95R$.

When the above quantities are substituted into the equations for the acoustic pressure and particle velocity, they have the same form as Heidmann's equations for the acoustic pressure and particle velocity. Letting $\tilde{P}_1'$ be the normalized acoustic pressure of the (100) mode and $\tilde{P}_2'$ be the normalized acoustic pressure of the (202) mode, and with $\omega_{202} = 2\omega_{100} = 2\omega$, the fundamental and distortion components of the pressure are

$$\tilde{P}_1' = P_{100}'/P_\infty = p_1 \cos(\omega t - \phi_1) \qquad (2.33a)$$

and

$$\tilde{P}_2' = P_{202}'/P_\infty = p_2 \cos(2\omega t - \phi_2) \tag{2.33b}$$

where

$$p_1 = \frac{\hat{P}_{100}}{P_\infty} \frac{J_1(0.95\ \alpha_{10}\ \pi)}{J_1(\alpha_{10}\ \pi)} \tag{2.34a}$$

$$\phi_1 = -(\eta_{100} + 90°) \tag{2.34b}$$

$$p_2 = -\frac{\hat{P}_{202}}{P_\infty} \frac{J_2(0.95\ \alpha_{20}\ \pi)}{J_2(\alpha_{20}\ \pi)} \tag{2.34c}$$

and

$$\phi_2 = -(\eta_{202} + 90°)$$

Similarly, the acoustic particle velocities are

$$v_{t_1}' = v_{\theta_{100}}' = c_\infty v_1 \cos(\omega t - \phi_1) \tag{2.35a}$$

and

$$v_{t_2}' = v_{\theta_{202}}' = c_\infty v_2 \cos(2\omega t - \phi_2) \tag{2.35b}$$

where

$$c_\infty v_1 = -\frac{\hat{P}_{100}}{0.95\ \rho_\infty\ \omega_{100}\ R} \frac{J_1(0.95\ \alpha_{10}\ \pi)}{J_1(\alpha_{10}\ \pi)} \tag{2.36a}$$

and

$$c_\infty v_2 = \frac{2\ \hat{P}_{202}}{0.95\ \rho_\infty\ \omega_{202}\ R} \frac{J_2(0.95\ \alpha_{20}\ \pi)}{J_2(\alpha_{20}\ \pi)} \tag{2.36b}$$

Combining equations (2.33) and equations (2.35), gives

$$\tilde{p}' = \sum_{n=1}^{2} p_n \cos(n\omega t - \phi_n) \tag{2.37a}$$

and

$$v_t' = \sum_{n=1}^{2} c_\infty v_n \cos(n\omega t - \phi_n) \tag{2.37b}$$

Equation (2.37a) is the same as Heidmann's equation (1.17) with the series terminated at 2, as was done in his analysis. Equation (2.37b) is the same as Heidmann's equation (1.14) with the series again terminated at 2 and with $\theta_n = 0$, which again is what Heidmann used. (The θ_n's were set equal to zero by Heidmann to model a spinning situation.)

In carrying out the actual calculations of $R_{n\ell}$, the wire Mach number ($M \equiv \bar{v}_z/c_\infty$), the intensity of p_1, the ratio of p_2/p_1 and the phase angle between p_2 and p_1 can be varied. What follows is a presentation of the effect of these variables on $R_{n\ell}$.

RESULTS

The following is a graphical presentation and discussion of the results of the calculations of the response factors for various values of M, p_1, p_2 and ϕ_2

Influence of Harmonic Content on $R_{n\ell}$

Considering sound pressure wave distortion due only to the second harmonic of p_1 (i.e., due to p_2), the nonlinear in-phase response factor was computed. The results are displayed graphically in figure 9 for various ratios of p_2 to p_1. For this Mach number (M = 0.005), the

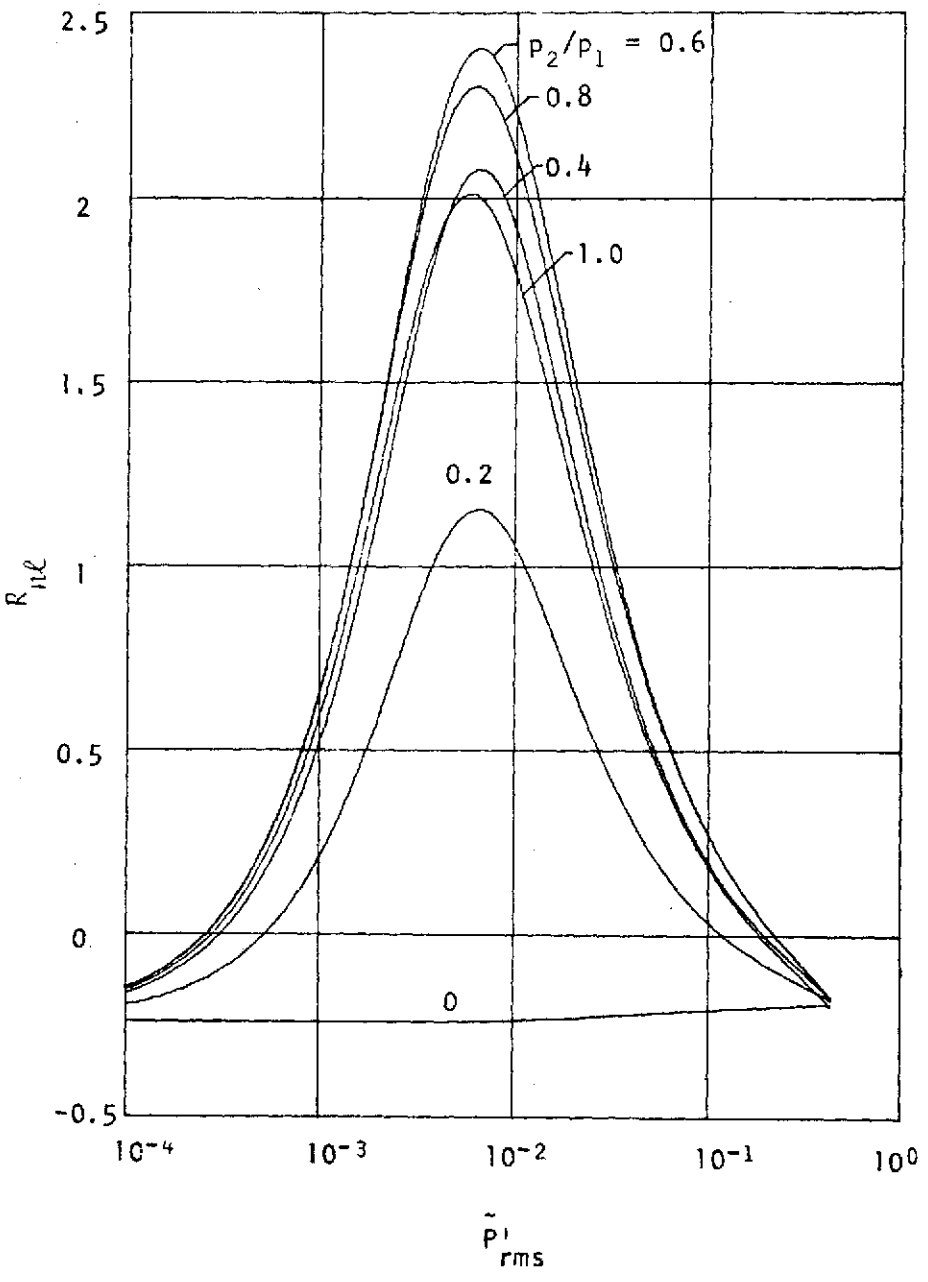

Figure 9. Response Factor Versus Root-Mean-Square Sound Pressure Level for Various Harmonic Contents; M = 0.005, $\phi_1 = \phi_2 = \theta_1 = \theta_2 = 0$, $T_w - T_\infty = 111.0$ K°

maximum response seems to occur for a nondimensionalized root-mean-square sound pressure level of 0.00631 and for p_2/p_1 approximately equal to 0.6. Figure 9 is similar in form to that obtained by Heidmann [3] for the combustion process; however, the peak response occurs at a lower value of $\tilde{P}'_{rms}$ for the hot-wire than for the combustion process. This figure very clearly shows the effect of the distortion component p_2 on the response factor.

Figure 10 was generated for the same conditions as figure 9 with the exception of the wire Mach number; figure 10 is for a zero through-flow velocity. This condition is of interest because it is the easiest to deal with experimentally and, as will be seen in figure 11, produces the maximum response.

Influence of Mach Number on $R_{n\ell}$

For a fixed pressure waveform (p_2/p_1 = 0.6) and for the value of $\tilde{P}'_{rms}$ at which the peak response occurs, values of $R_{n\ell}$ were computed for various wire Mach numbers. The results are shown in figure 11. Figure 12 shows the variation in $R_{n\ell}$ with changes in $\tilde{P}'_{rms}$ for various wire Mach numbers. Generally speaking the lower the Mach number, the greater the response. It should also be noted that the value of the sound level at which peak response occurs increases with increasing Mach number. These results agree with those of Heidmann [3].

Influence of Harmonic Phase Angle on $R_{n\ell}$

The influence of ϕ_2 on the nonlinear response factor for the conditions of the peak $R_{n\ell}$ of figure 9, except for ϕ_2, is shown in figure 13. The response factor has its maximum at ϕ_2 = 0 degrees. Figure 14

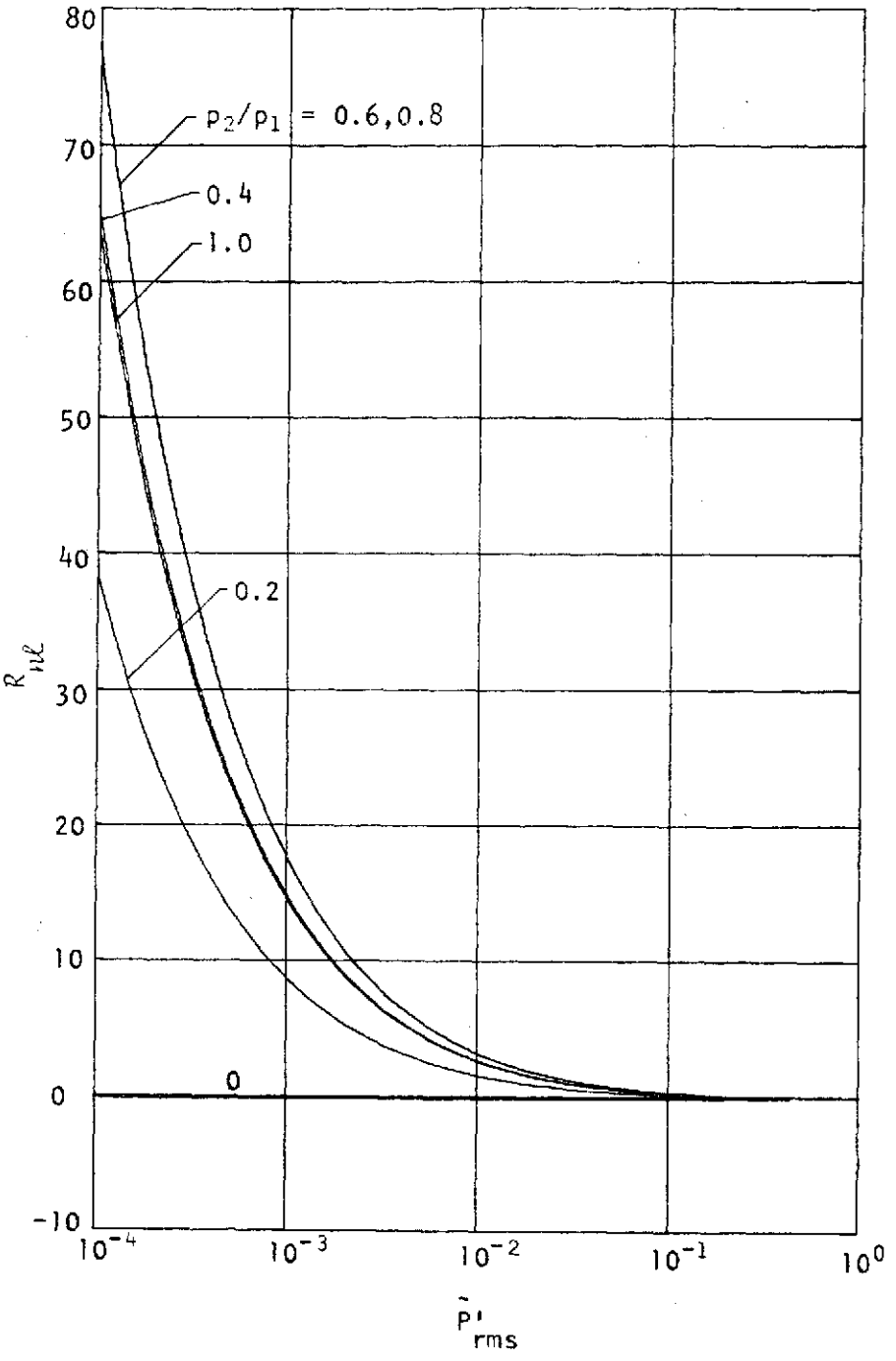

Figure 10. Response Factor Versus Root-Mean-Square Sound Pressure Level for Various Harmonic Contents; $M = 0$, $\phi_1 = \phi_2 = \theta_1 = \theta_2 = 0$, $T_w - T_\infty = 111.0\ K°$

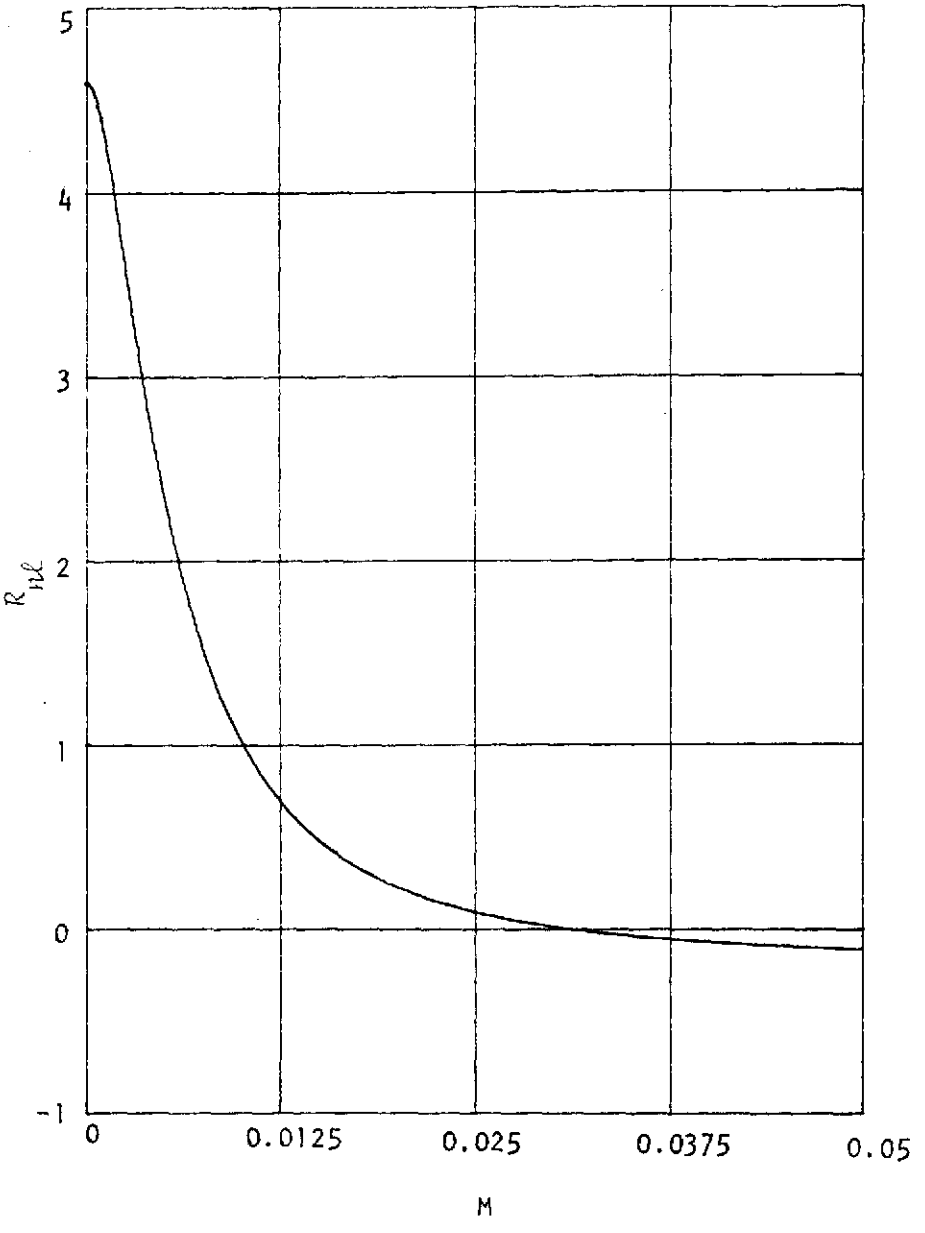

Figure 11. Response Factor Versus Wire Mach Number; $p_2/p_1 = 0.6$, $\tilde{P}'_{rms} = 0.00631$, $\phi_1 = \phi_2 = \theta_1 = \theta_2 = 0$, $T_w = T_\infty = 111.0$ K°

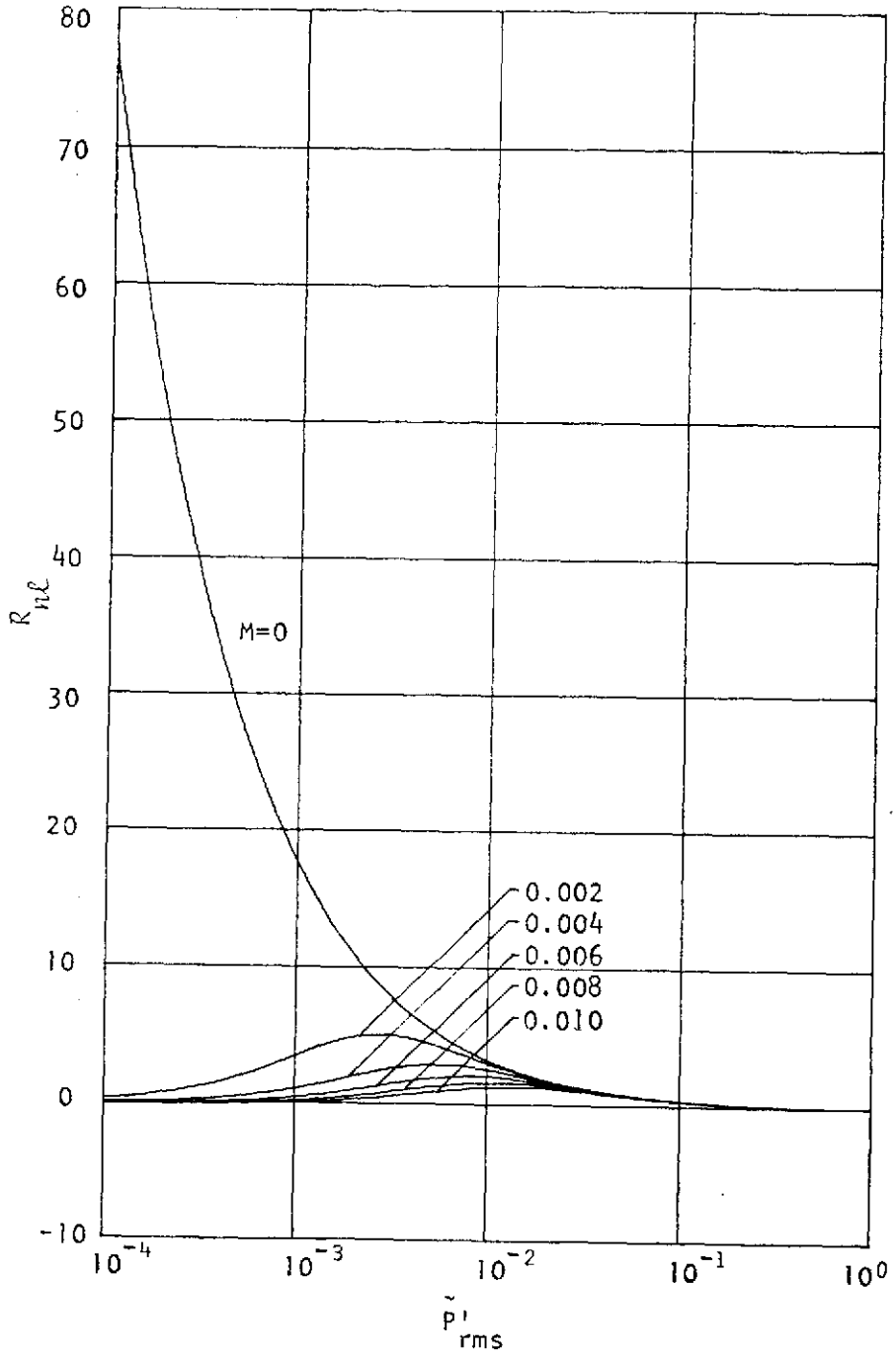

Figure 12. Response Factor Versus Root-Mean-Square Sound Pressure Level for Various Mach Numbers; $\phi_1 = \phi_2 = \theta_1 = \theta_2 = 0$, $T_w - T_\infty = 111.0\ K°$, $p_2/p_1 = 0.6$

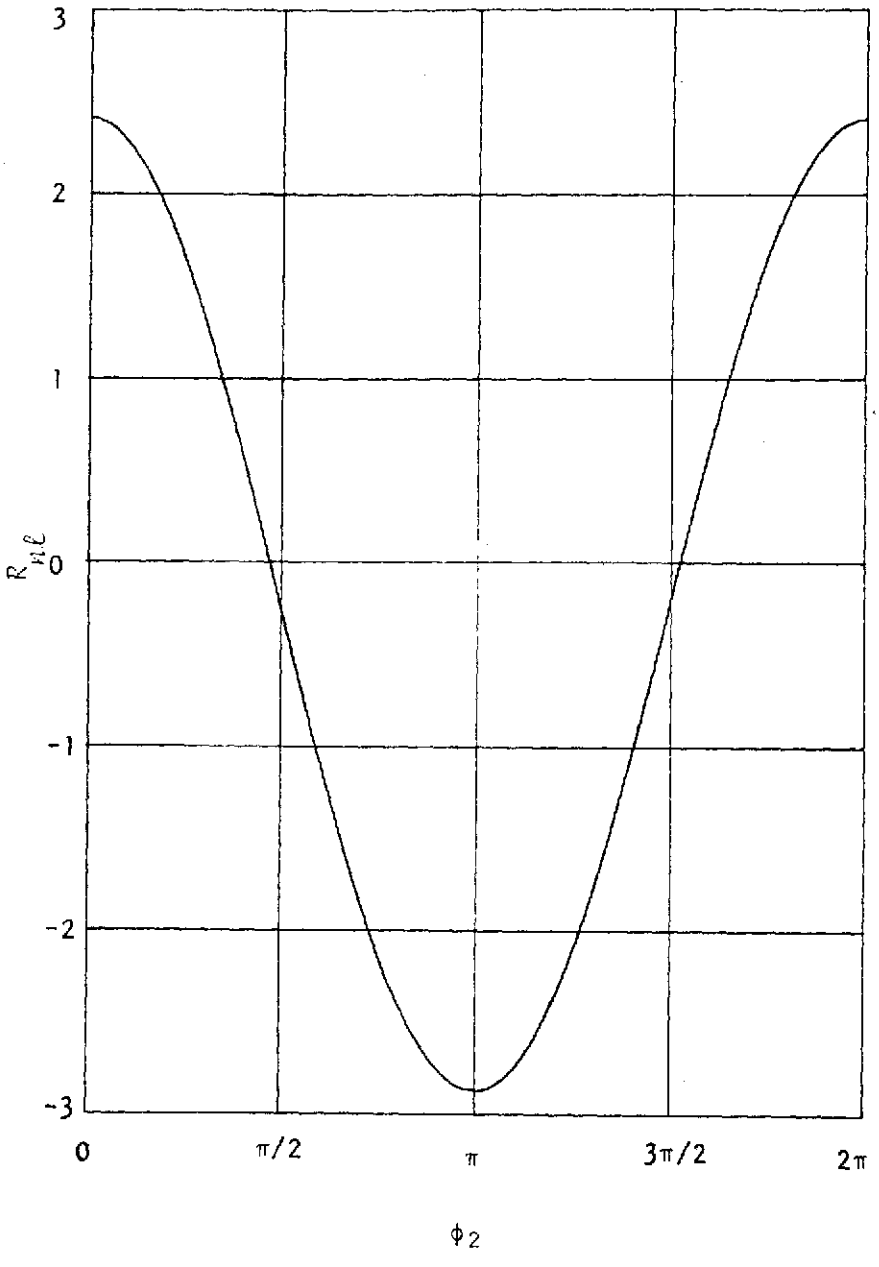

Figure 13. Response Factor Versus Phase Angle Between Fundamental Sound Pressure Component and Its Second Harmonic; $M = 0.005$, $\phi_1 = \theta_1 = \theta_2 = 0$, $p_2/p_1 = 0.6$, $\tilde{P}'_{rms} = 0.00631$, $T_w - T_\infty = 111.0$ K°

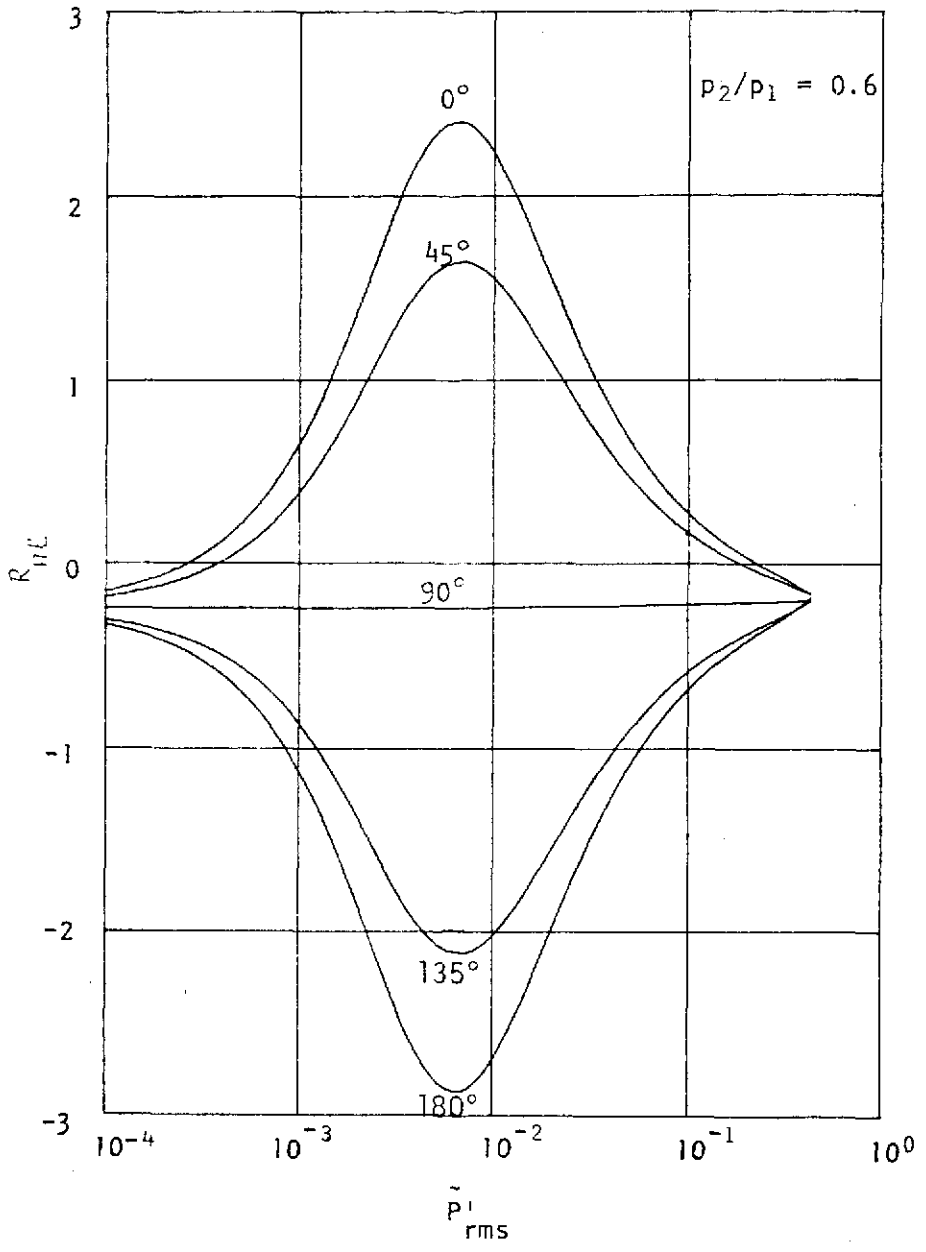

Figure 14. Response Factor Versus Root-Mean-Square Sound Pressure Level for Various Phase Angles Between Fundamental Sound Pressure Component and Its Harmonic; M = 0.005, $\phi_1 = \theta_1 = \theta_2 = 0$, $p_2/p_1 = 0.6$, $T_w - T_\infty = 111.0$ K°

shows the variation in $R_{n\ell}$ with root-mean-square sound pressure for various phase angles ϕ_2 between the fundamental and harmonic (distortion) component. Figure 15 is for the same conditions as figure 14 with the exception of the wire Mach number, which is zero in figure 15. Figures 13, 14 and 15 show the very strong influence of the phase angle on the response.

CONCLUSIONS

The results obtained for the analog process -- the output of a constant temperature hot-wire anemometer -- are qualitatively the same as those Heidmann obtained for vaporization limited combustion. There are small differences in the actual numbers involved, but this is to be expected since the equations for the two processes are slightly different. A scaling factor would be necessary to make a direct numerical comparison between the two, but this is unnecessary for the qualitative comparison done here.

The addition of distortion to sinusoidal perturbations of the environment of the hot-wire can increase the response significantly. Using the stability criterion of Heidmann [3] -- response factors greater than some value between 0.8 and 1.0 denote unstable operation (the oscillations will grow with time) -- the figures show that certain combinations of harmonic amplitude and phase angle will be unstable. The pure sinusoidal case, $p_2/p_1 = 0$, is always predicted to be stable. These results are examined experimentally in the next chapter.

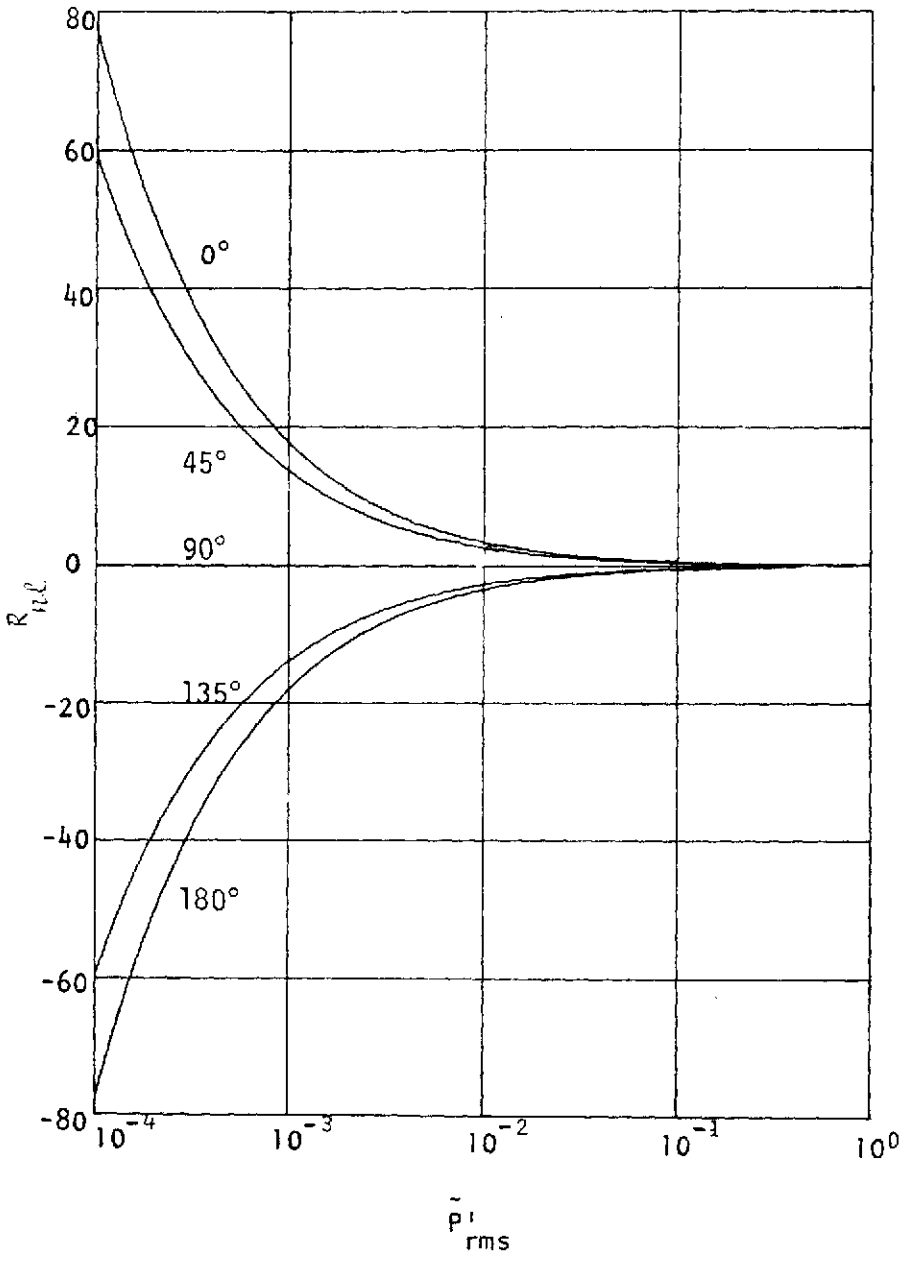

Figure 15. Response Factor Versus Root-Mean-Square Sound Pressure Level for Various Phase Angles Between Fundamental Sound Pressure Component and Its Harmonic; M = 0, $\phi_1 = \theta_1 = \theta_2 = 0$, $p_2/p_1 = 0.6$, $T_w - T_\infty = 111.0$ K°

Chapter 3

EXPERIMENTAL ANALYSIS

INTRODUCTION

The object of the experimental portion of the research is to determine the open-loop response of a constant-temperature hot-wire anemometer to sinusoidal and distorted sinusoidal acoustic oscillations, in the same way as was done analytically; and, through this, to gain insight into the closed-loop performance of the system. An experimental system was set up which would produce the same acoustic environment for the hot wire as was used in the analytical portion of the work (to the extent possible within the physical limitations of the system). With it the measurements required to determine the response could be made. The system consisted of four basic parts -- the test section itself, the means of generating the necessary acoustic oscillations, the means of making the necessary measurements to determine the response and the various types of equipment needed to calibrate and monitor the performance of all other parts of the system.

Before arriving at the system which is described later in this chapter, the system went through many design modifications. Each of the four basic parts caused its own special problems. Some of the tests done on the interim system configurations resulted in important decisions concerning the scope of the research and the acoustic fields

used. These decisions had significant effects on the design of the equipment so they will be discussed first.

No Through Flow

It was originally planned that data would be taken with no through flow through the chamber (M = 0) and with various amounts of constant axial flow through the chamber, as was done analytically. A cylindrical test section was built with perforated end plates. To generate the flow, the test section was connected via a sheet metal cone and flexible tubing to a fan which drew air through the system. This system is shown in figure 16.

When the chamber was tested to determine its resonant frequencies, it was found that the experimentally determined frequencies did not agree with those obtained from equation (A.39). Further investigation showed that there was spatial distortion of the acoustic field due to the holes in the end plates. When the same resonance test was done with solid end plates on the chamber, the experimental and theoretical frequencies were virtually identical. The results of the tests are listed in table 1. Not all the predicted frequencies appeared due to the location of the microphone used to detect resonance. The microphone was at a pressure node for some of the resonant frequencies. Higher resonant frequencies also existed, but those shown are sufficient to establish a basis of comparison.

Because of the distortion caused by the holes in the end plates, the analytical and experimental analyses would not be the same. Examination of figure 12 showed that the no-flow condition is the one that is most sensitive to acoustic perturbations -- the value of the sound level at

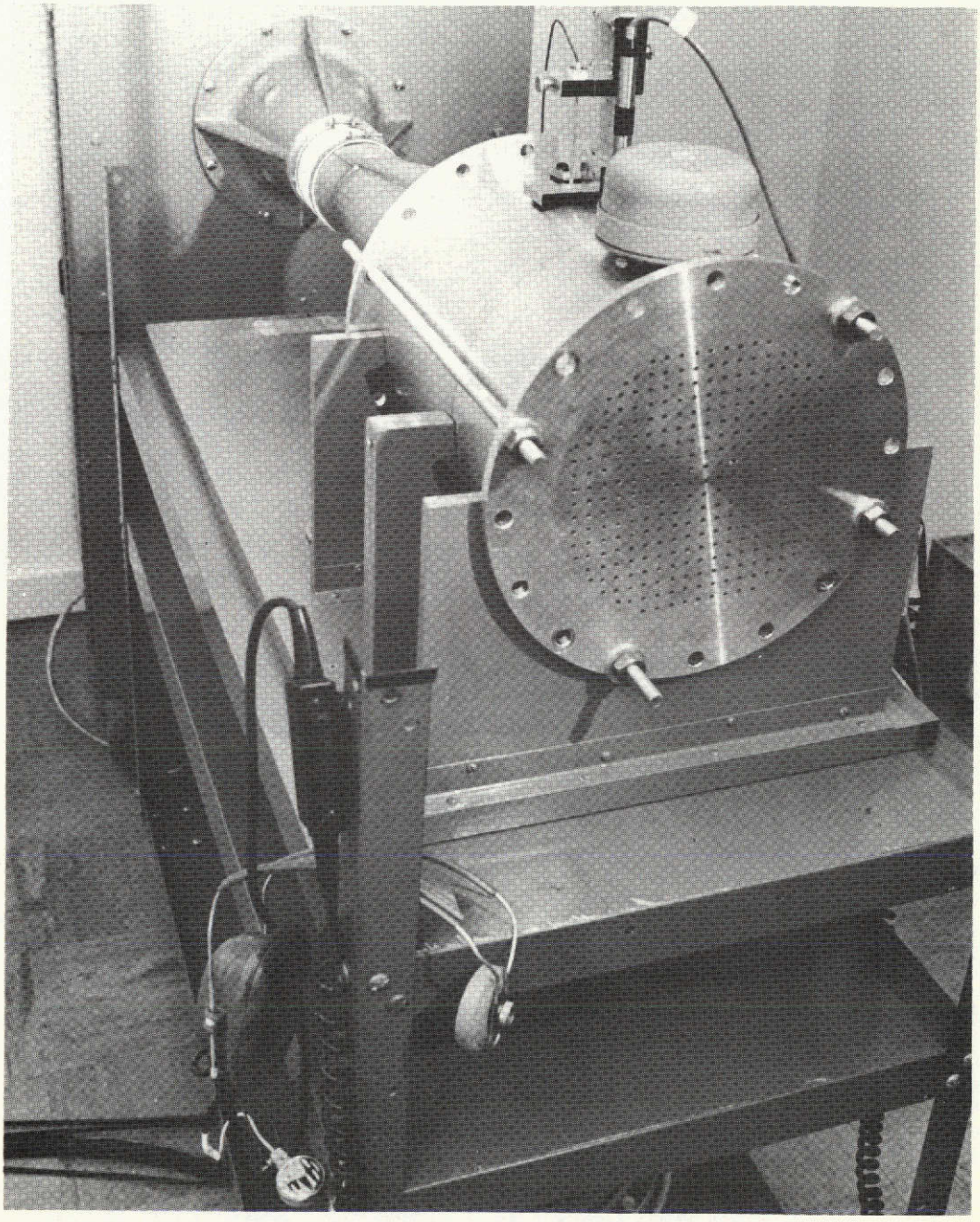

Figure 16. Photograph of the First Experimental System

Table 1. Resonant Frequencies (77°F)

Mode mnn_z	Theoretical (Hz)	Experimental	
		Holes (Hz)	No Holes (Hz)
001	556	583	556
100	990	1010	990
002	1112	1128	1113
101	1135	1192	1135
102	1489	1547	1490
200	1642	1661	1651
003	1669	1672	1667
201	1734	1765	1750
103	1941	--	--
202	1983	2020	1981
010	2060	2068	2059
011	2134	2151	2134
004	2225	2263	2221
300	2259	2284	2257
301	2326	2345	2330
012	2341	2374	2339
203	2341	2374	2339
104	2435	2491	2432
302	2518	2550	2515

which the peak response occurs decreases with decreasing Mach number and the lower the Mach number, the greater the response factor. Hence, it was decided to restrict the experimental work to a truly closed ended cylinder with $\bar{M} = 0$. It was felt that sufficient information could be obtained from just the no-flow situation to determine the validity of the analysis.

Combination Mode

Another major experimental difficulty, which was discussed briefly in Chapter 2, was caused by Heidmann's characterization of the distorted acoustic field as being the sum of the first spinning tangential mode and the second spinning tangential mode with

$$f_{200} = 2f_{100}$$

This is not true experimentally, as can be seen in table 1, or analytically, as indicated in equation (A.38). Examination of this equation shows that for the first two pure tangential modes

$$\frac{f_{200}}{f_{100}} = \frac{\alpha_{20}\pi}{\alpha_{10}\pi} = 1.6604 \qquad (3.1)$$

and, therefore, f_{200} is not equal to twice f_{100}. The ratio of the two is always the same and it is determined by the first zeros of the Bessel functions

$$J_1'(\alpha_{10}\pi) = 0 \qquad (3.2a)$$

and

$$J_2'(\alpha_{20}\pi) = 0 \qquad (3.2b)$$

Values of α_{mn} are given in Appendix B.

The ratio of the resonant frequency of a combination mode to that of the first tangential mode, however, is not only dependent on the zeros of a Bessel function but it is also dependent on the length and radius of the chamber,

$$\frac{f_{mnn_z}}{f_{100}} = \left[\frac{(\alpha_{mn}/R)^2 + (n_z/L)^2}{(\alpha_{10}/R)^2} \right]^{0.5} \tag{3.3}$$

The ratio of the two can be altered by changing the length or radius or both. Changing the radius changes f_{100} and f_{mnn_z}; changing the length only affects f_{mnn_z}.

Examination of the acoustic equations for a (202) mode (equations (A.48) with m = 2, n = 0, n_z = 2) showed that although this mode has a longitudinal component of velocity, a longitudinal velocity node exists at the center of the chamber and that the equations for the pressure and tangential and radial velocities at the center have the same spatial relationships as the pure second tangential mode. Hence, the length of the chamber was adjusted so that

$$f_{202} = 2f_{100} \tag{3.4}$$

and the wire was positioned in the central cross section of the chamber. In this way the distorted acoustic oscillations used by Heidmann would be simulated as was shown in Chapter 2.

APPARATUS

A schematic diagram of the principal parts of the experimental system is shown in figure 17. Each of these parts is described, as is the additional equipment needed to calibrate and monitor the system.

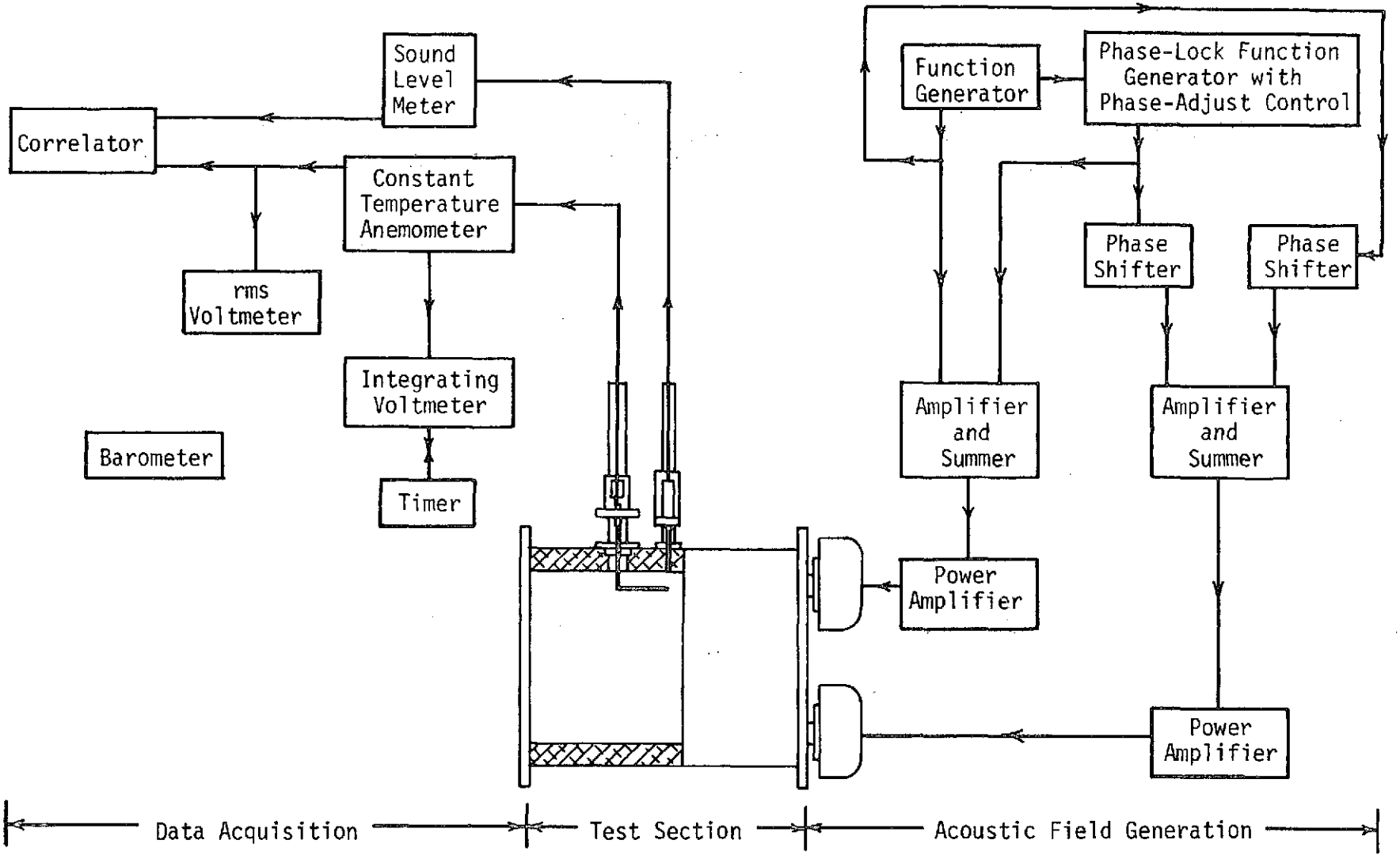

Figure 17. Schematic Diagram of the Experimental System

Test Section

The test section was originally designed to be part of a system which had a through-flow velocity and which would be excited by (100) and (200) pure spinning tangential modes of resonance. As was just discussed, this did not turn out to be the actual experimental conditions used. Rather than making a new test section, the original one was modified to meet the changing demands. Also, when any design modifications were made, an effort was made to anticipate as many future needs as possible. Because of these things, the chamber has some features which are not needed for the present experiments, but which will be described for the sake of completness.

Figure 18 is a photograph of the test section; it is an aluminum cylinder with a 20.49 cm (8.068 in.) I.D., 25.319 cm (9.968 in.) O.D. and length of 31.198 cm (12.283 in.). The cylinder is composed of two sections, one 12.70 cm (5.000 in.) long and the other 18.500 cm (7.283 in.) long, which are mated by means of a lap joint containing an O-ring seal. The longer section has provisions for mounting the hot-wire probe and the microphone from which the response factor is obtained, as well as other devices to examine the acoustic field. The shorter section has three threaded holes, for the mounting of acoustic drivers, located at its central transverse section, 90 and 180 degrees apart. When not in use, these holes are closed with threaded plugs which maintain the proper curved contour of the inside surface of the chamber. The cylinder was made in two sections so the angular position of the probe could be changed relative to the angular position of the drivers on the other section.

The ends of the cylinder are closed with plexiglass end plates.

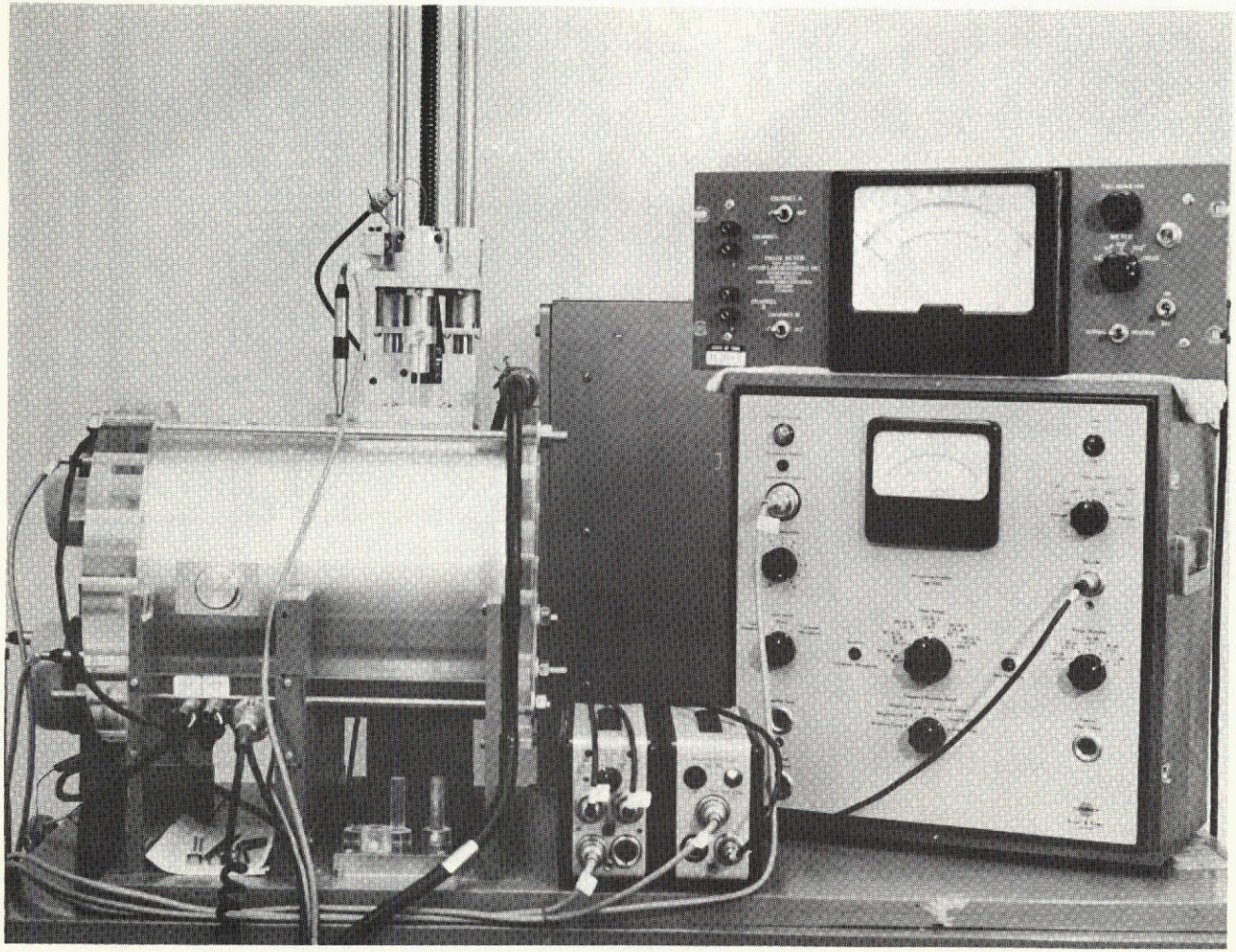

Figure 18. Photograph of the Test Section

At one end are two 1.27 cm (0.50 in.) thick end plates. (The second one is for added structural rigidity.) Four 0.254-cm (0.10 in.) diameter holes are located at 0, 90, 180 and 270 degrees at r = 9.20 cm (3.62 in.). These holes were made to permit investigation of the longitudinal variations of the pressure in the chamber. They are large enough to permit a 2.0 mm (0.079 in.) diameter microphone probe tube extension to pass through them.

At the other end of the cylinder is a 5.08 cm (2.00 in.) thick end plate in which provision has been made for mounting three acoustic drivers and three microphones to monitor the sound field. The end plate must be thick to be able to support the heavy drivers without distorting the shape of the end plate. Plugs are available to close any holes not in use. Figure 19 is a photograph of the driver end plate with two drivers and three microphones mounted on it. The third driver hole is closed with a plug.

Use of the (100) and (202) modes of vibration with the requirement that

$$f_{202} = 2f_{100} \tag{3.4}$$

means the permissible values of length and diameter are functionally dependent, as is expressed in equation (3.3). To comply with this equation, the existing chamber either had to have a smaller radius, a greater length or modifications of both dimensions. To avoid having to make an entirely new chamber, the existing chamber was given a longer effective length by machining a disc 0.051 cm (0.020 in.) thick and of the chamber diameter out of each of the end plates. This resulted in

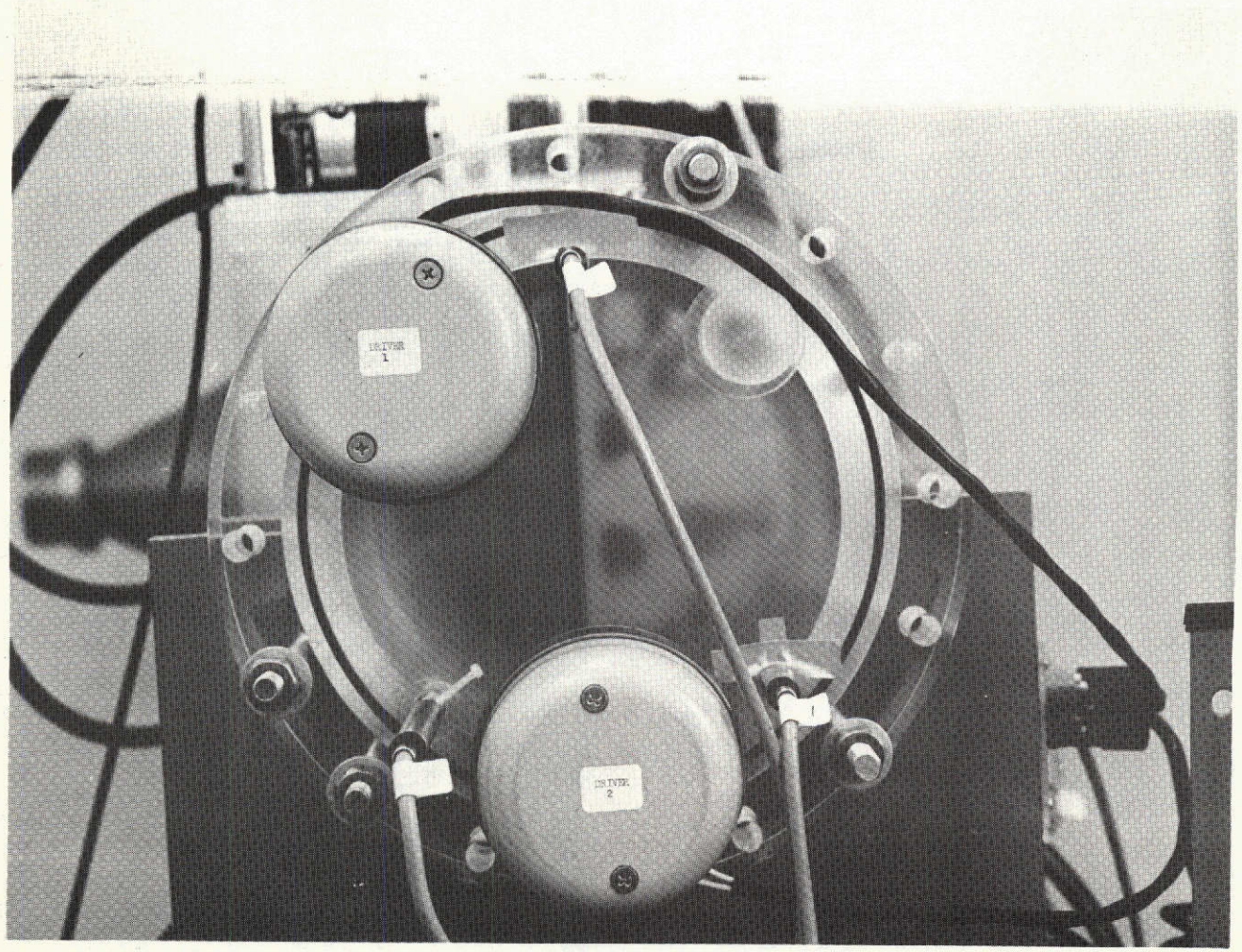

Figure 19. Photograph of an End Plate of the Test Section

the chamber having an effective overall length of 31.30 cm (12.323 in.) and meeting the requirement of equation (3.4).

The cylinder and end plates have O-ring seals between them and the whole system is clamped together with four long bolts. The chamber rests in a wooden cradle which has supports at both ends and at the lap joint.

On the longer cylindrical section there are two probe access holes and over each of these is provision for the mounting of a probe holding and positioning device. One of the holes is located at the central cross-section of the cylinder and is 1.77 cm (0.50 in.) in diameter. This size permits the use of a 1.77 cm (0.50 in.) diameter microphone at this location, or smaller probes by means of appropriatly sized plexiglass inserts.

The second access hole is designed for use with a Disa right-angle miniature hot-wire probe holder. The hole itself is 1.905 cm (0.750 in.) in diameter at the bottom and 3.81 cm (1.50 in.) in diameter at the top (refer to figure 17). The large size is necessary to be able to insert the right-angle probe holder. After insertion a plexiglass sleeve, made in two halves, is placed around the probe holder leaving only a 0.474 cm (0.187 in.) diameter hole in which the 0.318 cm (0.125 in.) diameter probe holder can move. The center of the hole is located 7.00 cm (2.756 in.) from the central cross-section of the cylinder so that when the right-angle probe holder is being used the hot wire itself is located at the center of the cylinder and is on the same radial line as that which extends to the first probe site. Figure 20 is a photograph of the Disa right-angle probe holder, a hot-wire probe and the plexiglass insert. With suitable plexiglass inserts other probes can also be used

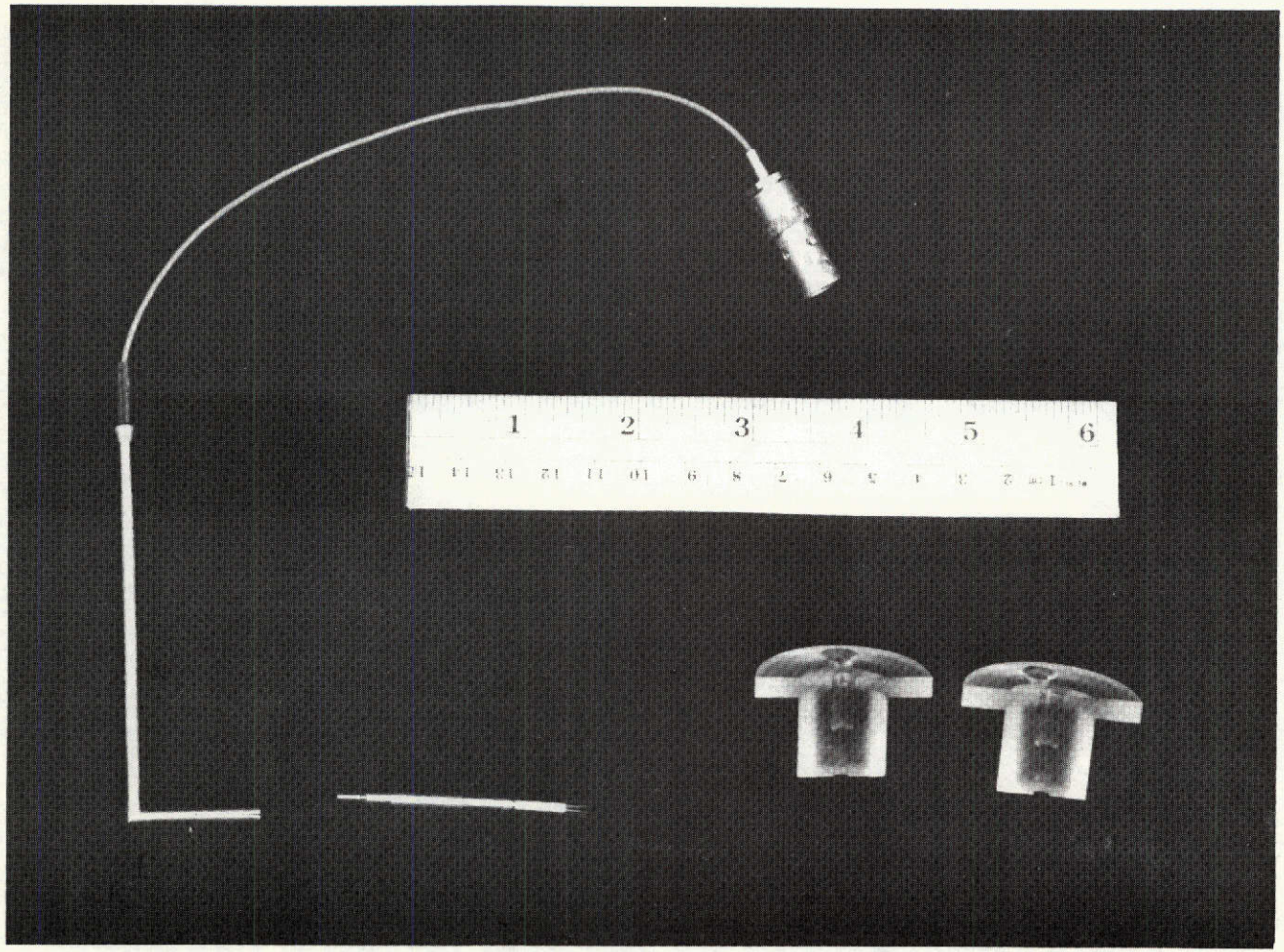

Figure 20. Photograph of the Disa Right-Angle Miniature Probe Holder, A Hot-Wire Probe and the Plexiglass Insert

at this location. The plexiglass inserts around the probes also act as electrical insulators between the probes and the test section and aid in preventing ground loops.

Two probe holding positioners are available for use on the test section -- one manually adjusted and one electrically activated device. The manually adjusted holder has a vernier scale with which a probe can be positioned to within 0.25 mm (0.01 in.). It is shown in figure 21 along with the inserts used to adapt it to the various probes. The electrically actuated holder (L. C. Smith BBR 24 180) has a remote control and readout device (L. C. Smith DI 3-R) associated with it -- the probe location can be adjusted and the resulting position read from a digital voltmeter, with an accuracy of 0.65 mm (0.025 in.), at a location remote from the device itself. The photograph of figure 18 shows this probe holder mounted on the test section.

Acoustic Field Generation System

The investigation requires that the combination of a (100) and (202) spinning acoustic field be generated and that the relative amplitudes and phases of these fields be adjustable with respect to one another. Since the frequency of resonance changes with temperature, and since chamber resonance studies are to be done, the frequency of the acoustic generation system also has to be adjustable. The number and location of the acoustic drivers is discussed first, then the means of generating the necessary oscillations to activate the drivers is explained.

Driver location. As was discussed in Chapter 1, the acoustic drivers need to be located near pressure antinodes of the particular

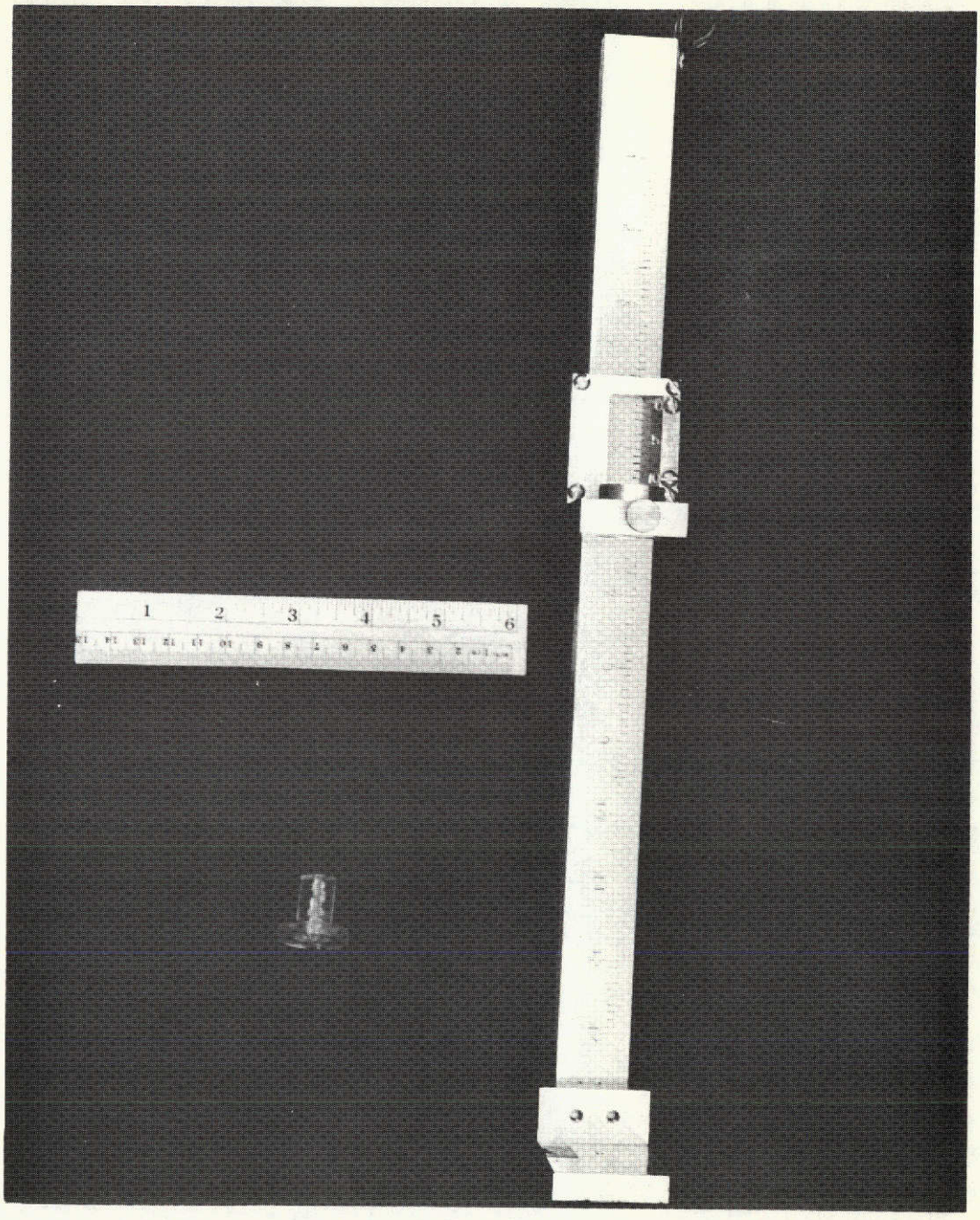

Figure 21. Photograph of the Manually Adjusted Probe Holding and Positioning Device

mode desired. For the (100) and (200) modes, the choice includes any location for which $r = R$ and $0 \leq z \leq L$. For the (202) mode, the pressure antinodes are at $r = R$, but the longitudinal positions of the antinodes are restricted to 0, L/2 and L. The original location of the drivers -- at the central cross-section of the shorter cylindrical section -- was very close to a (202) pressure nodal position rather than an antinodal position. Thus the location of the drivers had to be changed. The center, $z = L/2$, was difficult to utilize since the microphone, the hot-wire probe holder and the cradle supporting the test section obstructed access. Elimination of the flow through the chamber (solid end plates) meant the ends of the chamber could be used as probe and driver sites; hence, the drivers were mounted on one of the end plates.

In Appendix A, a spinning mode is shown to be the sum of two standing waves of equal amplitude but 90/m degrees out of phase with each other in angular position and 90 degrees out of phase in time. This indicates that to generate a spinning (100) mode, two drivers are needed separated by 90 degrees. To generate a spinning (202) mode, two drivers, separated by 45 degrees, are needed. Trigonometric manipulation of the equations shows that the same effect is achieved by putting the "second" driver at any pressure node of the acoustic field of the "first" driver. For the (202) mode this would be at 45, 135, 225 or 315 degrees with respect to the first driver.

Referring to figure 19, three driver sites are available -- 1 and 3, which are 90 degrees apart and therefore are suitable to drive the (100) mode, and 1 and 2, which are 135 degrees apart and are suitable to drive the (202) mode. In practice it was found that the (100) mode

could also be driven using 1 and 2; hence, only two drivers were actually used. The drivers are University Sound ID-75 driver units, rated at 75 watts. Experience has shown that they cannot be used at this level when being driven by a pure tone, or a pure tone with one of its harmonics, without overheating. Most of the experiments were done with less than 10 watts to each driver.

Driver input signal generation. The system used to generate the signals required to activate the drivers was shown in figure 17. Figure 22 shows the same system, only in more detail. A General Radio (GR) 1309-A oscillator with a sinusoidal output is the basis of the sound generation system. The output frequency is adjustable from 10 Hz to 100 kHz. The GR is tuned to the fundamental (100) frequency and its output is fed to the Wavetek 115 function generator, which uses it as a basis for generating a sine wave at the second harmonic (202) frequency. The Wavetek requires a signal of about 5 volts to be able to accurately frequency and phase lock to the GR. This is close to the maximum output of the GR. Because of this the amplitude adjustment of the GR cannot be used. Instead the amplitude is adjusted by means of an auxilliary voltage dividing potentiometer. When the frequency of the GR is changed, the frequency of the Wavetek also changes and maintains the proper 2 to 1 ratio.

The phase of the Wavetek signal can be adjusted relative to the GR signal. This phase adjustment is limited to about 80 degrees. The Wavetek has, in addition to its sinusoidal output, a negative sinusoidal output. By using this, an additional 80 degrees variation in phase can be obtained. When not in the frequency and phase lock mode, the output

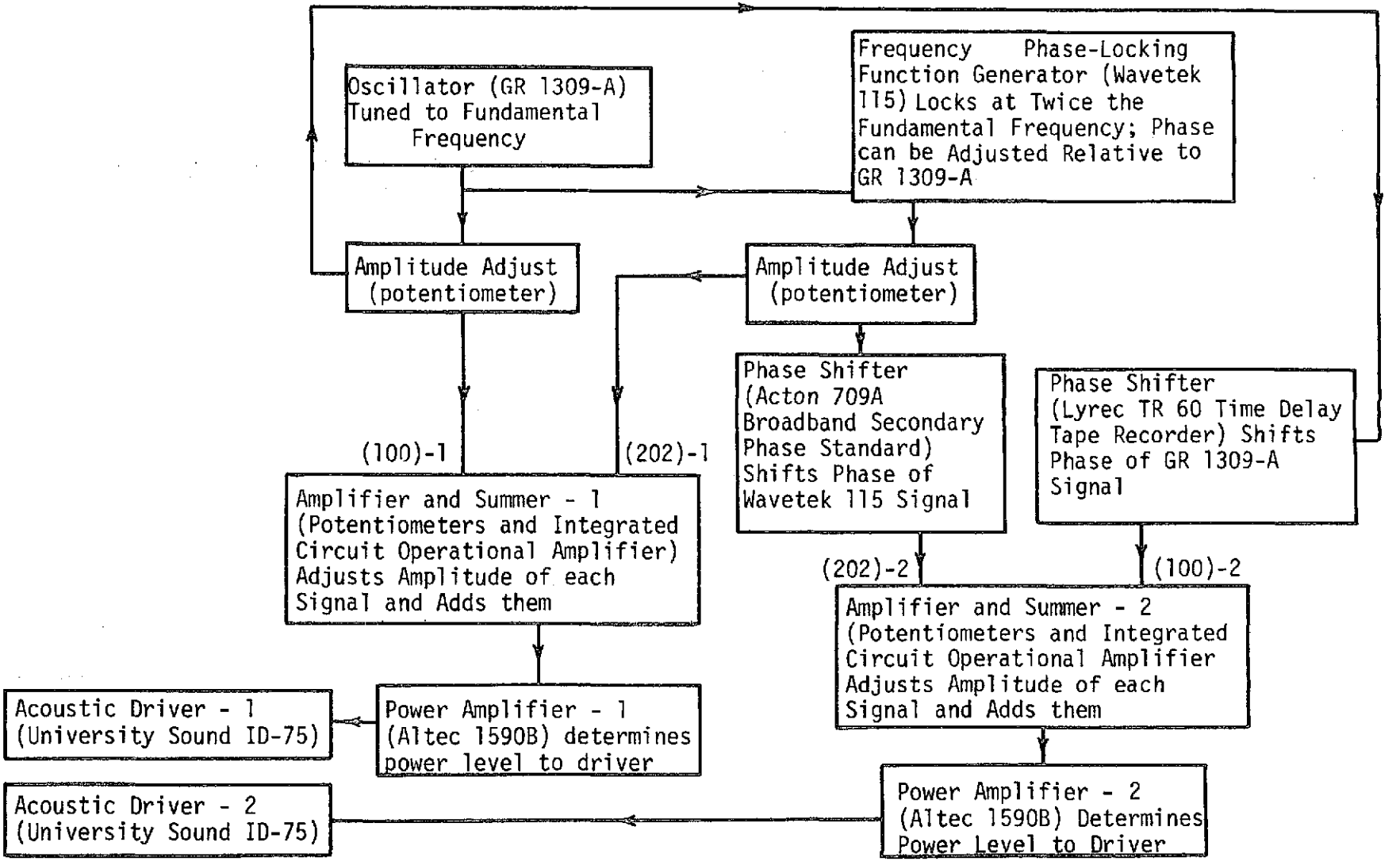

Figure 22. Schematic Diagram of the System used to Generate the Acoustic Fields

frequency of the Wavetek is determined by the settings on its frequency control knobs, or is determined by the level of a D.C. input voltage. The amplitude adjustment of the Wavetek is not very sensitive. To obtain better control, a voltage dividing potentiometer was added.

To activate driver 1, further fine adjustments of the amplitudes of each of the signals is made by means of two potentiometers; the two signals are then summed, fed to an Altec 1590-B power amplifier and then to driver 1. The summer is made from a Union Carbide UC4201 semiconductor integrated circuit operational amplifier, powered by a Kepco SC-36-1M regulated D.C. power supply.

The signals to driver 2 each have to be phase shifted relative to the signals to driver 1. The amount of phase shift is different for each signal; hence, two phase shifters are needed. The fundamental frequency is shifted by means of a Lyrec TF 60 time-delay tape recorder operating in the loop mode; the harmonic frequency is shifted by means of an Acton 709 A broadband secondary phase standard. After the phase shifts, fine adjustments are made to the amplitudes of each of the signals by means of two potentiometers. The signals are summed, fed to a second Altec 1590 B power amplifier and then to driver 2. The second summer is identical to the first. When less complex acoustic fields are needed, parts of the system are simply not used.

The photograph of figure 23 includes the GR and Wavetek function generators, potentiometer amplitude adjustors, the Acton phase shifter, and the Altec power supplies. The photograph of figure 24 includes the Lyrec tape recorder, which is used as a phase shifter, the amplifying and summing devices and the power supply for the summers.

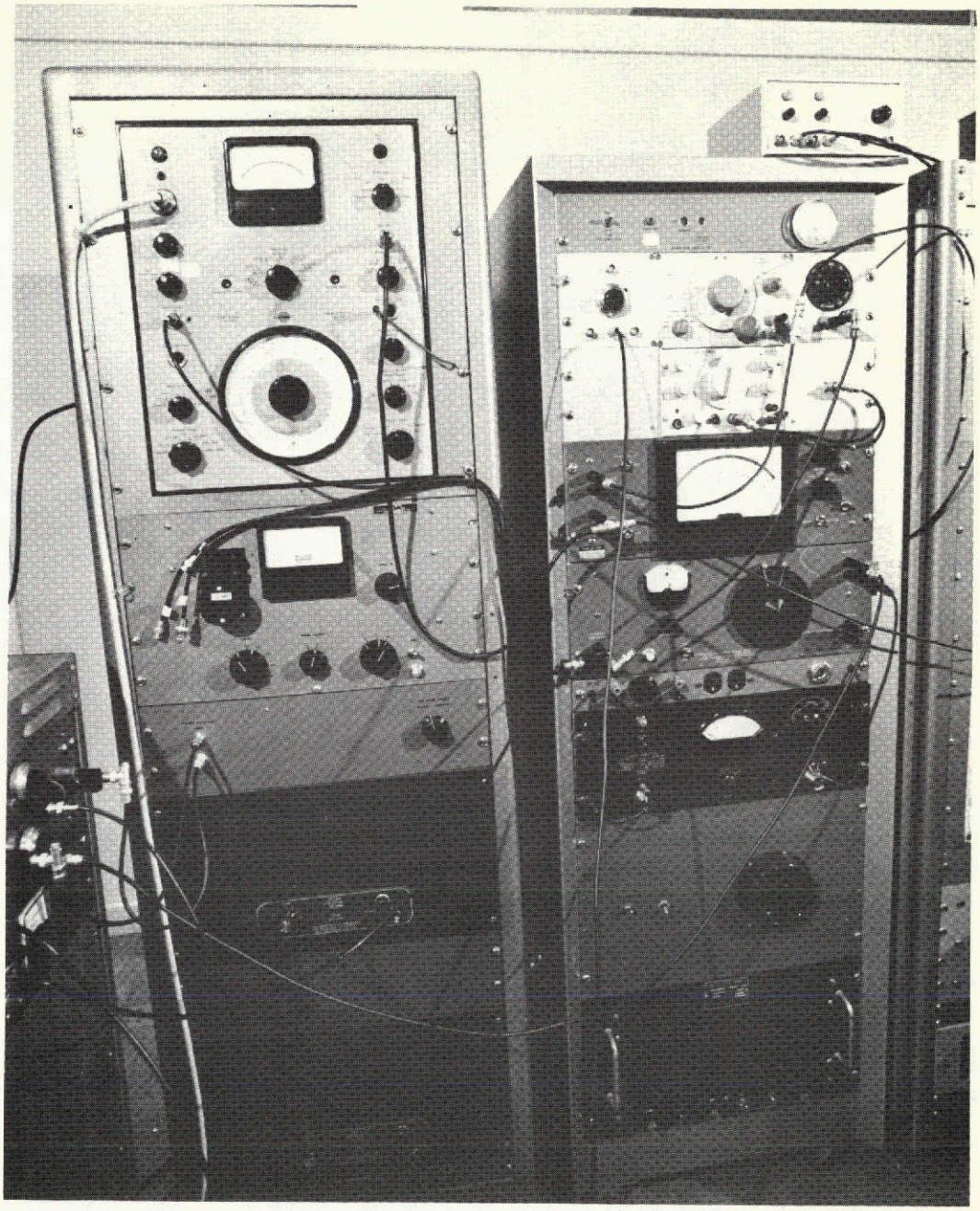

Figure 23. Photograph which shows the B&K Frequency Analyzer, Fluke VAW Meter, Altec Power Amplifiers, GR Oscillator, Wavetek Function Generator, Voltage Dividing Potentiometers, Acton Phase Meter, Acton Phase Shifter and Stabiline Voltage Regulator.

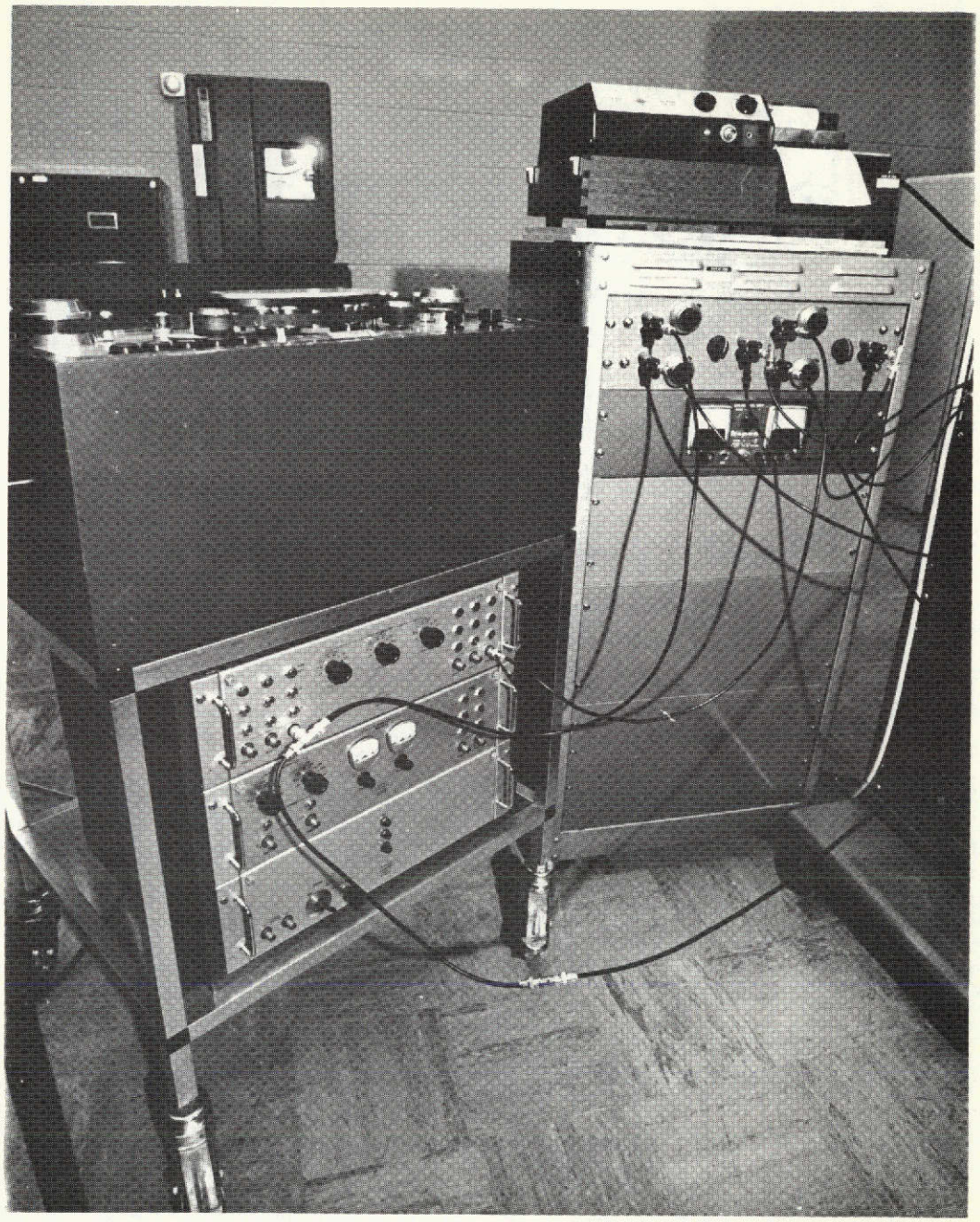

Figure 24. Photograph which shows the Lyrec Time Delay Tape Recorder, B&K Level Recorder, Amplifying and Summing Devices and Associated Kepco D.C. Power Supply

The Lyrec recorder has a 300-inch tape loop adapter mounted on it. When operated in a loop, a blip appears in the output signal every time the splice in the tape which forms the loop passes over the read heads. To reduce the frequency of occurrence of the blip, the permissible length of the tape loop is increased by use of the adapter. Without it the recorder can handle only an 80-inch loop.

Data Acquisition System

The main property to be determined is the in-phase response factor $R_{n\ell}$. It is a measure of the interaction between the anemometer output and the perturbations in the pressure and was defined as

$$R_{n\ell} = \frac{\int_0^{2\pi} \tilde{E}' \, \tilde{P}' \, d(\omega t)}{\int_0^{2\pi} (\tilde{P}')^2 \, d(\omega t)} \tag{2.30}$$

No equipment is available which will determine this quantity directly; however, it is obtainable from the correlation coefficient, which can be determined experimentally.

The correlation coefficient is defined as

$$R = \frac{\overline{E' \, P'}}{E'_{rms} \, P'_{rms}} \tag{3.5}$$

The response factor is obtained from R as follows:

From equation (2.30)

$$R_{n\ell} = \left[\frac{\overline{E' \, P'}}{\overline{(P')^2}} \right] \left[\frac{\bar{P}}{\bar{E}} \right] \tag{3.6}$$

Equation 3.6 may be rewritten as

$$R_{n\ell} = \left[\frac{\overline{E'\,P'}}{E'_{rms}\,P'_{rms}}\right]\left[\frac{E'_{rms}}{P'_{rms}}\right]\left[\frac{\overline{P}}{\overline{E}}\right] \tag{3.7}$$

Therefore,

$$R_{n\ell} = R\left[\frac{E'_{rms}}{P'_{rms}}\right]\left[\frac{\overline{P}}{\overline{E}}\right] \tag{3.8}$$

Hence, to determine $R_{n\ell}$, an instrument which can convert the anemometer fluctuations E' and pressure fluctuations P' into the correlation coefficient is needed, as well as equipment to measure E'_{rms}, P'_{rms}, the atmospheric pressure $\overline{P}$ and the time mean of the anemometer voltage $\overline{E}$. The system used is shown in figure 17. Figure 25 shows it in more detail.

The hot-wire probe used is a Disa 55F31 platinum-plated tungsten miniature hot-wire probe mounted on a Disa right-angle miniature probe support. Figure 20 shows both of these. The hot-wire is controlled by a Disa 55A01 constant temperature anemometer. The anemometer has two outputs -- a bridge output, $E = \overline{E} + E'$, and a turbulence output E'. The anemometer is shown in figure 26.

The fluctuations in pressure P' are sensed by a Brüel & Kjaer (B&K) 4136 0.635 cm (0.25 in.) condenser microphone cartridge and B&K cathode follower. The power supply for this instrument is a B&K 2107 frequency analyzer, which can be seen in figure 23. The frequency analyzer is also able to measure the sound pressure level, from which P'_{rms} can be obtained, and perform frequency analyses of the microphone signal.

The sound pressure level Lp is defined as,

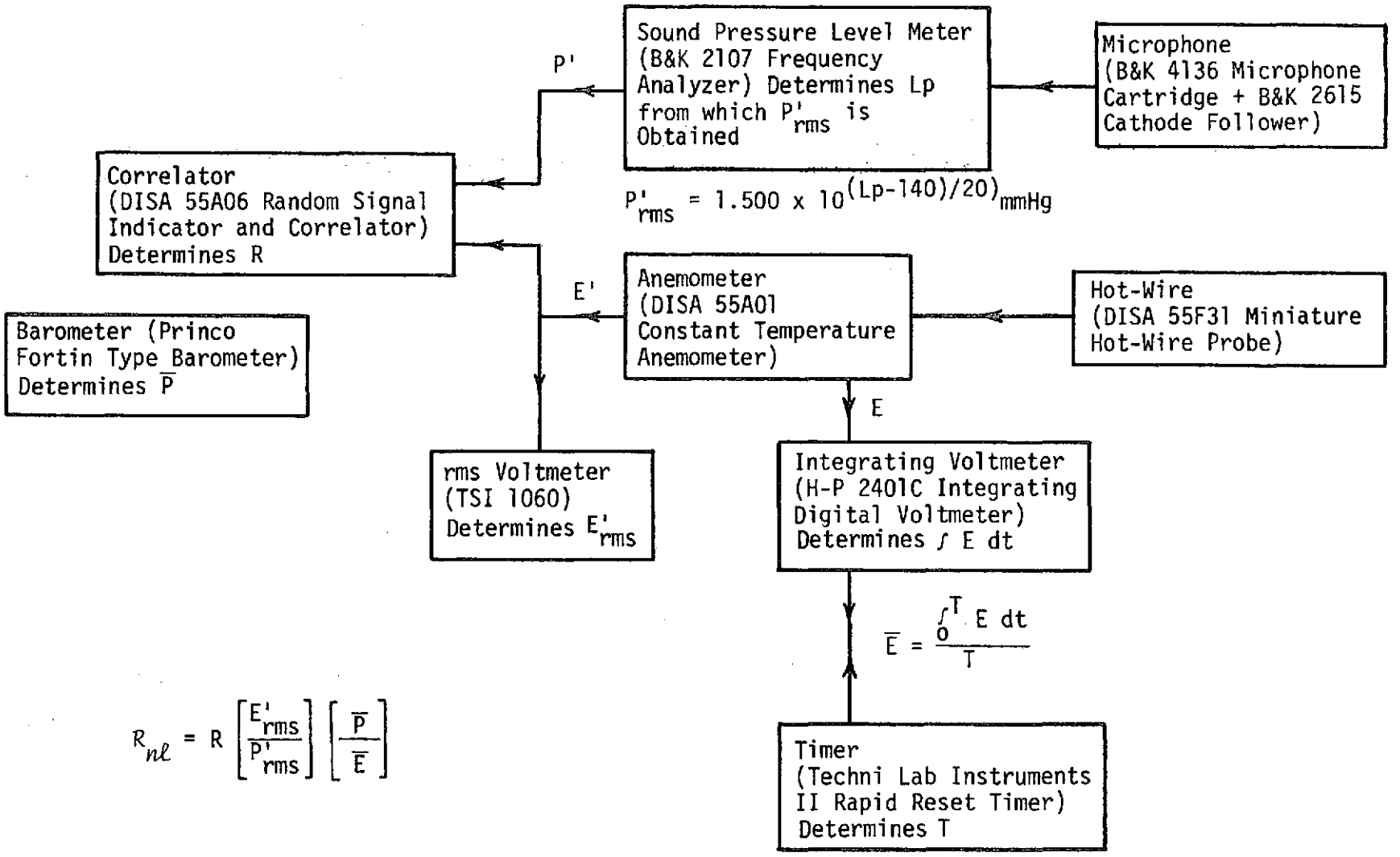

Figure 25. Schematic Diagram of the System used to Obtain the Response Factor, $R_{n\ell}$

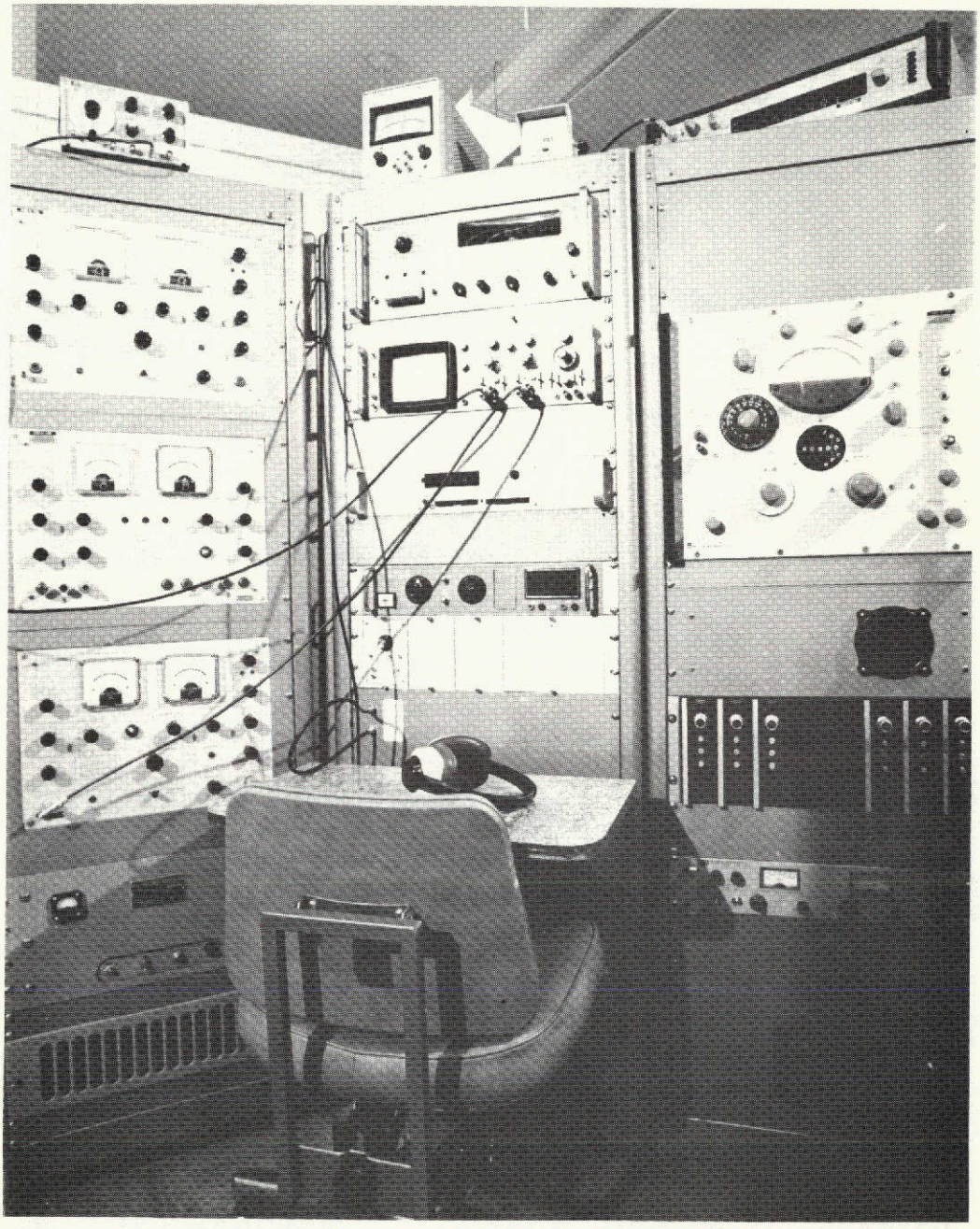

Figure 26. Photograph which shows the Disa Random Signal Indicator and Correlator, Disa Constant Temperature Anemometer, TSI rms Voltmeter, Techni Lab Timer, H-P Integrating Voltmeter, H-P Oscilloscope, California Instruments Multimeter, L.C. Smith Probe Actuator, MKS' Baratron Pressure Transducer and Switch

$$Lp \equiv 20 \log_{10} (P'_{rms}/P_{ref}) \tag{3.9}$$

where

$$P_{ref} \equiv 20\ \mu N/m^2 \tag{3.10}$$

Solving equation (3.9) for P'_{rms},

$$P'_{rms} = P_{ref}\ 10^{Lp/20} \tag{3.11}$$

The outputs from the sound level meter and anemometer are fed to a Disa 55A06 random signal indicator and correlator, which determines the correlation coefficient R. The correlator is pictured in figure 26.

A Thermo Systems Inc. (TSI) 1060 rms voltmeter is used to obtain E'_{rms} from E'. A Princo Fortin type barometer is used to obtain $\overline{P}$. To determine $\overline{E}$ a Hewlett-Packard (HP) 2401C integrating digital voltmeter is used in conjunction with a Techni Lab Instruments II timer. They are interconnected so that when the timer is started, the voltmeter starts integrating with respect to time, $\int_0^t E\ dt$. When the timer is stopped, the voltmeter also stops. Dividing the integrated voltage by the time elapsed determines $\overline{E}$, i.e.,

$$\overline{E} = \frac{\int_0^T E\ dt}{T} \tag{3.12}$$

The TSI rms voltmeter, the HP integrating voltmeter and the timer are shown in figure 26.

Calibration and Other Auxiliary Equipment

To make a comparison between the analytical and experimental results, the equation relating the velocity to the voltage output from

the anemometer, equation (2.17), must be the equation which fits the particular hot wire being used in the experiment. To obtain this equation the hot wire must be calibrated. Also, the microphones used had to be calibrated and the acoustic fields generated had to be verified. In addition to the above, a resonant frequency analysis of the chamber was performed (as was mentioned at the beginning of this chapter); and the frequency of the various signals, the power to the drivers and the ambient temperature were monitored. Frequency spectrum analyses were done on both the anemometer and microphone outputs. Also, due to the intensity of the sound during operation, the test section had to be enclosed by an acoustic shield.

Wire calibration equipment. The equipment used for the hot-wire calibration is shown photographically in figure 27 and schematically in figure 28. It consists of a Disa 55D41/42 low turbulence calibrating wind tunnel, an MKS Baratron 170M-5A pressure meter, a Neff 122 D.C. amplifier, a Meriam 34FB2 micromanometer, the anemometer, the integrating voltmeter-timer system described previously and a switch which allows either the output of the anemometer, or the output of the Neff amplifier, to be the input to the integrating voltmeter.

The wind tunnel has provision for the mounting of a wire in the flow. The amount of flow is adjusted by a variable transformer which controls the tunnel blower motor. The velocity of flow is determined by measuring the static pressure difference between the inlet to the nozzle and the axial location of the hot wire. This pressure difference is sensed by the MKS Baratron pressure transducer, a capacitance manometer which converts the pressure difference to a voltage output. The

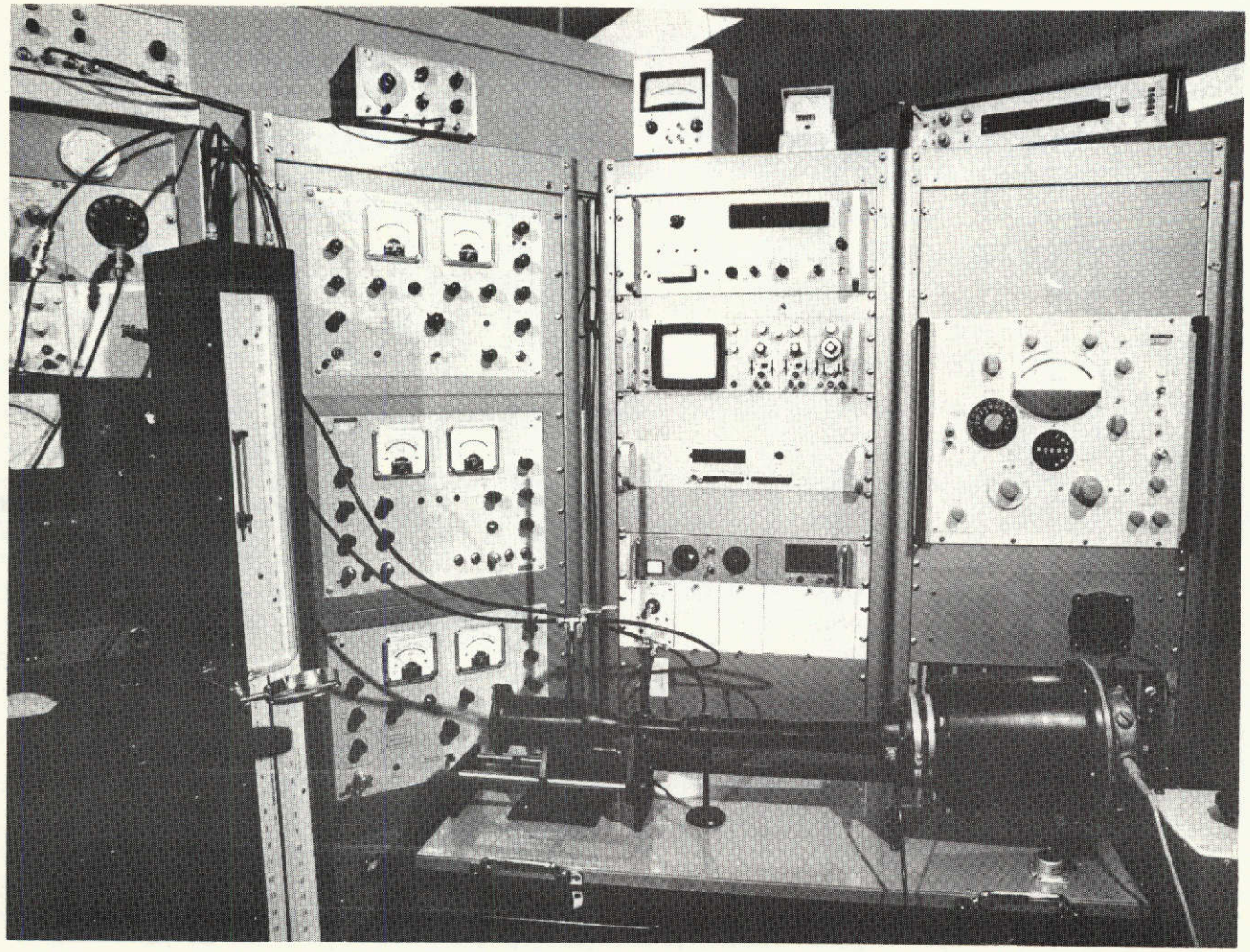

Figure 27. Photograph of the Equipment used for Hot-Wire Calibration

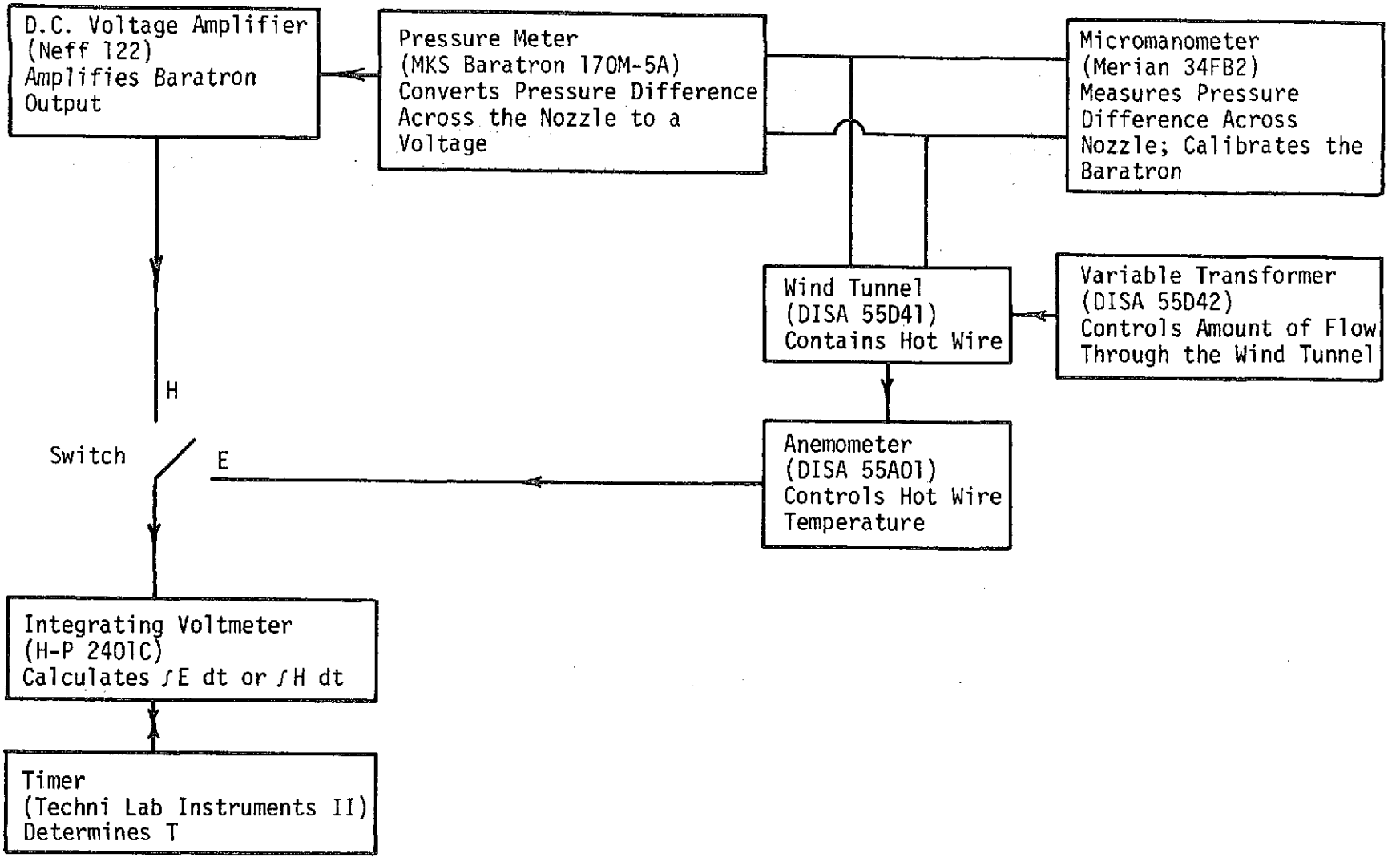

Figure 28. Schematic Diagram of the System used for Hot-Wire Calibration

voltage outputs for the velocities being considered (less than 3 m/sec) are small, so the Neff amplifier is used to increase them. The Baratron-Neff amplifier combination is calibrated using the Meriam micromanometer. The micromanometer is not sensitive enough to be able to accurately determine the pressure differences associated with velocities below about 1 m/sec. Hence, the micromanometer is used to calibrate the Baratron-Neff combination at higher velocities and the calibration, which is linear, is extrapolated to the lower velocities.

Microphone calibration. To calibrate the microphones, a B&K 4220 pistonphone is used. The pistonphone produces a sound pressure level of 124.0 dB ($\pm$ 0.2 dB) plus a correction factor determined by the barometric pressure. A barometer is supplied with the pistonphone which converts the barometric pressure reading to the necessary correction factor. Adaptors are available to fit the opening of the pistonphone to various microphones. Figure 29 shows the pistonphone being used to calibrate a microphone. The barometer and adaptors are also shown.

Acoustic field verification. Prior to taking data, the presence of the desired acoustic fields had to be verified. Initially, rather extensive investigations of the acoustic fields were performed. Once the ability of the equipment to generate the necessary acoustic fields was demonstrated, the procedure for setting up the acoustic fields was followed and the resulting sound field was used for actual data taking without further verification.

From equation (A.48a) the variations in the pressure in the chamber with respect to both space and time can be determined. To verify the existence of a particular mode of vibration, these analtyical

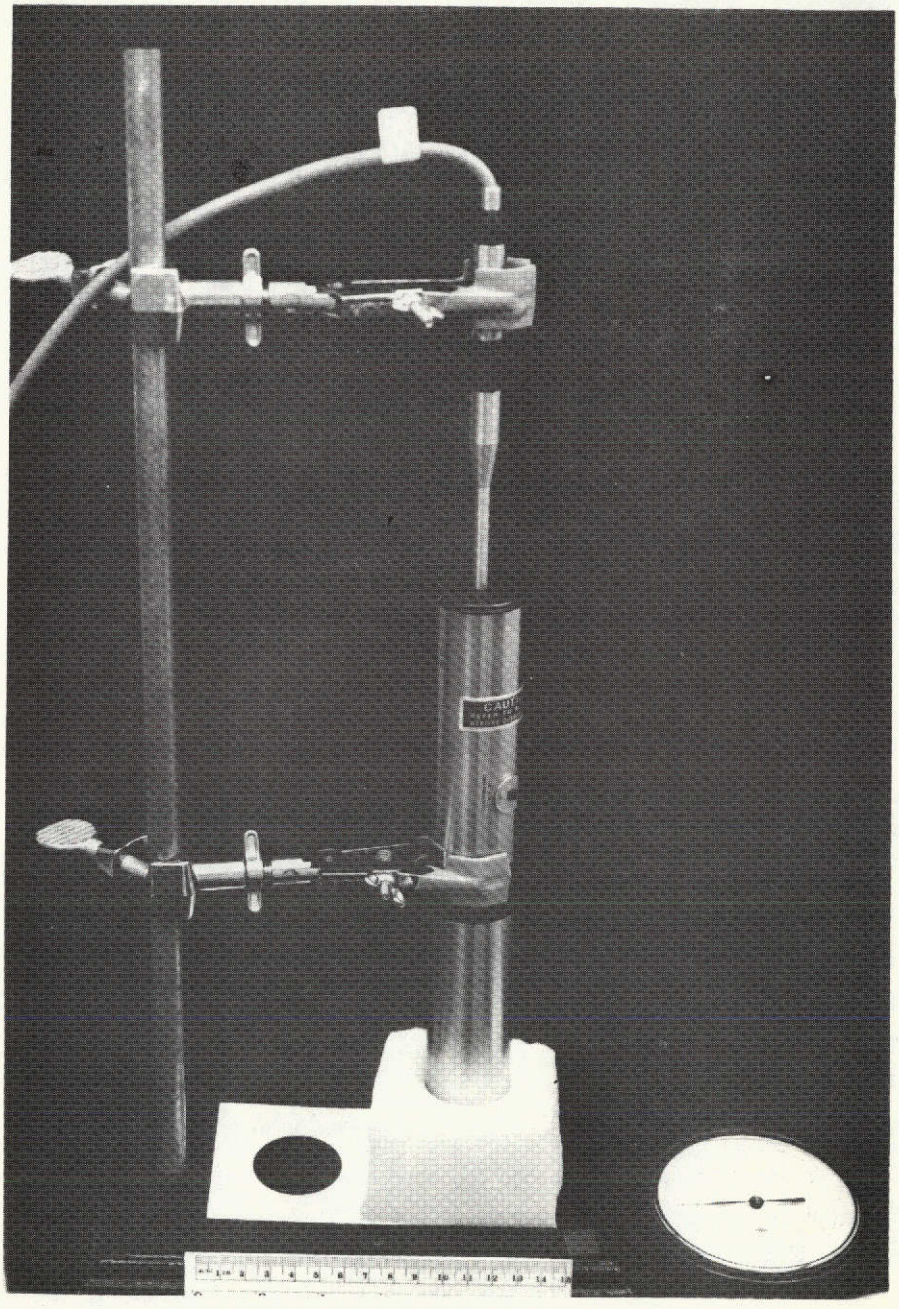

Figure 29. Photograph of the Microphone Calibration Equipment

predictions of the pressure profiles, and phase relationships of the pressure in various parts of the chamber, are compared to the experimentally determined ones.

To measure a radial pressure profile a B&K UA0040 probe microphone kit was used to make a 2 mm (0.079 in.) O.D., 22.86 cm (9.0 in.) long microphone probe which was attached to the B&K 4136/2615 microphone (microphone 3). A plexiglass adaptor was made for the central probe hole of the chamber to reduce the size of the hole to 2.36 mm (0.093 in.). The microphone probe was clamped into the manually adjusted probe holder (figure 21), which was mounted over the probe hole and used to position the tip of the probe at various radial locations in the chamber. The amplitude and the phase of the pressure was measured at each location. The phase measurement was accomplished by comparing the appropriate oscillator signal to the microphone signal, using a Acton 320-AB phase meter. The same microphone-probe adaptor combination was used in a similar fashion to investigate the longitudinal variation in the amplitude and phase of the pressure.

To examine the tangential variation in amplitude and phase, three additional microphones were used which were mounted in the same end plate as the acoustic drivers. These microphones are numbered as shown in figure 19. Microphone 1 is a B&K 4133 1.27 cm (0.50 in.) condenser microphone cartridge with a B&K 2615 cathode follower. It is powered by a B&K 2603 microphone amplifier. Microphone 2 is a B&K 4134 1.27 cm (0.50 in.) condenser microphone cartridge with a B&K 2615 cathode follower. It is powered by a B&K 2801 microphone power supply. Microphone 4 is a B&K 4135 0.635 cm (0.25 in.) condenser microphone cartridge

with a B&K 2615 cathode follower. It is powered by a B&K 2803 two-channel power supply. To determine the sound pressure level for any of these, they are connected to the B&K 2107 frequency analyzer. Each microphone is calibrated using the pistonphone. The three microphone power supplies can be seen in the photograph of figure 18.

When both the (100) and (202) acoustic fields exist in the chamber at the same time, each may be analyzed separately by using the frequency analysis mode of the B&K 2107 frequency analyzer. In this mode the particular frequency of interest is chosen by the setting of a frequency range dial and frequency tuning scale. Six different bandwidths are available.

Resonant frequency analysis. When the air in a chamber is excited by an acoustic driver, the resulting sound pressure level, for a fixed power input, depends on the frequency of the driver input. The sound pressure level peaks at the resonant frequencies of the chamber. This fact was used to perform the resonant frequency analysis mentioned at the beginning of the chapter.

The system shown in figure 30 was used to determine the resonant frequencies of the chamber. The acoustic driver is activated by the Wavetek function generator and the Altec power amplifier. The output frequency of the Wavetek is determined by the input voltage level to it. This voltage is supplies by a Hewlett-Packard 3310A function generator. The HP is set to deliver a very low frequency ramp function. The frequency used was about 2×10^{-4} Hz, which means one cycle would take almost an hour and a half to complete. In practice the total cycle was not used; the system was stopped when it was felt a sufficient range of frequencies had been examined. The amplitude was adjusted so

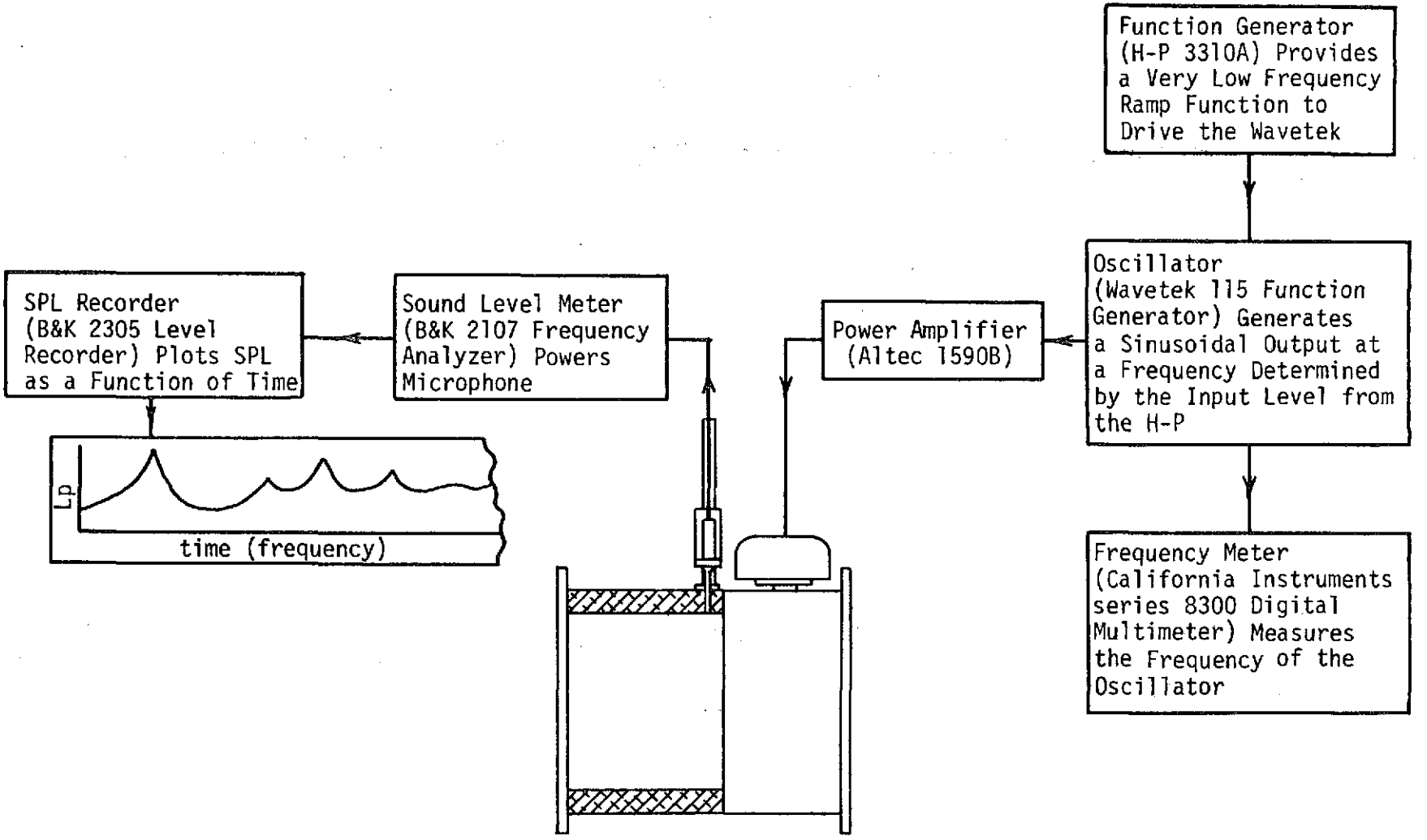

Figure 30. Schematic Diagram of the System used to Determine the Resonant Frequencies of the Chamber

that frequencies from about 100 Hz to greater than 4000 Hz were available. The frequency being produced by the Wavetek was measured by a California Instruments series 8300 digital multimeter. The HP function generator and multimeter can be seen in figure 26.

The microphone used to detect the sound pressure level is powered by the B&K 2107 frequency analyzer. The output from the 2107 is fed to a B&K 2305 level recorder, which plots the sound pressure level as a function of time. Since the frequency is dependent on time, the abscissa is also a measure of the frequency. To calibrate the abscissa, a mark was made on the chart at every 100 Hz interval, as indicated by the multimeter. The frequency varied linearly with time. The resonant frequencies are the frequencies at which the peaks occur on the chart. The level recorder is shown in figure 24.

Miscellaneous equipment. The power to the drivers, as well as the voltage and current, was monitored by a John Fluke 102 VAW meter. A switch was incorporated into the circuits of the drivers which enabled the VAW meter to be switched to either driver. The VAW meter is included in the photograph of figure 23.

An additional frequency meter was also used, a General Radio 1191-B counter. With it frequencies can be measured to within 0.1 Hz. It can be seen in figure 26.

To better understand the nature of the anemometer and microphone signals, spectrum analyses were performed on them. To do this an EMR-Schlumberger 1510 spectrum analyzer was used. A Houston Instruments Omnigraphic 2000 X-Y recorder was interconnected with the spectrum analyzer and was used to record the spectrum obtained. The analyzer and plotter are shown in figure 31.

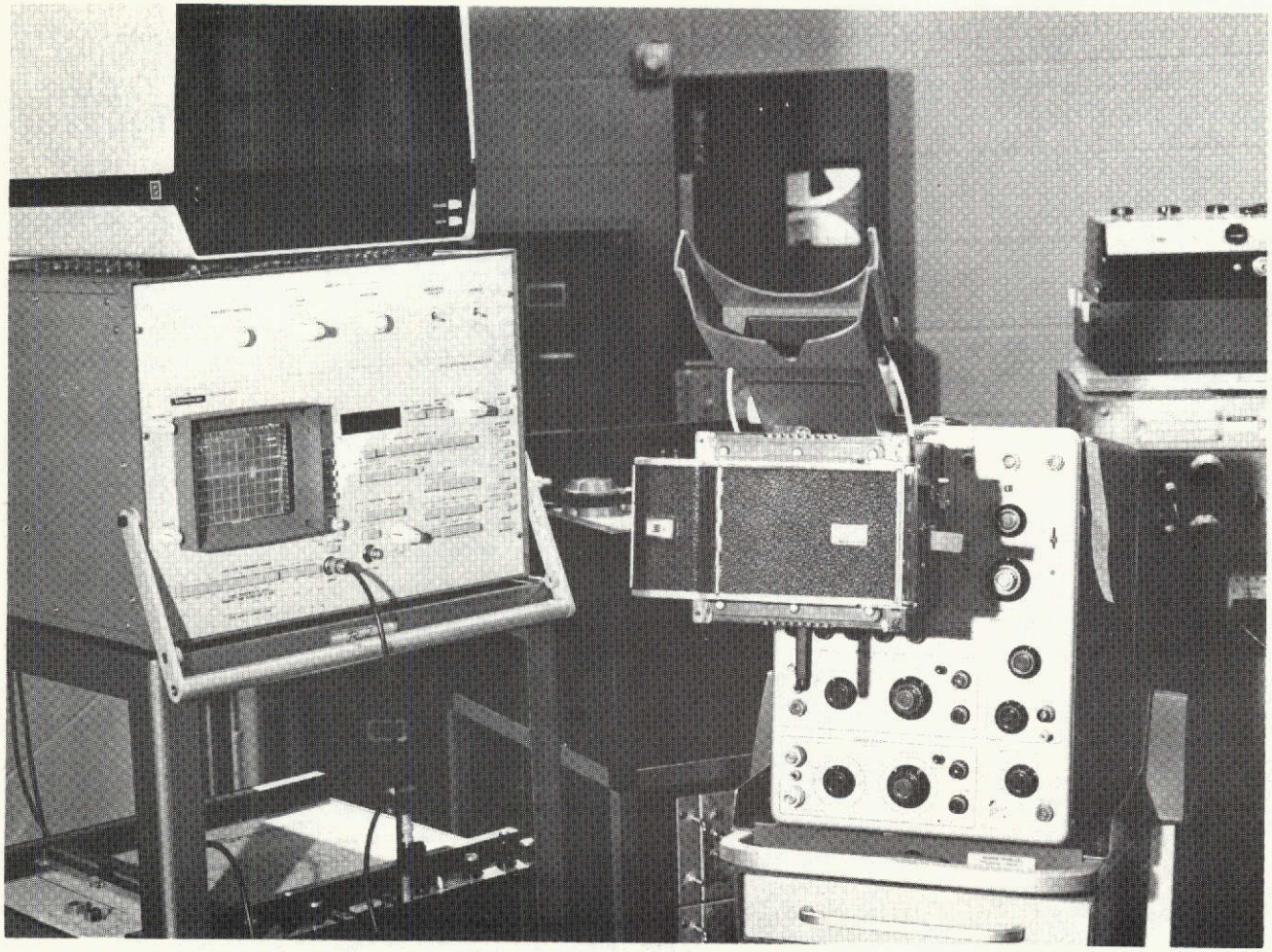

Figure 31. Photograph which shows the EMR-Schlumberger Spectrum Analyzer, Houston Instruments X-Y Recorder, Tektronix Oscilloscope and Polaroid Oscilloscope Camera

To study the phase relationships between the pressure and anemometer signals, and the shape of these signals, a Tektronix 502-A dual-beam oscilloscope was used. A Polaroid oscilloscope camera (Tektronix C-27) was mounted on the oscilloscope and pictures were made of the signals. The phase difference between the signals could then be determined from measurements of the distance between the peaks in the pictures. The oscilloscope and camera can be seen in figure 31. An additional oscilloscope was also used to monitor the wave shapes of the various signals -- a Hewlett-Packard 1200B dual-trace oscilloscope which can be seen in figure 26.

A Stabiline EM 10364 voltage regulator was used to supply regulated A.C. power to all of the electronic equipment.

When the system was in operation, it was found that the sound levels were too high for the personal safety or comfort of those operating the system, and were annoying to others working in the same building. Because of this, an acoustic shield was built which housed the test section itself. Most of the electronic equipment was kept on the outside of the shield. The shield is a structure 12-feet long, 8-feet wide and 8-feet high. The walls and roof are formed by a 2 x 4 framework covered with two layers of 3/8-inch sheetrock on the inside and two layers of 3/8-inch sheetrock on the outside. The roof is sealed to the top of the walls, and the bottom of the walls are sealed to the floor, with rubber weather stripping. The door is also sealed all around with rubber weather stripping. The inside is furnished with a fluorescent ceiling light and power receptacles. The cables connecting the chamber and the electronic equipment pass through a 2.5-inch

diameter hole in one of the walls. When in operation, the sounds being generated can still be heard outside the shield, but at a much reduced level. The acoustic shield is shown in figure 32.

An overall view of the electronic equipment is shown in figure 33.

PROCEDURES

All the electronic equipment was kept on at all times. Periodically, the various instruments were adjusted according to the manufacturers' instructions.

Six procedures will be described -- microphone calibration, chamber resonant frequency analysis, acoustic field generation and verification, hot-wire calibration and response factor determination.

Microphone Calibration

To calibrate a microphone the following procedure is used:

- The microphone is connected to its power supply and to the sound pressure level meter.
- The microphone is inserted into the pistonphone's cavity (using an adaptor is necessary).
- The pistonphone is turned on and the sound pressure level on the meter is determined. The pistonphone is turned off.
- The sound pressure level in the cavity is calculated by measuring the barometric pressure, determining the cavity correction factor from the barometer and adding this factor to 124.0 dB.
- The difference between the sound pressure level produced in the pistonphone cavity and the meter reading is determined. This difference is the microphone calibration factor; it

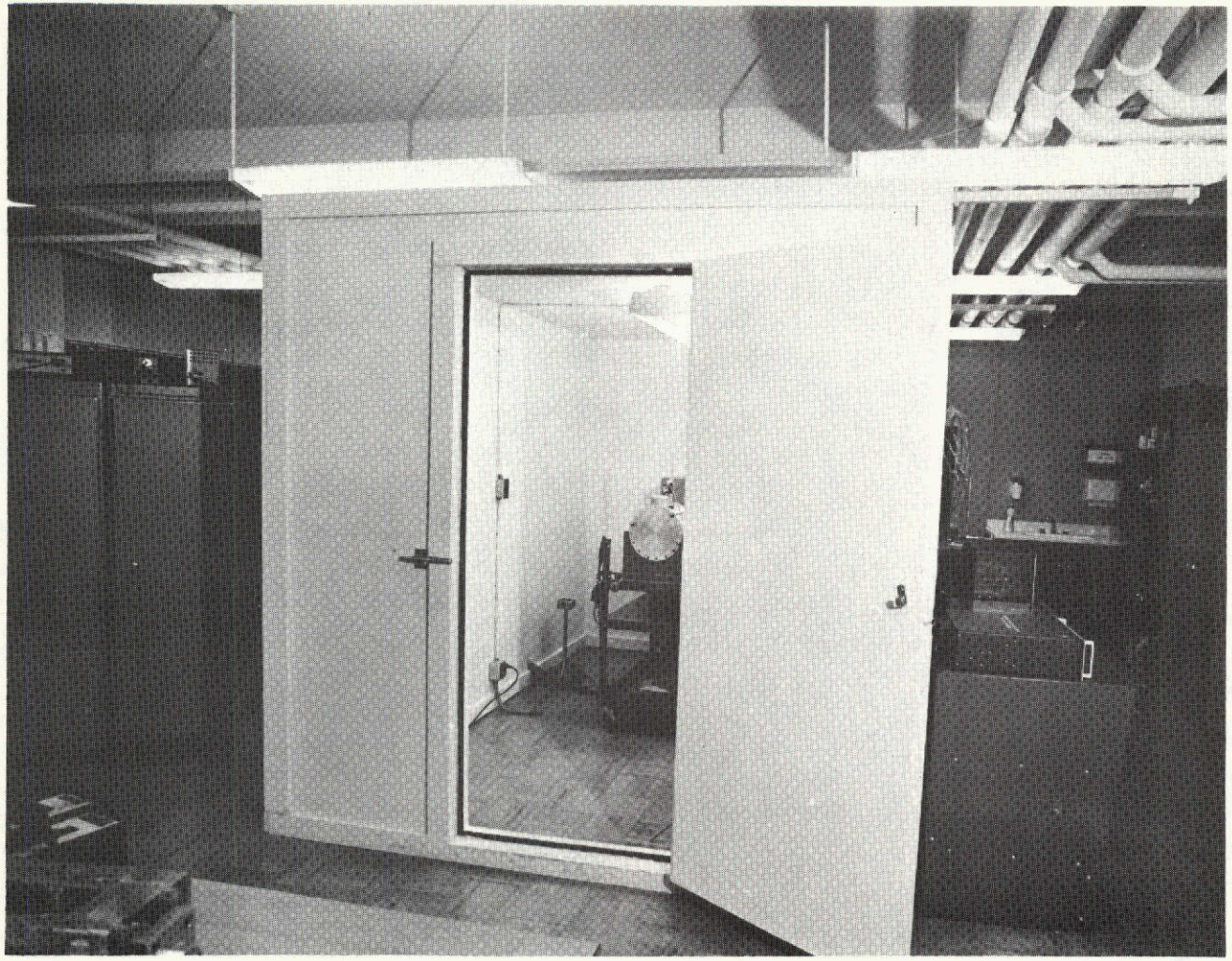

Figure 32. The Acoustic Shield

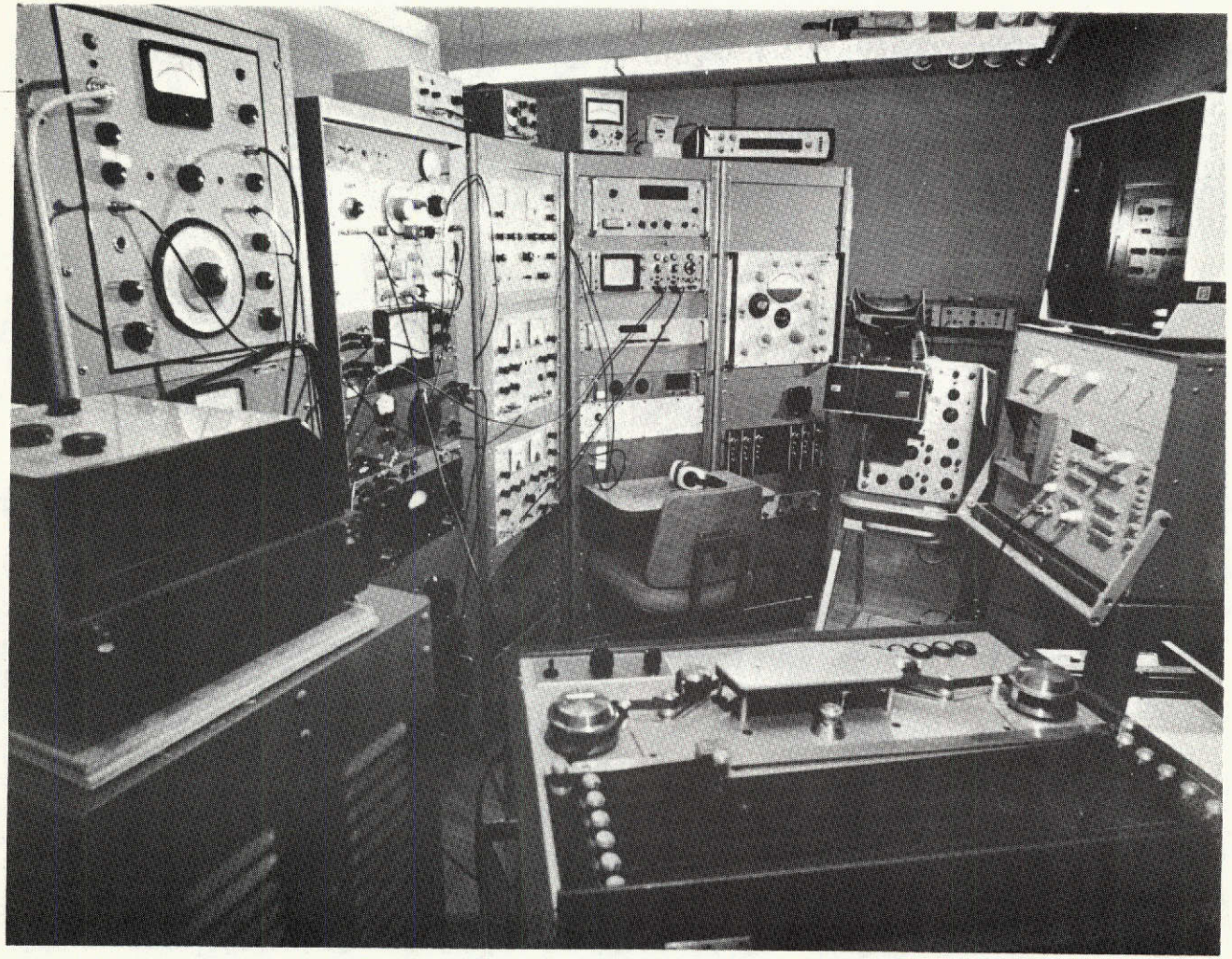

Figure 33. Overall View of the Electronic Equipment

must be added to the meter reading to obtain the true sound pressure level.

For the 2107 frequency analyzer the calibration factor depends on whether or not the instrument is being used in the frequency analysis mode. The microphones must be calibrated for both conditions.

The measured phase of a signal varies slightly depending on which microphone is used to detect it. Since the phase difference between various locations in the chamber is an important part of verifying that the correct acoustic field exists in the chamber, the microphones must be calibrated for phase relative to one another. This is done as follows:

- A standing resonant acoustic field is set up in the chamber.
- The microphone which is chosen as the "standard" is placed at a pressure antinodal position.
- The phase difference between the oscillator used to generate the acoustic field and the microphone is measured using the Acton phase meter.
- The "standard" microphone is removed and the other microphones are each successively placed at the same location and their phases are also measured.
- The difference between the "standard" phase measurement and each of the other microphones' phase measurement is then determined. The resulting numbers are the phase calibration factors for the microphones. This calibration must be done for each freqency used.

Chamber Resonant Frequency Analysis

To perform the chamber resonant frequency analysis, the system

is set up as shown in figure 29, with the exception that the HP and Wavetek function generators are not interconnected. The following procedure is then followed:

- The HP function generator is set for a ramp function output at a frequency of about 2×10^{-4} Hz and an amplitude of about 5 volts.
- The Wavetek function generator is scanned manually from about 500 Hz to about 3000 Hz to determine the maximum sound pressure level to be expected.
- The B&K recorder is scaled so the maximum sound pressure level will not go off scale and an appropriate paper speed is set -- about 0.3 mm/sec (0.71 in./min).
- When the HP function generator reaches the beginning of a cycle, it is connected to the Wavetek. This initiates the frequency scan.
- The B&K recorder is started.
- As each 100 Hz interval is reached, as indicated by the multimeter, the chart paper on the recorder is marked.
- When a sufficient range of frequencies has been scanned, the recorder is turned off and the HP is disconnected.
- The frequencies at which the peaks occur on the chart are measured. These are the resonant frequencies of the chamber.

Acoustic Field Generation and Verification

The desired acoustic field is a (100) spinning mode, distorted by a (202) spinning mode. These two modes are set up on the following basis:

- A spinning wave is the sum of two standing waves.
- The sound pressure level of a spinning mode, in a transverse section, at a particular value of r, is constant for any value of θ.
- For a (100) spinning mode the phase difference between the pressure at $\theta = \theta_1$ and the pressure at $\theta = \theta_2$ is equal to $(\theta_1 - \theta_2)$.
- For a (202) spinning mode, in a transverse section, the phase difference between the pressure at $\theta = \theta_1$ and the pressure at $\theta = \theta_2$ is equal to $2(\theta_1 - \theta_2)$.

To generate the acoustic field, the system shown schematically in figure 22 is used. The drivers and microphones are located as shown in figure 19. The microphones all have different power supplies, as was described previously, but they use the same B&K 2107 frequency analyzer for sound pressure level determinations. The frequency analysis mode is used to isolate the pressure associated with the (100) mode from that associated with the (202) mode. The microphones are calibrated for sound pressure level and phase. Prior to setting up the acoustic field, the inputs to the summers and the amplifiers are not connected. All other connections are as indicated in figure 22. The power amplifiers' controls are set at 8. The following is the procedure used to set up the acoustic field:

1. The amplitude adjust of the GR is turned up to an "appropriate" level. (An appropriate level depends on the sound pressure level desired. A sound pressure level of 155 dB or more would require close to the maximum

output. A sound pressure level of 140 dB would only require about a third of that.)

2. The GR output is connected to amplifier and summer 1 (AS1). The output of AS1 is connected to power amplifier 1 (PA1). This sets up a standing acoustic field in the chamber.
3. Microphone 1 (M1) is connected to the B&K 2107 and the frequency of the GR oscillator is tuned to the (100) resonant frequency. This frequency varies slightly with the temperature, but it is approximately 990 Hz. Tuning is accomplished by varying the frequency from 990 Hz until the maximum sound pressure level is obtained.
4. The B&K 2107 is turned to the frequency analysis mode and set to the (100) frequency.
5. The sound pressure level is adjusted to the approximate level desired for the (100) mode by use of the appropriate potentiometer of AS1.
6. The input to PA1 is disconnected. The phase shifted GR signal is connected to AS2 and the input to PA2 is connected.
7. M2 is connected to the B&K 2107 and the sound pressure level is adjusted to the approximate (100) level desired, by use of the appropriate potentiometer of AS2.
8. The input to PA1 is reconnected. Two standing waves of approximately the same amplitude now exist in the chamber. Next, the proper phase relationship between the two must be established.
9. M1 is connected to the B&K 2107. The exact (100) sound pressure level desired is set by adjusting the appropriate

potentiometer of AS1. The phase between the output of the GR and M1 is determined using the Acton phase meter.

10. M2 is connected to the B&K 2107. The phase between the GR and M2 is measured using the phase meter. The Lyrec phase shifter is adjusted until the difference in the phases measured in steps 9 and 10 is 135 degrees. The exact (100) sound pressure level desired is set by adjusting the appropriate potentiometer of AS2.
11. Steps 9 and 10 are repeated until the sound pressure levels of M1 and M2 are the same and the signals are 135 degrees out of phase. A (100) spinning acoustic mode should now exist in the chamber. Next, the (202) spinning mode is set up.
12. The amplitude adjust of the Wavetek is turned up to an appropriate level.
13. The Wavetek output is connected to AS1. This sets up a standing (202) acoustic field in the chamber. It is at resonance because the Wavetek frequency is twice the GR frequency and the (202) resonant frequency is twice the (100) resonant frequency. Tuning for the (100) mode tunes for the (202) mode.
14. The B&K 2107 is set to the (202) frequency. (It is still in the frequency analysis mode.)
15. The sound pressure level is adjusted to the approximate level desired for the (202) mode by use of the appropriate potentiometer of AS1.
16. The phase shifted Wavetek signal is connected to AS2.

17. M2 is connected to the B&K 2107 and the sound pressure level is adjusted to the approximate level desired for the (202) mode by use of the appropriate potentiometer of AS2.
18. M1 is connected to the B&K 2107. The exact (202) mode sound pressure level desired is set by adjusting the appropriate potentiometer of AS1. The phase between the output of the Wavetek and M1 is determined using the phase meter.
19. M2 is connected to the B&K 2107. The phase between the Wavetek and M2 is measured. The Acton phase shifter is adjusted until the difference in the phases measured in steps 18 and 19 is 270 degrees. The exact (202) mode sound pressure level desired is set by adjusting the appropriate potentiometer of AS2.
20. Steps 18 and 19 are repeated until the sound pressure levels of M1 and M2 are the same and they are 270 degrees out of phase. A (202) spinning acoustic mode should now exist in the chamber along with the (100) spinning acoustic mode.
21. Minor adjustments in the levels of the two modes can be made using the GR and Wavetek amplitude adjustment potentiometers.
22. The phase for the (202) mode with respect to the (100) mode can be changed by varying the phase adjustment knob of the Wavetek.

Before proceeding to studies of the response factors using this method to set up the acoustic field, more extensive investigations were

performed to verify that the desired acoustic field had been set up. The variation in the level and phase of the sound pressure with respect to θ, r and z is predicted by equation (A.48a). Measurements were made of the sound field to see if it matched the theory.

When setting up the sound field for verification purposes, two additional steps are added to the procedure:

11a. M4 is connected to the B&K 2107 and the sound pressure level and phase between the Gr and M4 is measured.

20a. M4 is connected to the B&K 2107 and the sound pressure level and phase between the Wavetek and M4 is measured.

These two steps are an additional check on the variation of sound pressure level and phase with respect to θ.

The procedure for checking the variation in level and phase with respect to r consists of the following steps:

1. Microphone 3 in combination with the probe tube extension is positioned over the central probe access hole using the manually adjusted probe holding and positioning device. M3 is connected to the B&K 2107 frequency analyzer.
2. The sound field is set up in the chamber using the method described previously.
3. With the B&K 2107 in the frequency analysis mode and set to the (100) frequency, values of the sound pressure level and the phase with respect to the GR function generator are measured at various radial locations in the chamber.
4. With the B&K 2107 in the frequency analysis mode and set to the (202) frequency, values of the sound pressure level and the phase with respect to the Wavetek function generator

are measured at various radial locations in the chamber.

The procedure for checking the variations in level and phase with respect to z is the same as that with respect to r, except that the microphone probe and holder are mounted on an end plate.

Hot Wire Calibration

The wire calibration is divided into two parts -- data taking and data analysis.

Data taking. The following is the procedure used for taking the data from which to calibrate a hot wire:

1. The calibration equipment is set up as shown in figure 28. The variable transformer is turned to the off position. The hot wire is mounted in the wind tunnel in the orientation that will be used in the experimental system.
2. The operating temperature of the hot wire is chosen and the wire operating resistance associated with this is set on the anemometer. The anemometer is turned to "operate."
3. The micromanometer is set to zero.
4. An appropriate amount of amplification is set on the Neff amplifier.
5. The barometric pressure and ambient temperature are measured.
6. The switch is set to "E." The timer and the HP integrating voltmeter are reset to zero. The timer is turned on, which starts the integration. After a minimum elapse time of 100 seconds, the timer is turned off, which stops

the integration, and the resulting values of $\int_0^T E\,dt$ and T are recorded.

7. The switch is set to "H." The timer and the voltmeter are reset to zero. The timer is turned on, which starts the integration. After a minimum elapse time of 100 seconds the timer is turned off, which stops the integration, and the resulting values of $\int_0^T H\,dt$ and T are recorded.
8. The setting on the variable transformer is increased. This places a flow across the wire. Steps 6 and 7 are repeated.
9. Step 8 is repeated until a sufficiently high flow rate has been established so that readings of the pressure drop across the nozzle can be read on the Meriam micromanometer; a micromanometer reading of ΔP is taken after steps 6 and 7 are completed. Care must be taken that sufficient time elapses between increasing the flow rate and the taking of the data so that the system has had time to reach steady state.
10. When a sufficiently high velocity has been reached, the system is shut down and the data are analyzed.

Data analysis. The hot wire calibration equation is

$$E = [A + B\,V^N]^{0.5} \tag{2.18}$$

What follows is the procedure used to fit the data to an equation of this form; the constants A, B and N are to be determined:

1. Each value of $\int_0^T E\,dt$ and $\int_0^T H\,dt$ is divided by the value of T associated with it. This determines time-average value of E and H for each flow rate.

2. The H data, which are in volts, must be converted to equivalent pressures. This is accomplished by performing a least-squares curve fit of the H versus ΔP data; the relationship is linear. When the equation is obtained, the values of H are converted to ΔP.
3. The velocity $\bar{V}$ which corresponds to each value of ΔP is found using the following equation:

$$V^2 = \left[\frac{2\gamma}{\gamma-1}\right] R_a T[1 - (1 - \Delta P/P)^{(\gamma-1/\gamma)}] \tag{3.13}$$

This equation is taken from the instruction manual for the calibrating wind tunnel [20].

4. Equation (2.18) can be put in the form

$$\ln (E^2 - A) = \ln B + N \ln V \tag{3.14}$$

Letting

$$\ln (E^2 - A) = Y \tag{3.15a}$$

$$\ln B = b \tag{3.15b}$$

and

$$\ln V = X \tag{3.15c}$$

equation (3.14) becomes

$$Y = b + NX \tag{3.16}$$

A value is assumed for A. Using this assumed value, the data are converted to Y and X and a computer program is used to fit the resulting values to equation (2.18). The program

determines a value for b and N and also a value for the "goodness-of-fit" of the equation to the data.

5. Other values of A are assumed and the procedure in step 4 is repeated for each.
6. A plot of the goodness-of-fit versus the assumed value of A is made. The value of A where the goodness-of-fit reaches a maximum is determined. This value of A, along with the corresponding values of b and N, determine the wire calibration equation constants A, B and N.

By knowing the temperature difference at which the calibration was performed, together with various other wire and flow field characteristics, equation (2.17) can be obtained from equation (2.18). Equation (2.17) is then used for the analysis done in Chapter 2. A more detailed discussion of the hot-wire calibration procedure can be found in reference [20].

Response Factors

To obtain the data necessary to calculate response factors, the experimental system shown schematically in figure 17 was used.

Both the hot-wire and microphone probes should be at the same location. Since this is impossible, some compromise had to be made. Also, the interference of the probes with the sound field should be kept at a minimum.

The rate of change of P'_{rms} with respect to radial position decreases as r increases and approaches zero as r approaches R. Because of this, and to prevent the microphone from affecting the sound field, the microphone used to obtain the response factors (B&K 4136, microphone

3) was mounted flush with the inside surface of the test section. (As was discussed previously, the longitudinal location of the probes, $z = L/2$, was determined by the characteristics of the (202) acoustic field.)

The hot wire was positioned directly under the microphone at $r/R = 0.875$ and was oriented vertically (coincident with the radius vector to the microphone).

The quantity $\phi_2 - \phi_1$ is the phase difference between the fundamental and distortion component of the acoustic oscillations using the terminology Heidmann developed. The relationship between this terminology and that which was used in the solution of the inviscid wave equation was explained in Chapter 2. The phase difference can be measured using any arbitrary reference point; therefore, ϕ_1 will be assumed to be zero and, henceforth, the phase difference $\phi_2 - \phi_1$ will be equal to ϕ_2.

Two procedures were used to obtain response factors. The first procedure generated the variation in $R_{n\ell}$ with respect to $\tilde{P}'_{rms}$, for ϕ_2 equal to zero and 180 degrees and for a constant value of p_2/p_1. The second procedure generated the variation in $R_{n\ell}$ with respect to ϕ_2 when $\tilde{P}'_{rms}$ and p_2/p_1 are held constant.

$R_{n\ell}$ as a function of P'_{rms}. With the system set up as illustrated in figure 17, the procedure to determine $R_{n\ell}$ as a function of $\tilde{P}'_{rms}$ is as follows:

1. A value of p_2/p_1 is chosen. From this the corresponding difference between the sound pressure levels ($Lp_{100} - Lp_{202}$) is determined.

2. All the microphones are calibrated.
3. The atmospheric pressure and temperature are recorded.
4. The anemometer is switched from its stand-by to its operating condition.
5. The signal from the Wavetek is taken from the positive sinusoidal output. The Wavetek's phase shift knob is set at its minimum position (counter clockwise). At this setting it is least likely to become unlocked while manipulations are being made to set up the acoustic field.
6. With the B&K 2107 frequency analyzer in the frequency analysis mode and using microphones 1 and 2, an acoustic field is set up which has approximately the required value of (Lp_{100} - Lp_{202}) and which has the maximum overall sound pressure level obtainable without overheating the drivers (the power to the drivers is limited to less than 10 watts).
7. Using microphone 3 (with the B&K 2107 still in the frequency analysis mode) and the external amplitude adjustment potentiometers of the GR and Wavetek function generators, the sound pressure levels are adjusted to the exact value of (Lp_{100} - Lp_{202}) desired.
8. With the B&K 2107 no longer in the frequency analysis mode (all frequencies now included in the microphone signal) the phase shift of the Wavetek is adjusted until the trace of the pressure signal, as seen on an oscilloscope, has "even peaks" (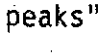). This is the waveshape predicted when

ϕ_2 is equal to zero degrees.[1]

9. The value of $(Lp_{100} - Lp_{202})$ is rechecked.
10. The overall sound pressure level is read from the meter on the B&K 2107.
11. The timer-integrating voltmeter combination is started.
12. The value of E'_{rms} is read from the TSI rms voltmeter.
13. The necessary adjustments are made to the correlator controls and the value of R is read from its meter and recorded.
14. The timer-integrating voltmeter system is stopped and the resulting values of $\int_0^T E\,dt$ and T are recorded. Sufficient information has now been obtained to determine a value of $R_{n\ell}$.
15. The Tektronix 502A oscilloscope and camera are used to make a photographic record of the microphone and anemometer signals.
16. The EMR-Shlumberger spectrum analyzer is used to obtain the frequency spectrum of the microphone and anemometer signals. A permanent record is made of these spectrum analyses using the Texas Instruments X-Y plotter. (It is not necessary to carry out steps 15 and 16 every time since they are not necessary to determine the value of $R_{n\ell}$.

---

[1]No method was available to measure the absolute difference in phase ϕ_2 between the (100) and (202) acoustic fields; only the change in phase could be measured. Hence, the even peaks condition associated with $\phi_2 = 0$ was used as a reference, and other phase angles were determined by adding or subtracting, whichever was appropriate, the change in ϕ_2 to it. The method used to measure the change in ϕ_2 is described in the procedural description following this one.

17. The output from the Wavetek is changed from the positive to the negative sine and the phase adjustment knob is used to set up "even peaks" again. The peaks are now on the bottom instead of on the top ( ), which corresponds to ϕ_2 = 180 degrees.
18. Step 7 is repeated.
19. Steps 10 through 14, 15 or 16 are repeated.
20. Steps 5 through 19 are repeated, but at a lower overall sound pressure level.
21. Step 20 is continually repeated until the overall sound pressure level is so low that meaningful measurements can no longer be made.

$R_{n\ell}$ as a function of ϕ_2. The procedure used to obtain $R_{n\ell}$ as a function of ϕ_2 is as follows:

1. With the system set up as illustrated in figure 17, steps 1 through 7 of the previous procedure are followed with the exception that the overall sound pressure level is not necessarily set to the maximum obtainable. Usually it is more desirable to use the sound pressure level which corresponds to the maximum value of $R_{n\ell}$ as determined by previous data or analysis.
2. The phase angle between the outputs of the GR and Wavetek function generators is measured using the Acton phase meter. This establishes a relative phase difference between the (100) and (202) acoustic fields. It is not an absolute phase difference since the phase changes that occur between

the function generators and the actual sound fields is not known.

3. Steps 10 through 14, 15 or 16 of the previous procedure are followed.
4. The relative phase between the GR and Wavetek function generators is changed by a few degrees using the phase adjustment knob of the Wavetek. The new relative phase difference is measured using the Acton phase meter. The change in phase is the difference between the previous phase measurement and this measurement.
5. Steps 3 and 4 are repeated until the Wavetek is no longer able to remain locked to the GR. During this step the phase angle reading at which the even peaks condition occurs is recorded.
6. The phase adjustment knob of the Wavetek is returned to its counterclockwise position, the output of the Wavetek is changed from the positive to the negative sine and the frequency and phase lock condition of the Wavetek is reestablished.
7. Steps 2 through 5 are repeated.

When these two procedures have been completed, the response factors are calculated from the data generated using equation (3.8)

$$R_{n\ell} = R \left[\frac{E'_{rms}}{P'_{rms}} \right] \left[\frac{\bar{P}}{\bar{E}} \right] \qquad (3.8)$$

RESULTS AND DISCUSSION

The results of a hot-wire calibration and the sound field verification procedures are presented and discussed. Data were taken to determine the microphones' and anemometer's operational characteristics; certain of these characteristics are depicted. Finally, the response factors themselves are presented.

The results of the chamber resonant frequency analysis have already been presented in the introduction of this chapter.

Hot-Wire Calibration

Two hot wires were calibrated during the course of the research. The resulting calibration equations are similar. Figure 34 contains the data used to determine a calibration equation and the equation itself. For this case the calibration constants of equation (2.18) are:

$$A = 11.909$$

$$B = 8.0995$$

$$N = 0.444$$

with a goodness-of-fit of 0.99988. Combining these values with the various wire and flow field properties, the constants of the anemometer equation, equation (2.17), are found to be

$$\hat{A} = 0.525$$

$$\hat{B} = 0.6729$$

The equations and data used to obtain $\hat{A}$ and $\hat{B}$ are contained in Appendix C. These constants were used in the analytical portion of the research.

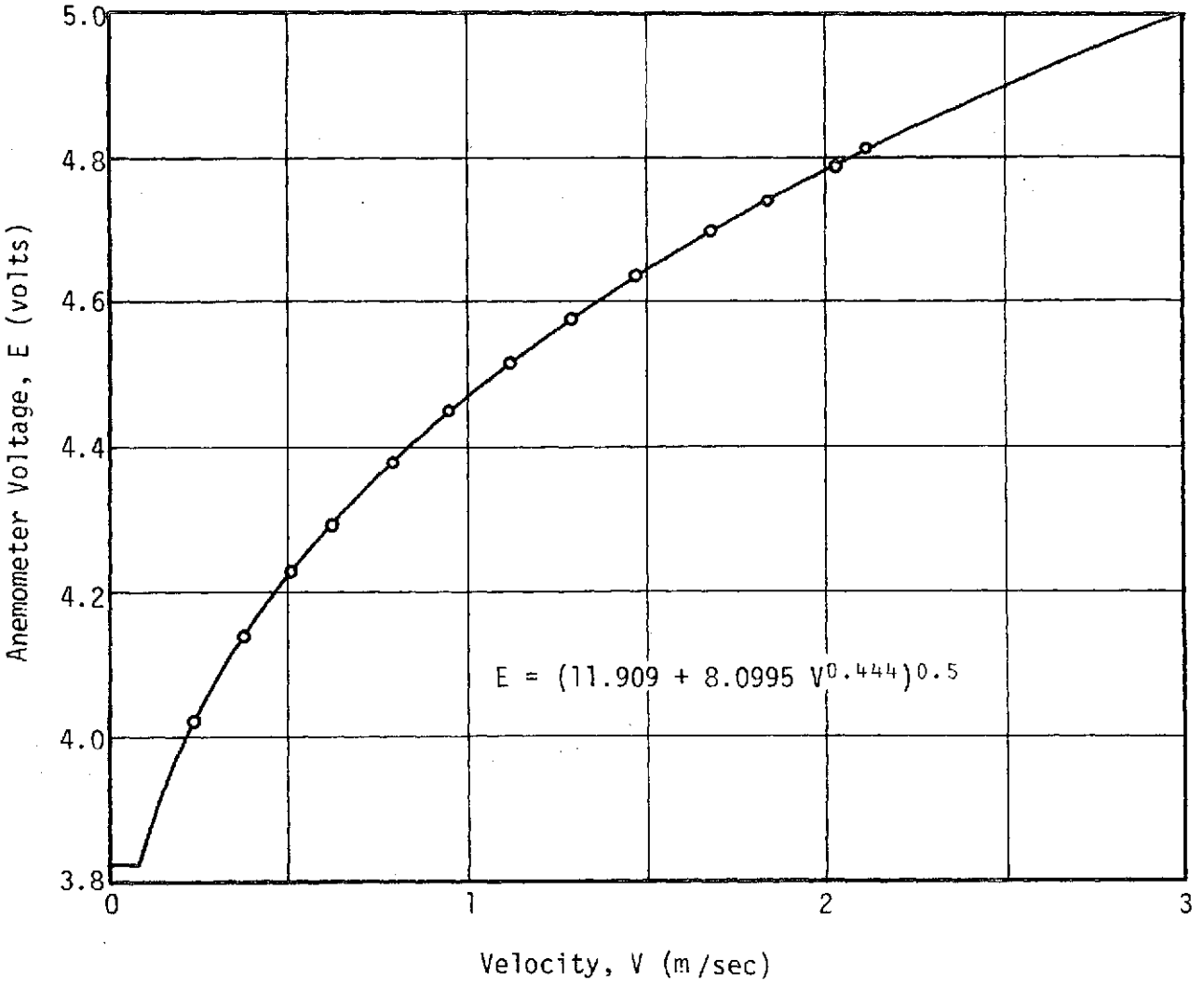

Figure 34. Hot-Wire Calibration Data and Resulting Equation

The anemometer equations were developed assuming forced convection heat transfer from the hot wire to the surrounding cooler air. At a velocity of zero, or very close to zero, free convection heat transfer dominates and the equations are not valid. Because of this, the anemometer output at zero velocity is not a valid data point for obtaining the wire calibration constants and, therefore, it is not used in the least-squares curve fitting procedure.

To account for the change in heat transfer mode in the vicinity of zero velocity, the calibration equation is considered to consist of two regions -- a very short free convection dominated region in which the anemometer output E is assumed to remain constant at its zero velocity value and a forced convection dominated region in which the equation for E is that determined by the calibration procedure described. The boundary of these two regions is the intersection of the constant E region and the variable E region. These two regions are shown in figure 34.

Sound Field Verification

Verification of the sound field depends on comparison of the analytically predicted sound pressure in the chamber with that obtained experimentally. The expected analytical distributions were discussed in Chapter 1.

Figure 35 shows the variation in the normalized values of P'_{rms} across a diameter of the chamber, at the central cross section, for the (100) mode. Information regarding the phase of the pressure along the diameter with respect to the pressure at r = R is also shown in this figure. Figure 36 is similar to figure 35, but it is for the (202) mode.

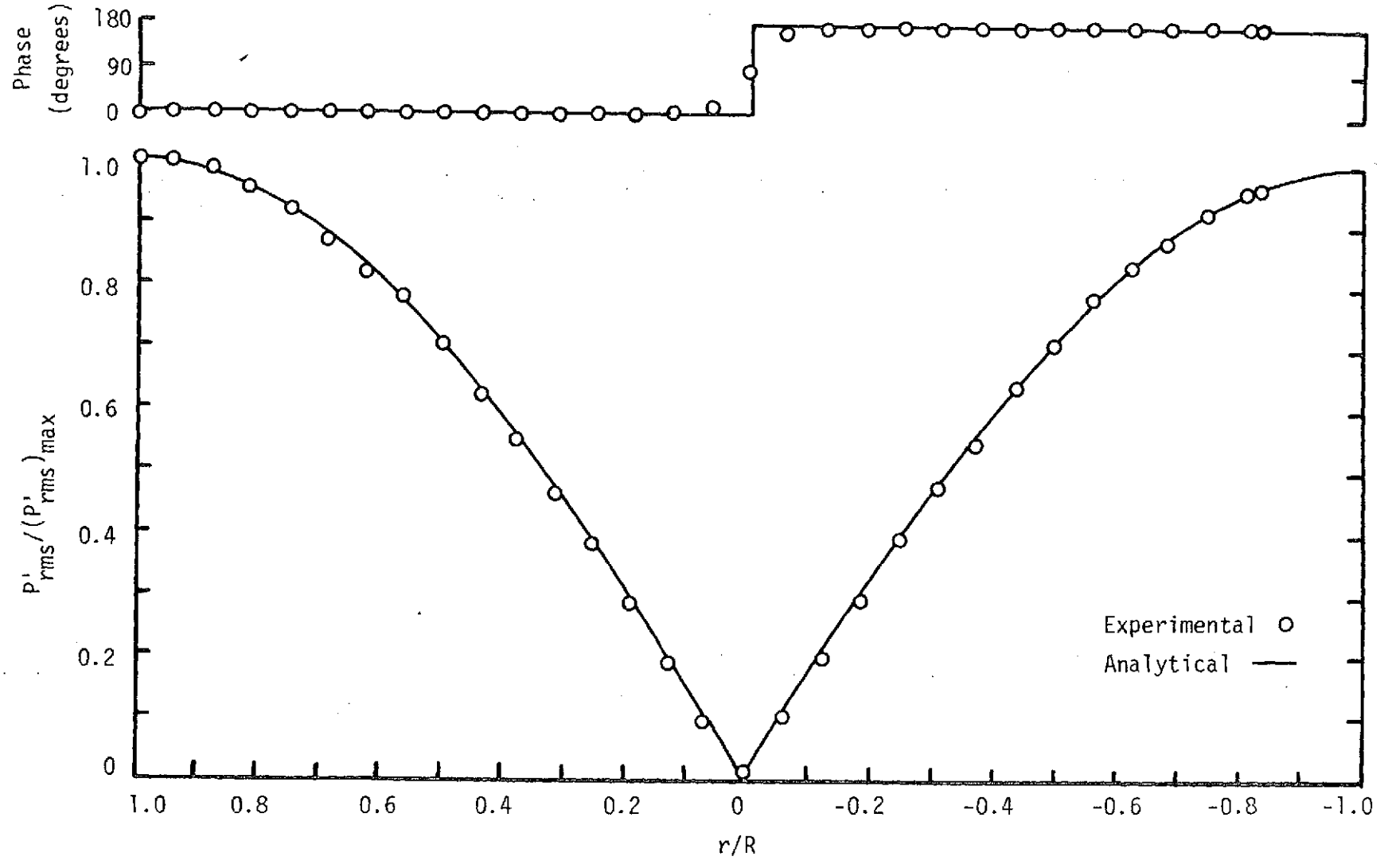

Figure 35. Sound Pressure and Phase Variation of the First Tangential Mode Along a Diameter

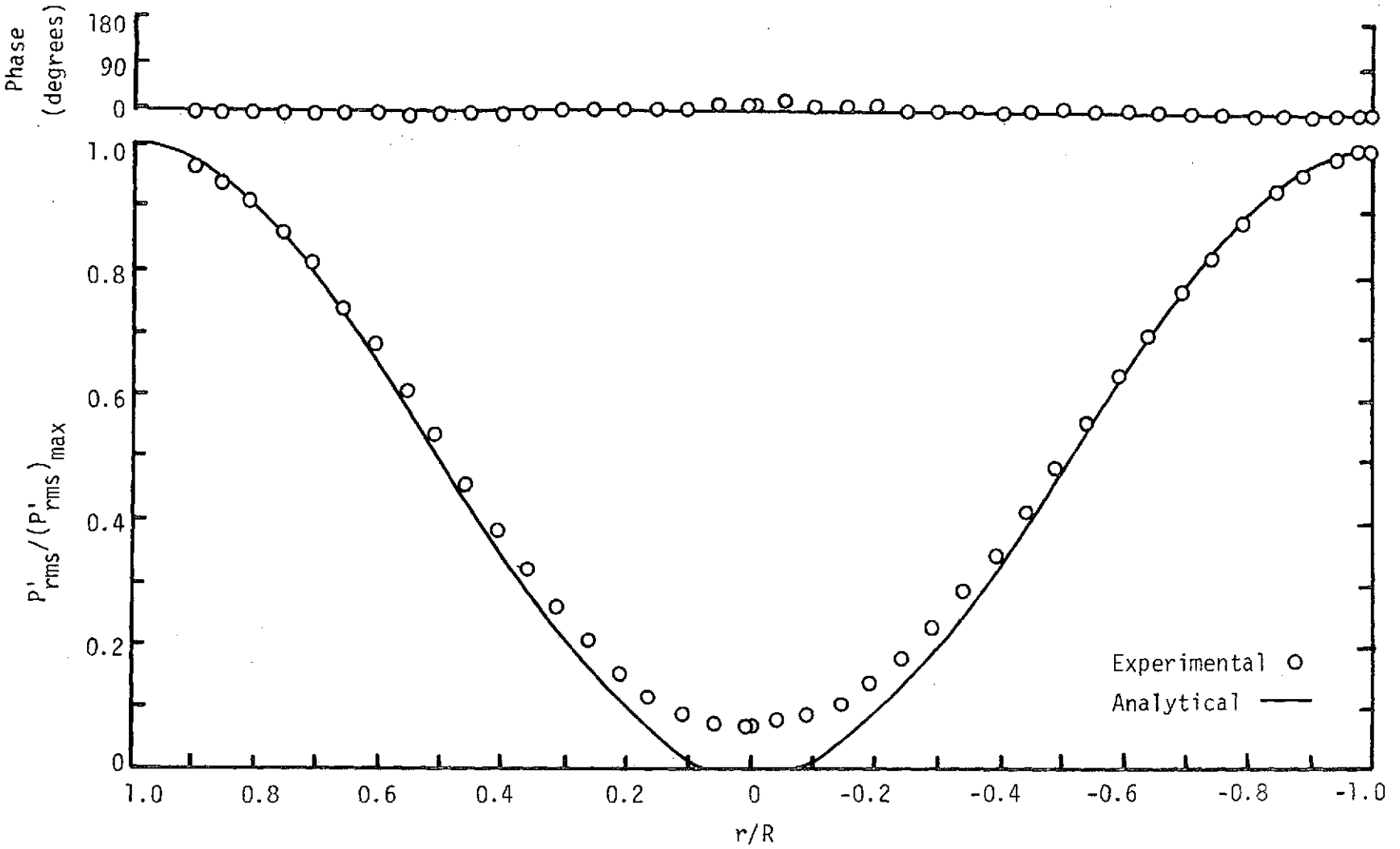

Figure 36. Sound Pressure and Phase Variation of the Second Tangential - Second Longitudinal Mode Along a Diameter at the Central Cross Section of the Chamber

Figure 37 shows the variation in the normalized value of P'_{rms} and phase with respect to longitudinal position, at r/R = 0.90, for the (202) mode. The same data were taken for the (100) mode; however, no variation in either pressure of phase is predicted for the (100) mode and the data indicated only a slight decrease in P'_{rms} near the end plate.

For the spinning situation, there should be no tangential variation of pressure amplitude for a constant value of r. The difference in the values of sound pressure level of the (100) mode, as measured by the three microphones mounted in one of the end plates, varied from 0.2 dB to 0.7 dB. The difference in the values of sound pressure level of the (202) mode, as measured by the three microphones in the end plate, varied from 0.3 dB to 1.3 dB.

The above errors in the sound pressure level are related to the errors in the value of the phase angle measurements between the microphones. As was explained earlier, for a (100) spinning mode, the phase difference between the pressure at $\theta = \theta_1$ and the pressure at $\theta = \theta_2$ is equal to $(\theta_1 - \theta_2)$. The error associated with the phase measurements between the three microphones in the end plate for the (100) mode, ranged from 2 to 8 degrees. For a (202) spinning mode, the phase difference between the pressure at $\theta = \theta_1$ and the pressure at $\theta = \theta_2$ is equal to $2(\theta_1 - \theta_2)$. The error associated with the phase measurements between the three microphones in the end plate, for the (202) mode, ranged from 1 to 8 degrees.

The larger errors in the sound pressure levels are associated with the smaller errors in the phase measurements, and vice versa. The errors are in part caused by the dimensions and locations of the microphones. Microphones 1 and 2 have a 1.27 cm (0.50 in.) diameter

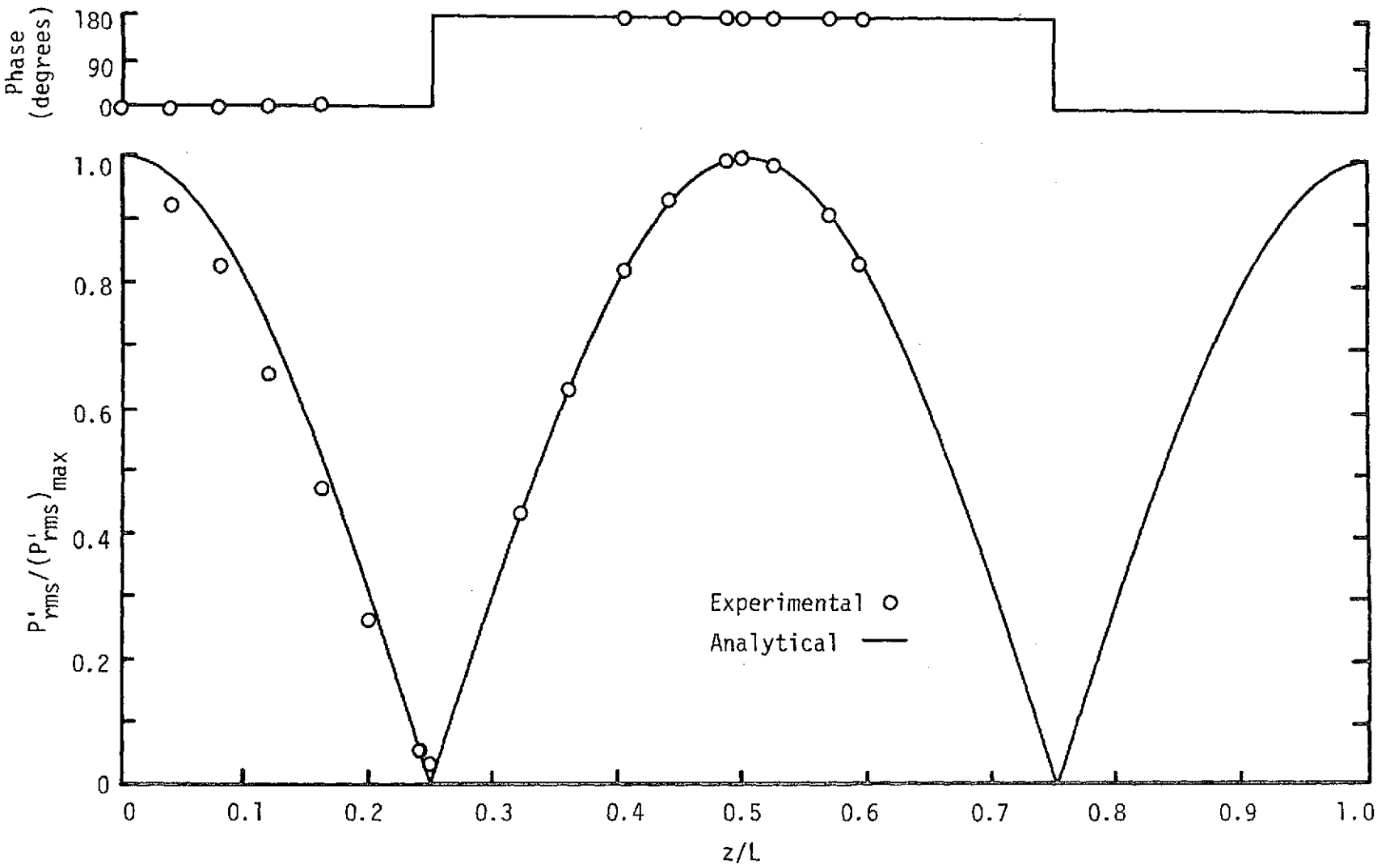

Figure 37. Sound Pressure and Phase Variation of the Second Tangential - Second Longitudinal Mode with Respect to Longitudinal Position at r/R = 0.90.

and are mounted so their circumference is tangent to the circumference of the cylinder. The third microphone, microphone 4, has a 0.635 cm (0.25 in.) diameter and is mounted so its circumference is 0.317 cm (0.125 in.) from the circumference of the cylinder. The measurements are being made over a finite area, not a point. In addition, the acoustic field is being driven by drivers that each act over a finite circular area, 1.91 cm (0.75 in.) in diameter, not a point.

Microphone and Anemometer Operational Characteristics

Figure 38 is a plot of the analytical and experimental values of time-mean anemometer output voltage $\overline{E}$ with respect to $\tilde{P}'_{rms}$, for various values of p_2/p_1. The experimental values of $\overline{E}$ are similar to those predicted analytically.

Figure 39 is a plot of the analytical and experimental values of the root-mean-square of the time-dependent anemometer output voltage E'_{rms} with respect to $\tilde{P}'_{rms}$ for various values of p_2/p_1. The analytical and experimental values are not similar.

Figures 40, 41, 42 and 43 illustrate the analytical and experimental microphone and anemometer waveforms for the (100), the (202) and the combined (100) plus (202) spinning modes. The waveform for the combined mode depends on the phase relation ϕ_2. The waveforms for ϕ_2 equal to zero and 180 degrees are shown. There are differences between the analytically predicted and experimentally obtained wave forms. The locations of the anemometer peaks with respect to the microphone peaks are not the same analytically and experimentally -- a phase shift exists. The relative amplitudes are also different.

Figures 44, 45 and 46 are frequency spectrum analyses of the

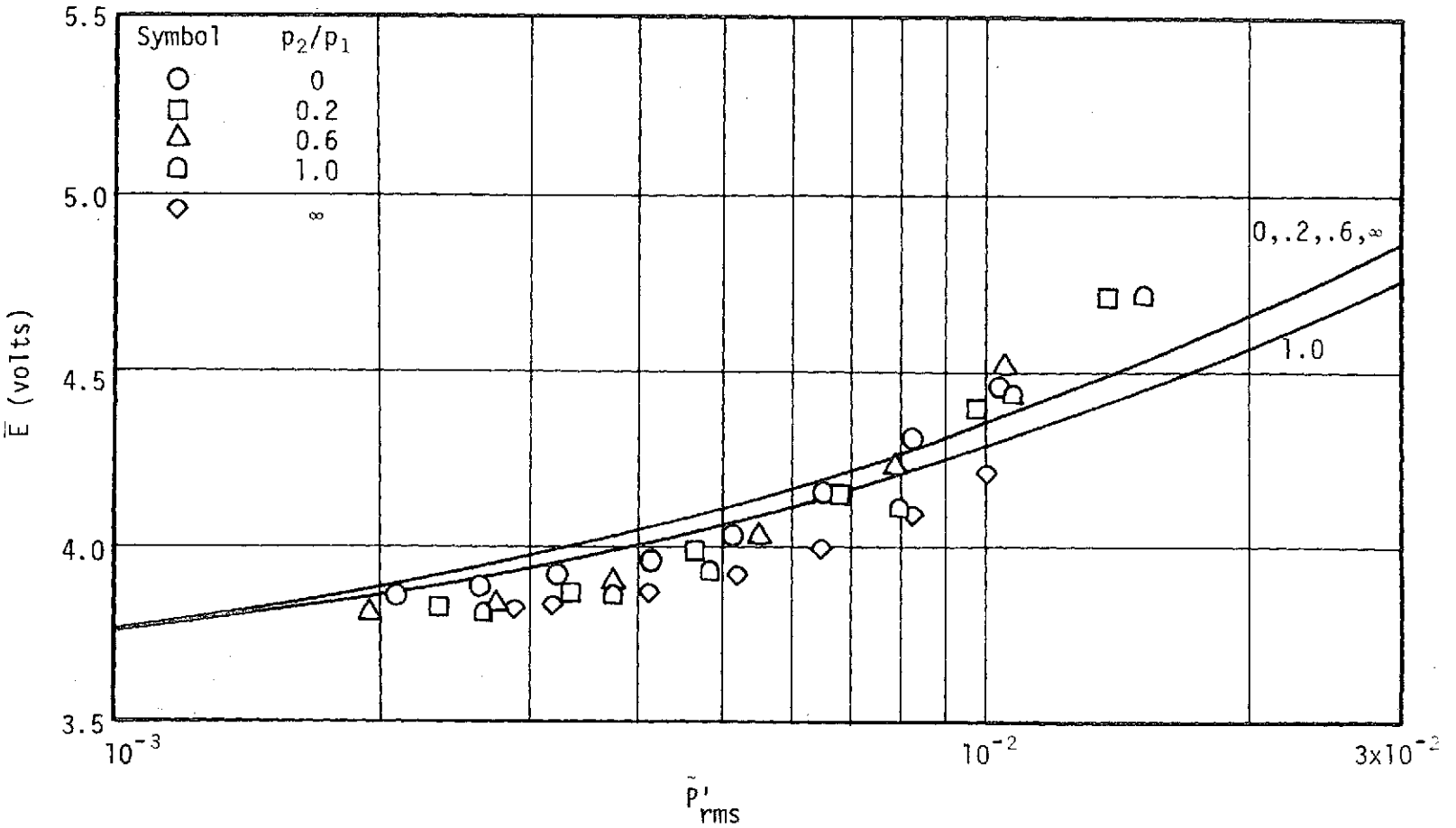

Figure 38. Analytical and Experimental Values of $\bar{E}$ Versus $\tilde{P}'_{rms}$ for Various Ratios of p_2/p_1; M = 0, $\phi_1 = \phi_2 = \theta_1 = \theta_2 = 0$, $T_w - T_\infty$ = 111.0 K°

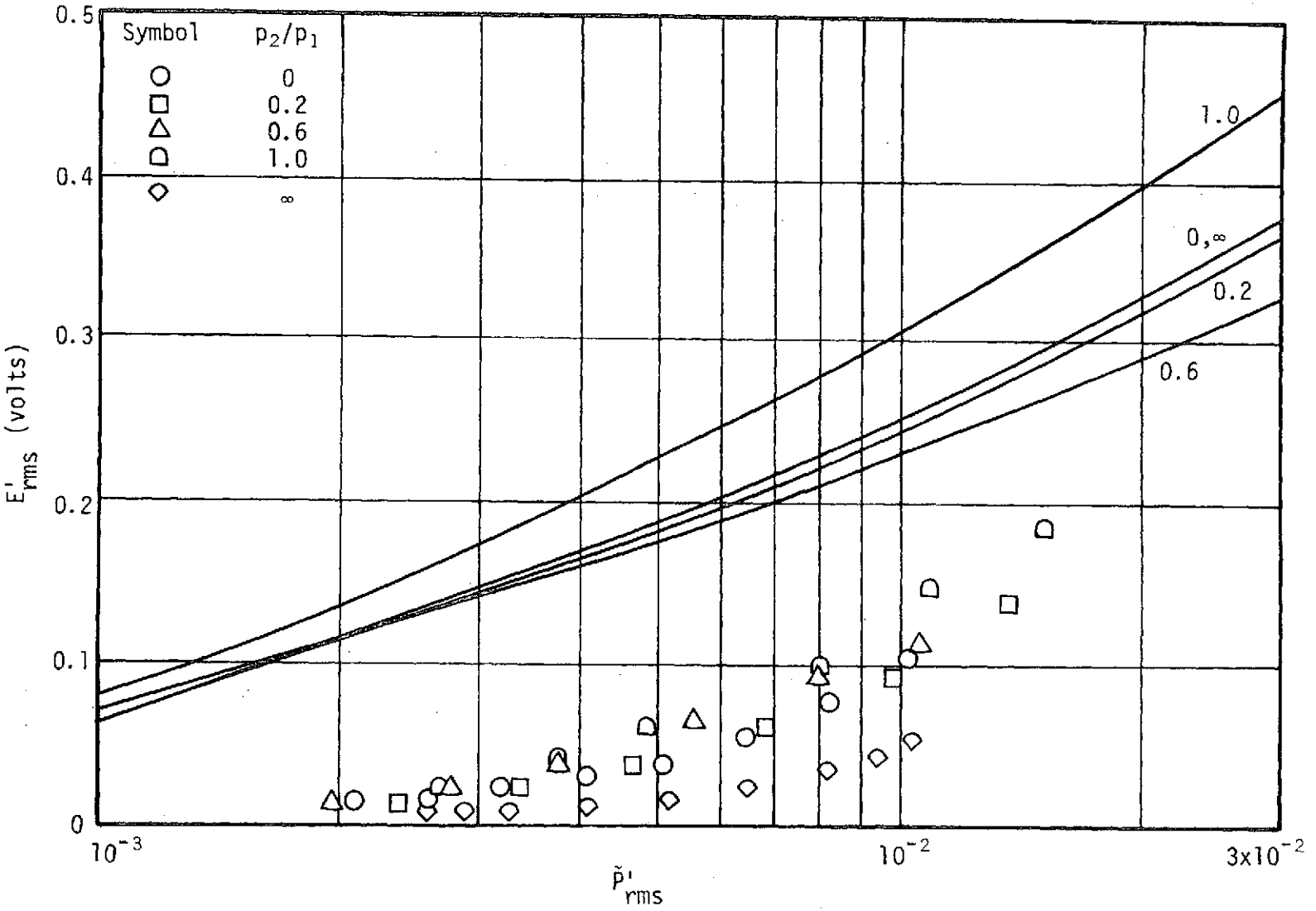

Figure 39. Analytical and Experimental Values of E'_{rms} Versus $\tilde{P}'_{rms}$ for Various Ratios of p_2/p_1; M = 0, $\phi_1 = \phi_2 = \theta_1 = \theta_2 = 0$, $T_w - T_\infty = 111.0$ K°

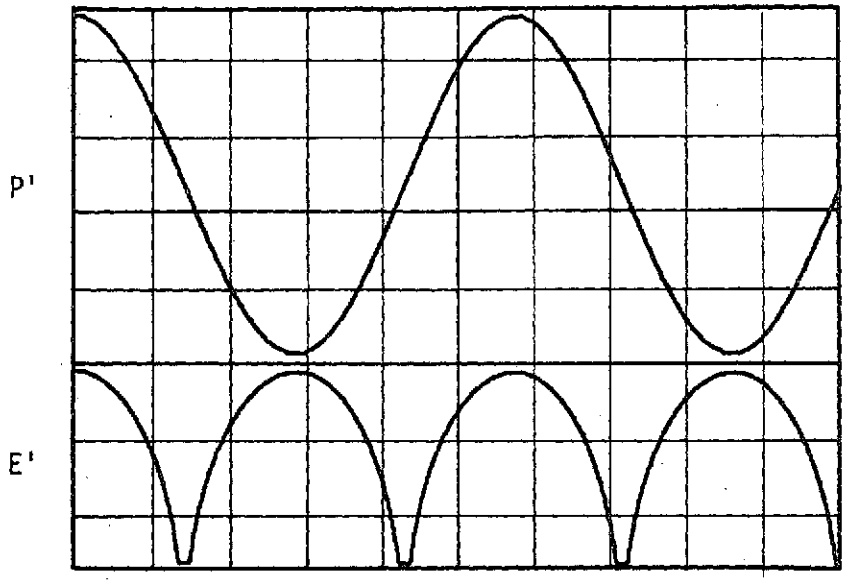

Analytical

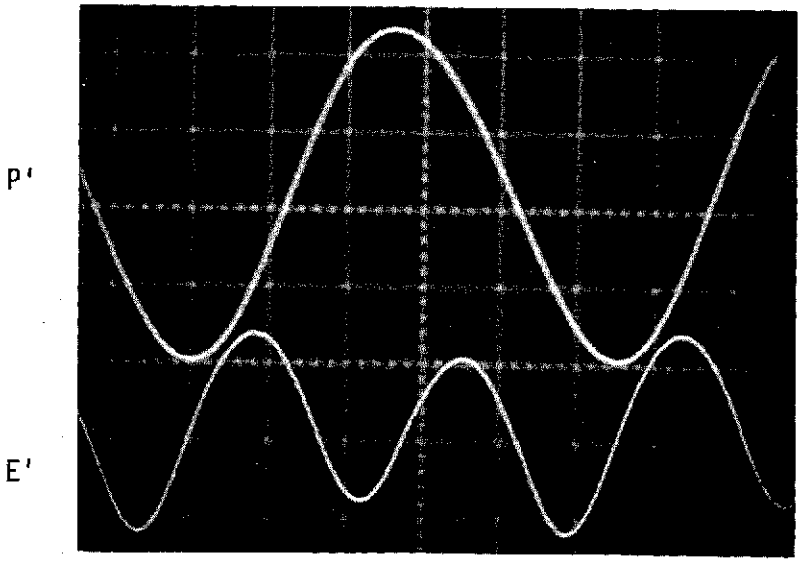

Experimental

Figure 40. Analytical and Experimental Microphone and Anemometer Waveforms for the (100) Spinning Mode

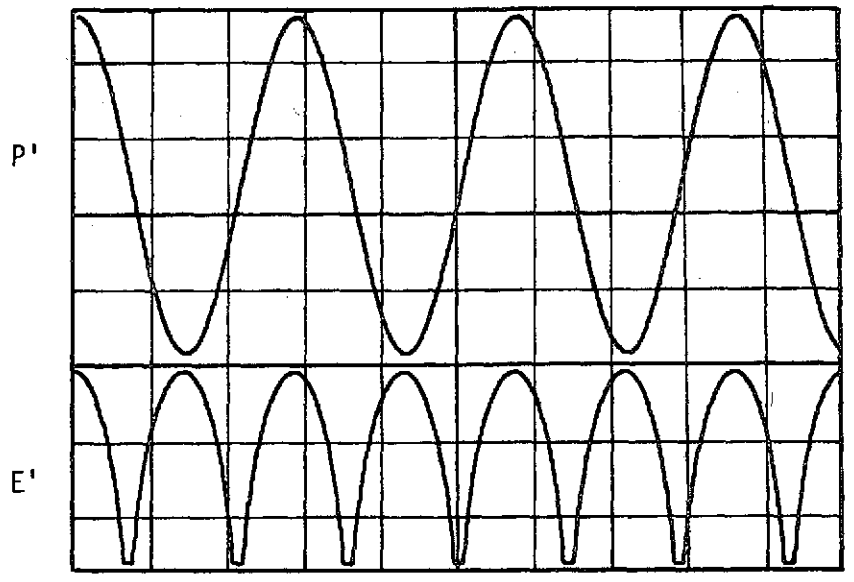

Analytical

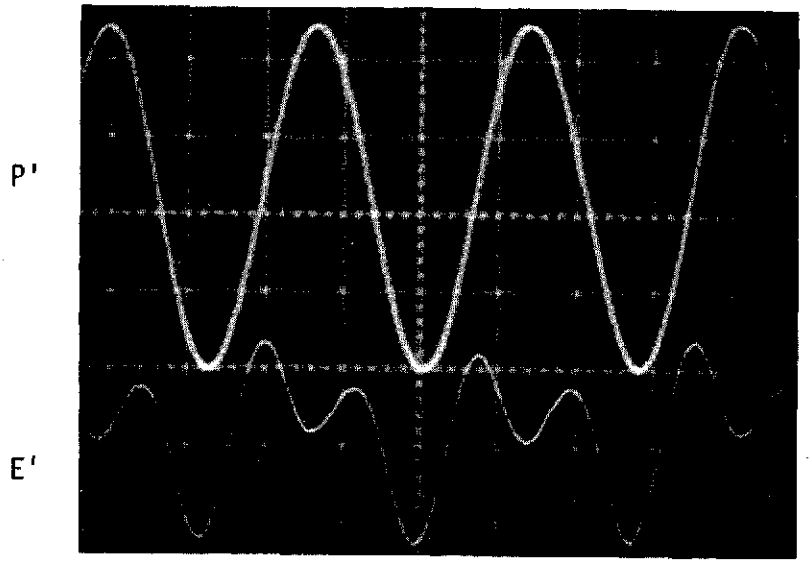

Experimental

Figure 41. Analytical and Experimental Microphone and Anemometer Waveforms for the (202) Spinning Mode

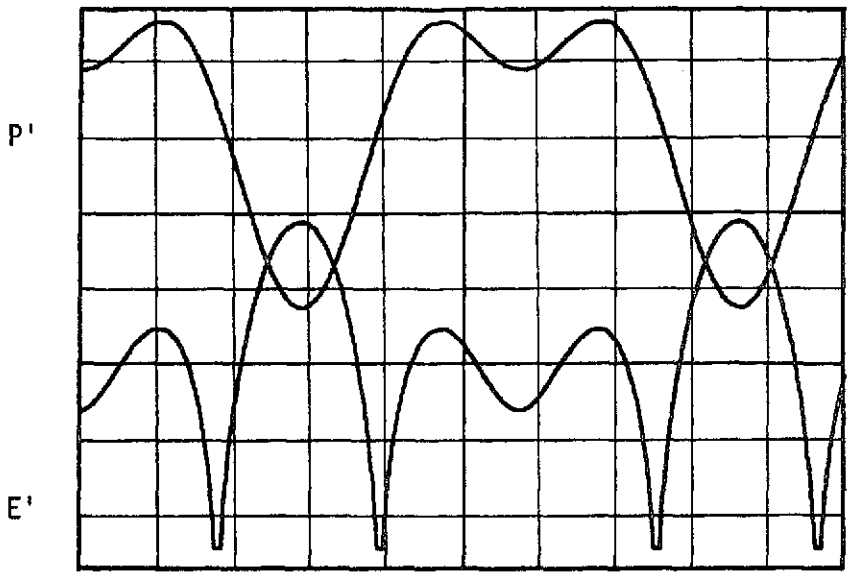

Analytical

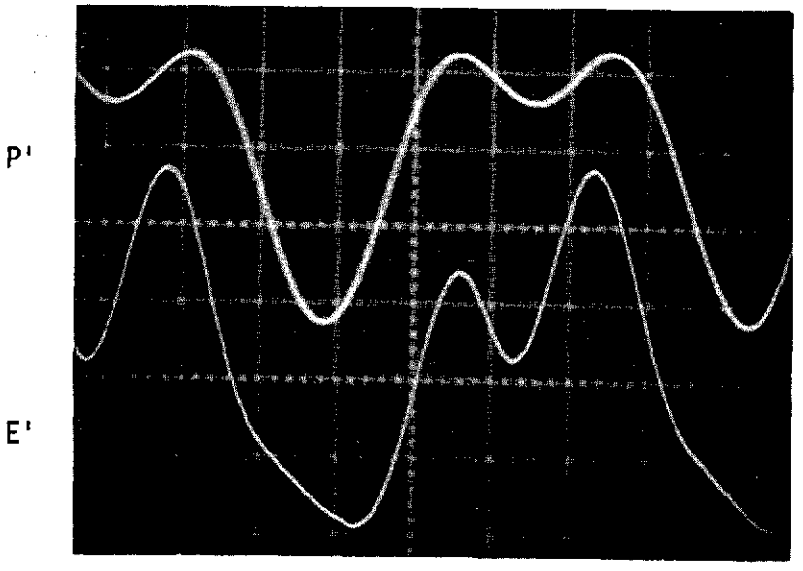

Experimental

Figure 42. Analytical and Experimental Microphone and Anemometer Waveforms for the Combined (100) plus (202) Modes with $p_2/p_1 = 0.6$, $\phi_1 = \phi_2 = \theta_1 = \theta_2 = 0$

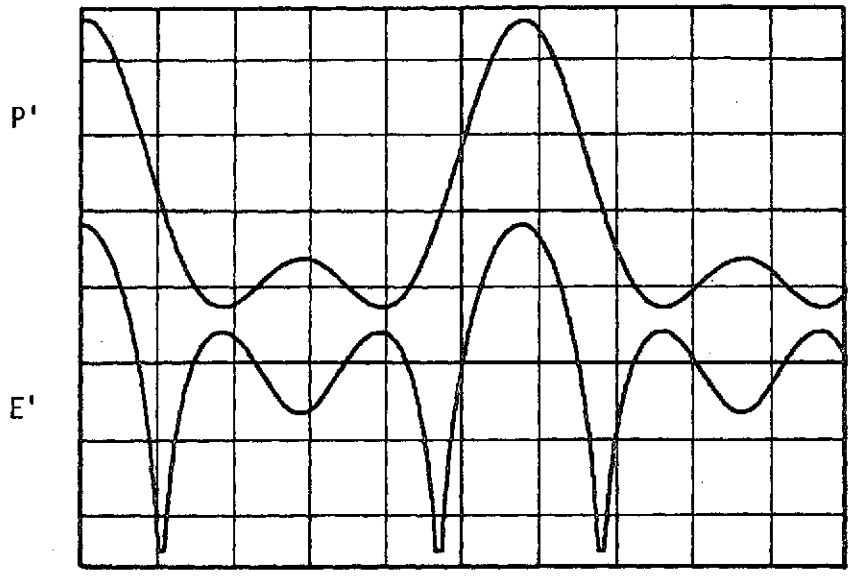

Analytical

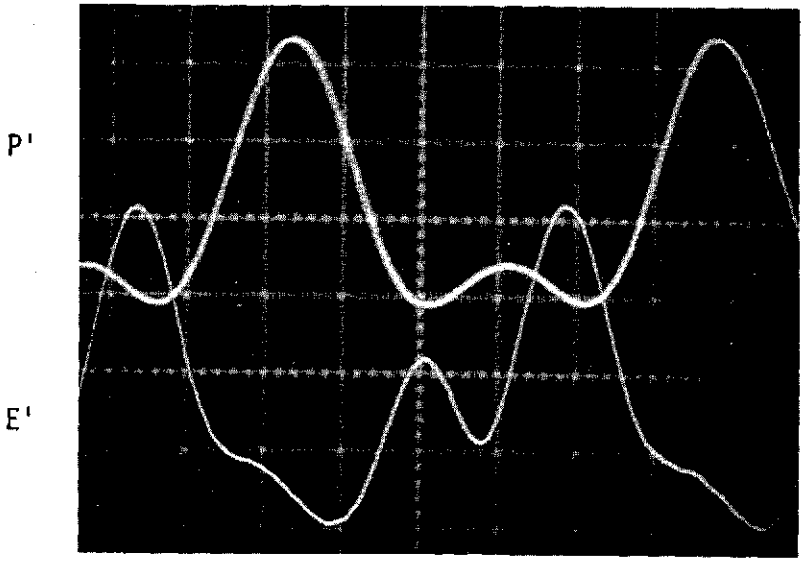

Experimental

Figure 43. Analytical and Experimental Microphone and Anemometer Waveforms for the Combined (100) plus (202) Modes with $p_2/p_1 = 0.6$, $\phi_1 = \theta_1 = \theta_2 = 0$ and $\phi_2 = 180°$

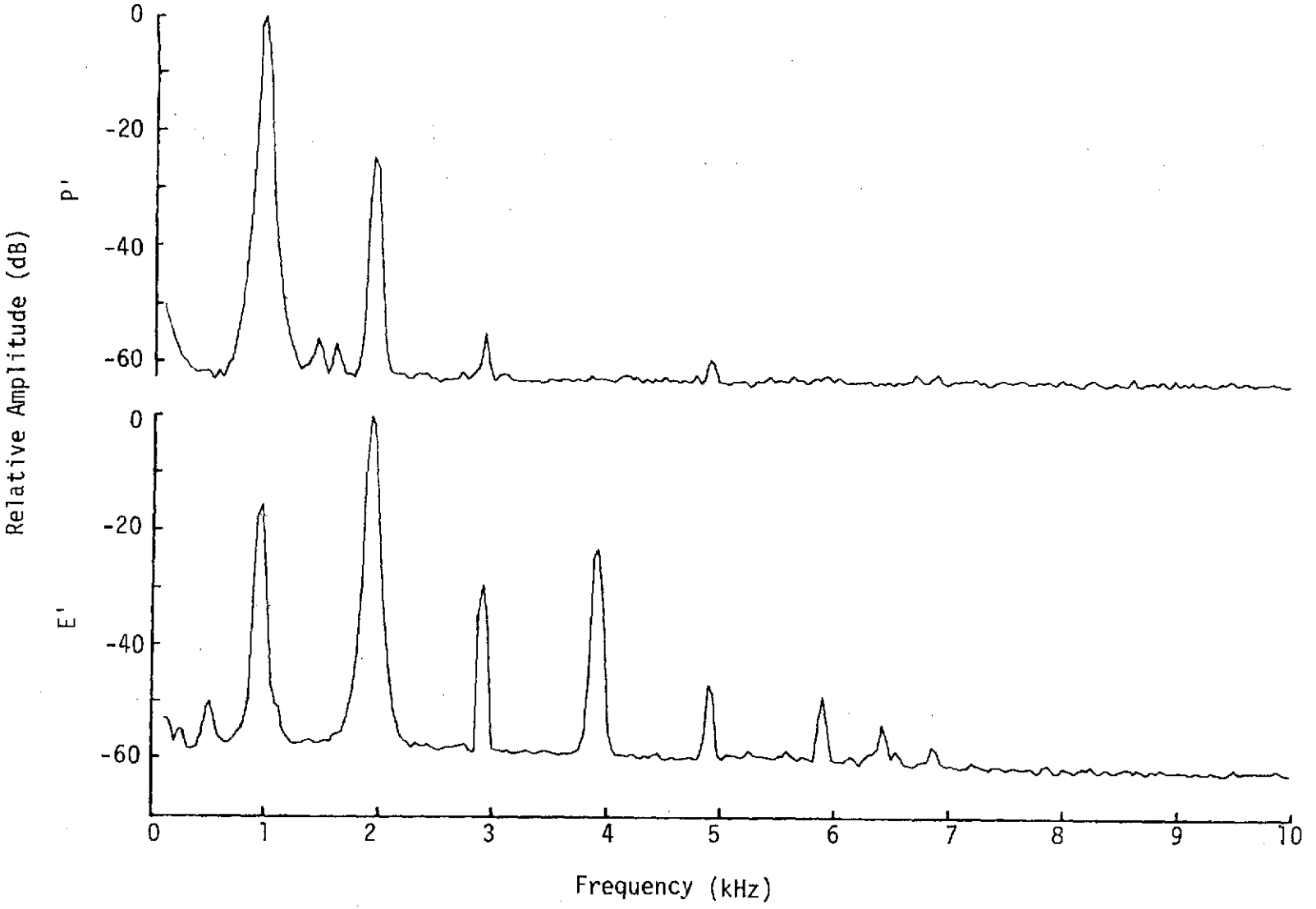

Figure 44. Frequency Analysis of the Microphone and Anemometer Signals for the (100) Spinning Mode

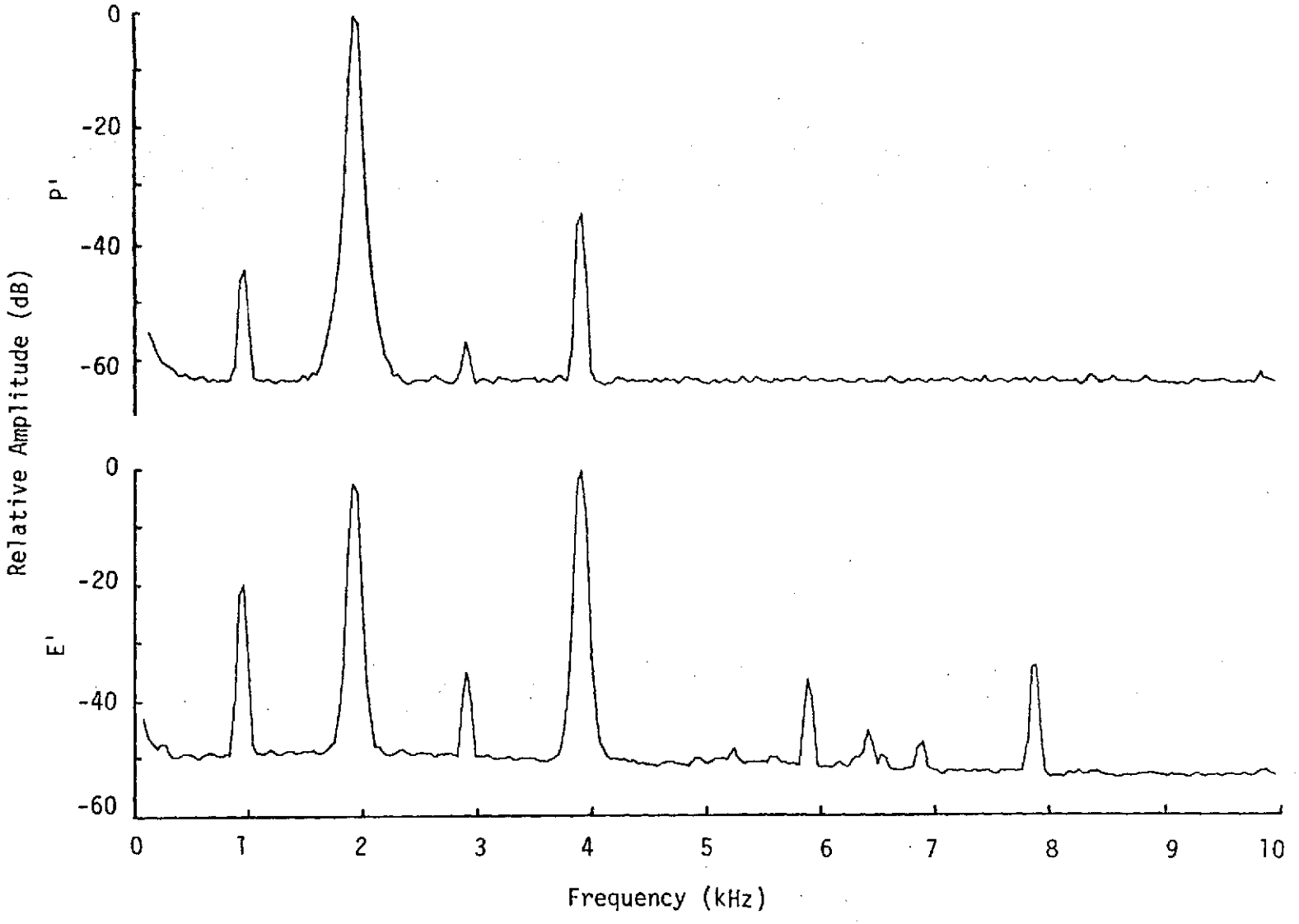

Figure 45. Frequency Analysis of the Microphone and Anemometer Signals for the (202) Spinning Mode

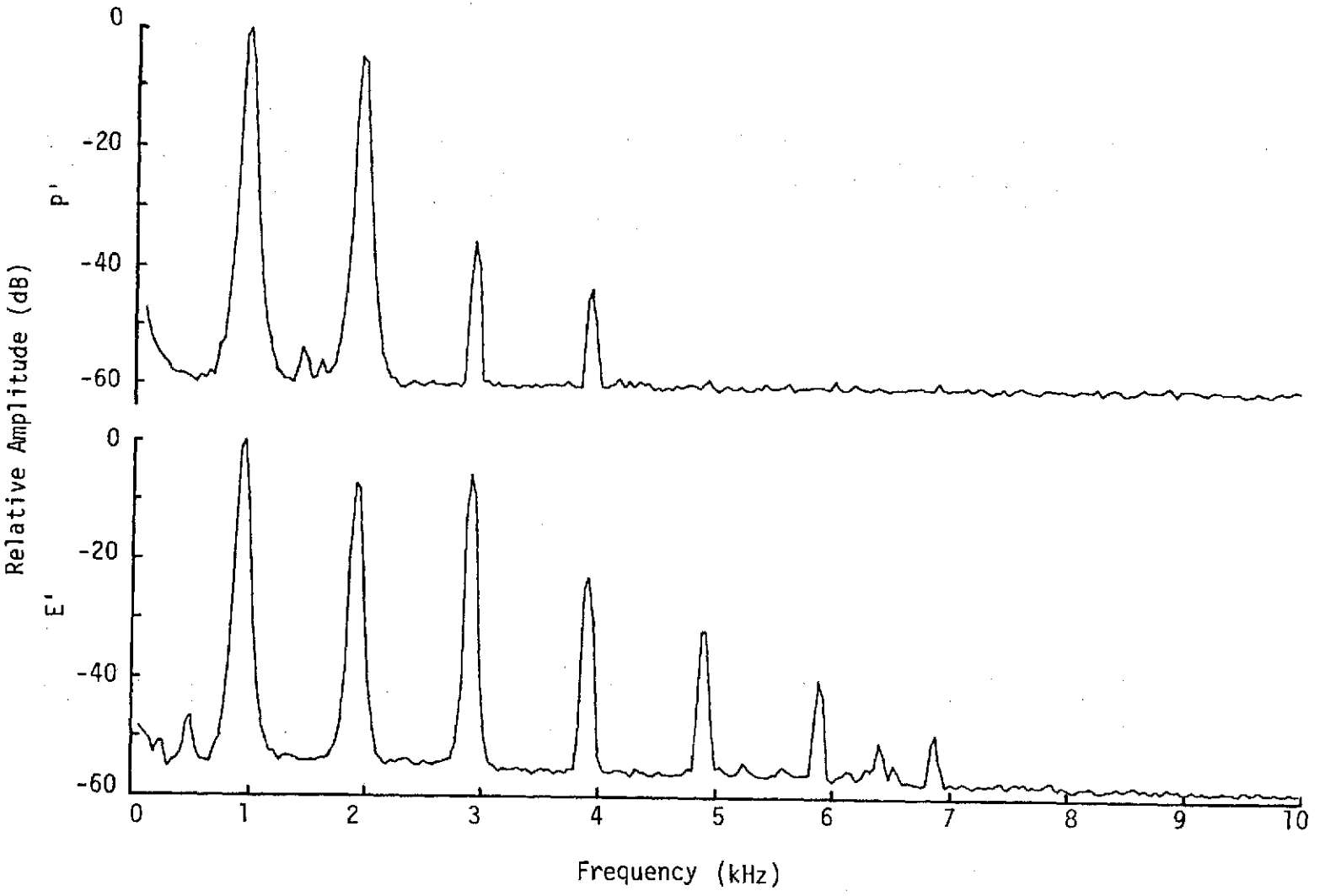

Figure 46. Frequency Analysis of the Microphone and Anemometer Signals for the (100) plus (202) Combined Spinning Modes for $p_2/p_1 = 0.6$

waveforms for the (100), the (202) and the combined (100) plus (202) spinning modes.

The (100) mode microphone signal is predicted to be a pure sine wave at f_{100}. The frequency analysis of figure 44 indicates it has, in addition, a component at $2f_{100}$; however, the amplitude of this harmonic component is about 25 dB below that of the f_{100} so it is not very significant. The results of the frequency analysis of the (202) mode microphone signal, shown in figure 45, are similar, but the amplitude of the harmonic component is about 35 dB below that of the f_{202}.

The particular combined (100) plus (202) spinning mode shown in figure 46 had a ratio of p_2/p_1 of 0.6. For this ratio the sound pressure levels should differ by 4.44 dB, and this is approximately the value obtained from the frequency analysis shown in figure 46.

The velocity variations associated with the (100) mode are predicted to be sinusoidal. The anemometer acts as a nonlinear rectifier. Rectification doubles the fundamental frequency. Hence, a frequency analysis of the anemometer signal should be composed of a strong component of $2f_{100}$ plus higher harmonics. The frequency analysis of the anemometer signal presented in figure 44 shows that the expected frequencies do occur; but, in addition, there is a subharmonic component. Examination of the experimental anemometer waveform in figure 40 also indicates that its periodicity is associated with f_{100} not $2f_{100}$. The same phenomenon occurs for the (202) mode of figure 45.

The frequency associated with the anemometer signal of the combined mode should be f_{100} plus higher harmonics, as is shown in figure 46.

Response Factors

Figure 47 is a plot of the experimental values of the response factor as a function of $\tilde{P}'_{rms}$ for various amounts of harmonic content p_2/p_1. A representative set of data at each value of p_2/p_1 is displayed. This figure very clearly shows the strong effect of the distortion component on the response factor. The overall shape of these curves is similar to that which would be expected if a through flow existed in the chamber rather than the no-forced-through-flow condition which existed (see figures 9 and 10).

Figure 48 shows the effect on the response factor of changing the phase angle ϕ_2 by 180 degrees. It is a graphical display of the experimentally determined response factors with respect to P'_{rms} for p_2/p_1 equal to 0.4 and 0.6.

Figure 49 shows the variation in the response factor with respect to the phase between the fundamental (100) component and the distortion (202) component of the acoustic field for $p_2/p_1 = 0.6$. This figure illustrates the strong effect of the phase of the distortion component on the response factor. Figure 50 is the analytically determined values of $R_{n\ell}$ as a function of ϕ_2 for the same conditions as existed in figure 49. The value of ϕ_2 at which the maximum response occurs is different experimentally than it is analytically. Also, the analytical magnitudes of the response are much larger than those obtained experimentally.

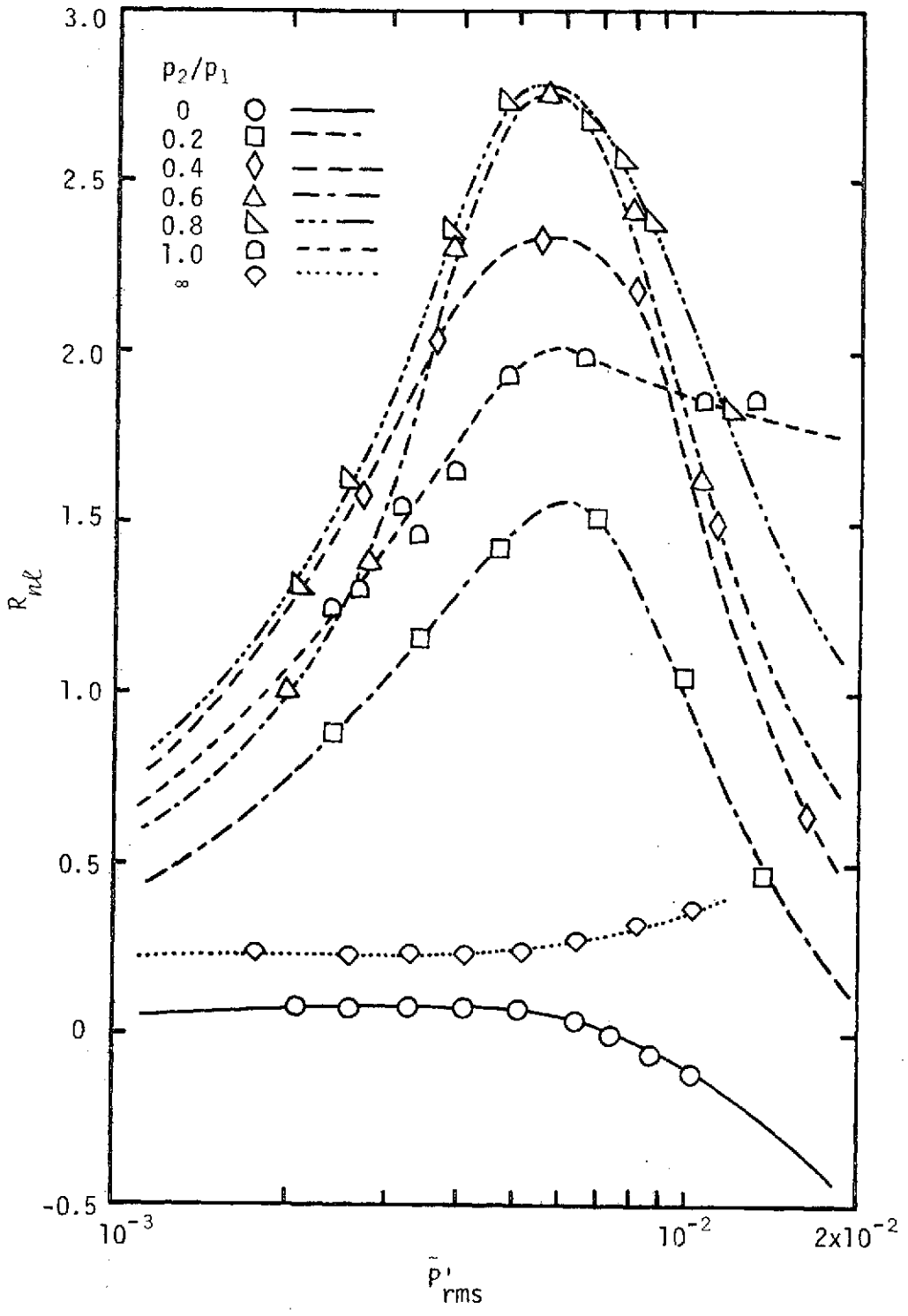

Figure 47. Experimental Response Factors Versus $\tilde{P}'_{rms}$ for Various Harmonic Contents; M = 0, $\phi_1 = \phi_2 = \theta_1 = \theta_2 = 0$, $T_w - T_\infty = 111.0$ K°

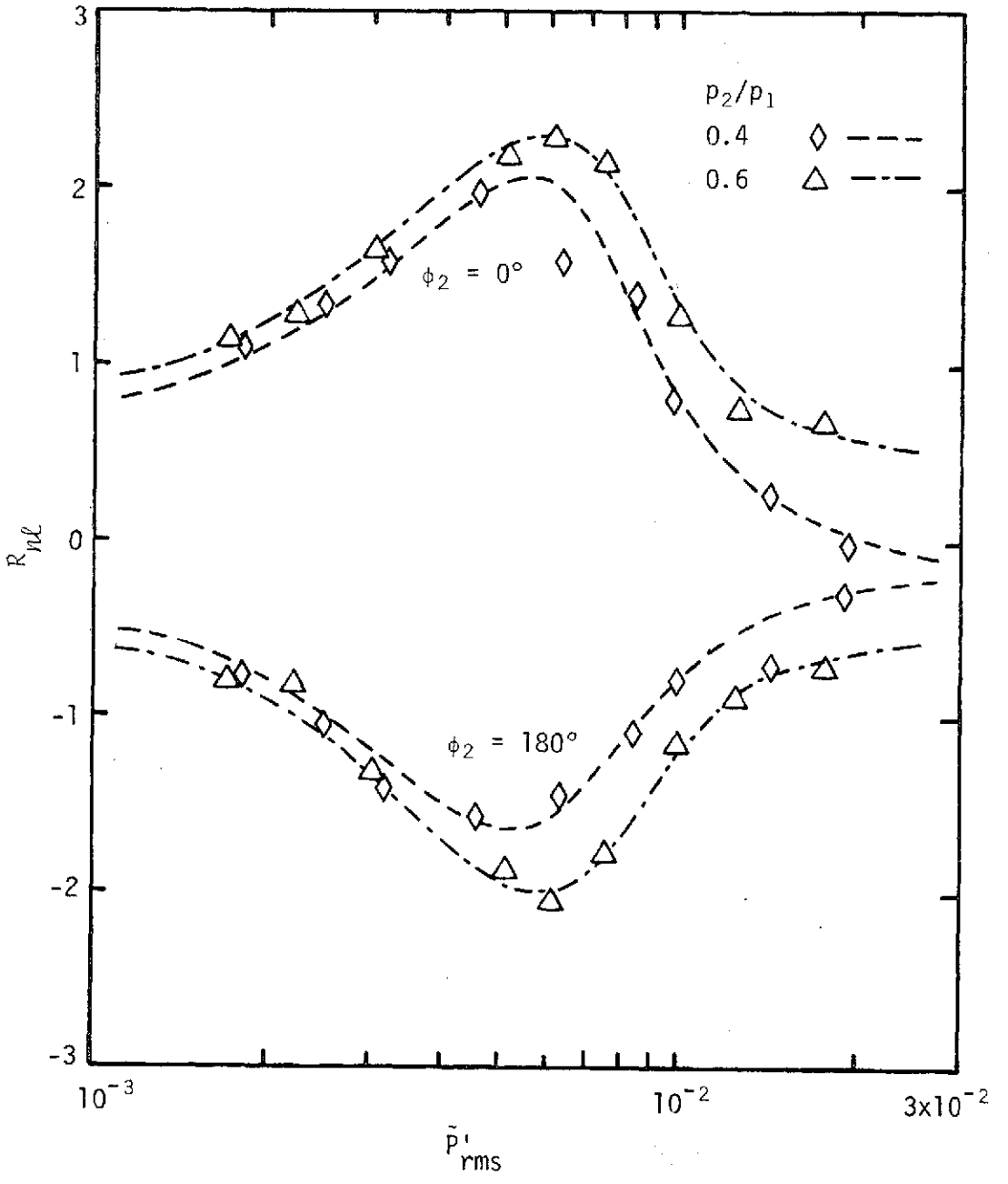

Figure 48. Experimental Response Factor Versus $\tilde{P}'_{rms}$ for ϕ_2 = 0 and 180° and p_2/p_1 = 0.4 and 0.6; M = 0, $\phi_1 = \theta_1 = \theta_2 = 0$, $T_w - T_\infty$ = 111.0 K°

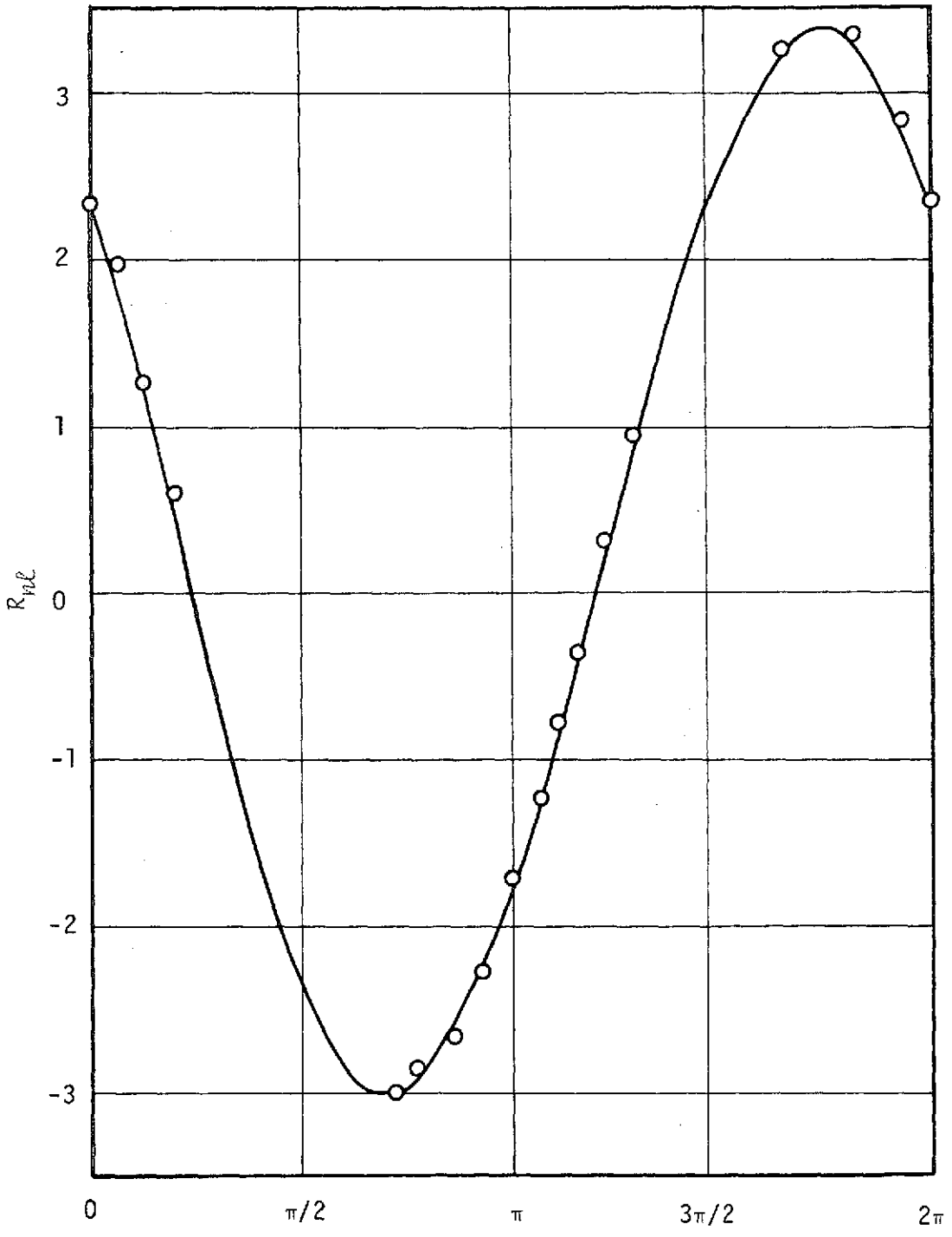

Figure 49. Experimental Response Factor Versus Phase Angle Between the (100) and (202) Modes; M = 0, $\phi_1 = \theta_1 = \theta_2 = 0$, $p_2/p_1 = 0.6$, $\tilde{P}'_{rms} = 0.0065$

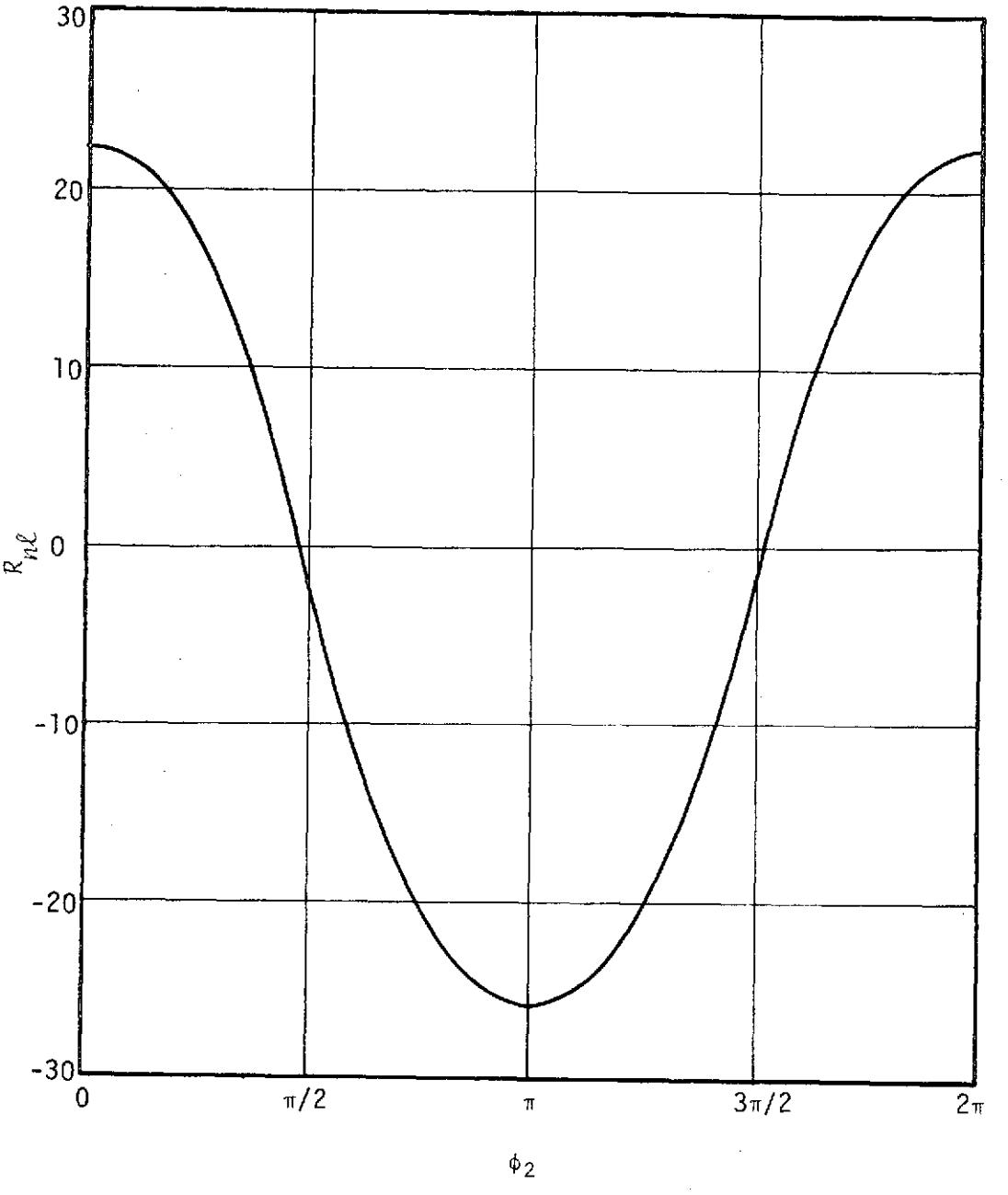

Figure 50. Analytical Response Factor Versus Phase Angle Between the (100) and (202) Modes; M = 0, $\phi_1 = \theta_1 = \theta_2 = 0$, $p_2/p_1 = 0.6$, $\tilde{P}'_{rms} = 0.0065$

Chapter 4

DISCUSSION OF THE ANALTYICAL AND EXPERIMENTAL RESULTS

INTRODUCTION

This chapter is devoted to a discussion of the analytical and experimental results. The discrepancies between the two are discussed and an extension of the results to rocket stability is made.

ANALYTICAL RESULTS

This research began with an analytical study of the response of a constant-temperature hot-wire anemometer to sinusoidal and distorted sinusoidal acoustic oscillations. This analytical study showed that the response of the anemometer is similar in nature to the response of a vaporization-limited combustion process. In both processes the amount and phase of the distortion component, relative to the fundamental component, strongly affects the response of the system. For some conditions, the addition of distortion increases the response by more than an order of magnitude above that expected for the undistorted case. The response is an estimate, obtained from open-loop studies, of the closed-loop performance of the system. Unstable closed-loop performance is definitely predicted for some cases.

The analytical study contains predictions of the anemometer's response both with and without a longitudinal component of steady flow.

The no-flow response is greater than the corresponding response with flow. This effect is especially strong at low sound pressure levels. At low values of $\tilde{P}'_{rms}$ the response for the no-flow condition increases while the corresponding response with flow decreases and tends toward zero. At high values of $\tilde{P}'_{rms}$ both the flow and no-flow situation tend to have the same behavior -- as $\tilde{P}'_{rms}$ increases, the response decreases.

EXPERIMENTAL RESULTS

An experimental system was designed and built to produce for the hot wire the same acoustic environment that was studied analytically. The results of the studies made of the acoustic fields indicate that the desired acoustic fields are being generated, but that they include some distortion. Secondary effects due to the air's viscosity (acoustic streaming) are strongly indicated.

With the experimental system, it is possible to determine a response factor for the anemometer when the hot wire is exposed to various acoustic fields. The results of the response studies show that both the amount and phase of the distortion component of the acoustic field, relative to the fundamental component, strongly affect the response of the system. For some conditions the addition of distortion increases the response by more than an order of magnitude above that obtained for the undistorted case.

Discrepancies

In spite of qualitative agreement, a number of major differences exist between theory and experiment; they are:

- The variation in $R_{n\ell}$ as a function of $\tilde{P}'_{rms}$ resembles that associated with the through-flow case, not the no-flow case.

- The magnitudes of $R_{n\ell}$ are not as large as predicted.
- E'_{rms} is much smaller than predicted.
- The anemometer signal waveforms are not as predicted; there are both phase and amplitude distortions.
- The maximum value of $R_{n\ell}$ does not appear to occur at the value of ϕ_2 predicted by analysis.

As a group, the discrepancies suggest possible explanations of the results.

Acoustic streaming. The shape of the $R_{n\ell}$ versus $\tilde{P}'_{rms}$ curves strongly suggests the presence of a constant flow over the wire. Hribar [8] has shown that when a standing (101) or (201) acoustic field exists in the air in an open ended cylindrical chamber, large standing vortices develop in the chamber. These vortices are not predicted by nonviscous theory but result when viscous effects are included in the governing equations. The vortices are a secondary flow effect. They do not significantly affect the time-dependent pressure and velocity distributions predicted by nonviscous theory. The velocities associated with these vortices (acoustic streaming) are analytically predicted to be an order of magnitude less than that associated with the time-dependent velocities resulting from the nonviscous solution. There is also likely to be acoustic streaming associated with the presence of the hot-wire probe.

The addition of a time-mean tangential acoustic streaming velocity to the velocity predicted by the nonviscous solution would have an effect similar to that associated with a flow through the chamber. The acoustic streaming velocity would add a time-mean tangential velocity to the velocity field; axial flow through the chamber adds a time-mean

longitudinal component to the velocity field. The streaming velocity would alter the nature of the response so that $R_{n\ell}$ as a function of P'_{rms} would take on the general shape associated with through-flow velocities.

Temperature effects. If a standing (100) acoustic field were to be set up in the chamber, and a hot-wire probe placed at a velocity node, the anemometer should not detect a time-dependent velocity. When this is actually carried out, an apparent low level velocity is detected at the (100) frequency. As stated earlier, velocities are rectified by the hot wire; an oscillating velocity associated with the (100) mode is expected to have a fundamental frequency of $2f_{100}$.

For a standing (100) acoustic field, a pressure, and therefore a temperature antinode exists at a velocity node. As the anemometer equations indicate, the anemometer is sensitive to temperature fluctuations. Because of this, what may look like a velocity fluctuation may actually be a temperature fluctuation. A temperature fluctuation due to a (100) acoustic field would occur at f_{100}.

If the hot wire were actually sensing the time-dependent tangential velocity associated with the spinning (100) acoustic field, plus a time-mean tangential velocity due to the acoustic streaming, plus an oscillating "velocity" due to temperature fluctuations, and the relative magnitudes of these were of the proper value, the output of the anemometer would have a waveform similar to that actually obtained for the (100) spinning acoustic field (see figure 40).

Effect of $\bar{E}$ on E'_{rms}. The value of E'_{rms} is affected when a constant flow exists over the wire because of the nonlinear nature of the anemometer. For example, referring to figure 34, the change in E

resulting from a change in velocity from zero to one meter per second is greater than the change in E resulting from a change in velocity from one to two meters per second. As the constant velocity increases, the value of E'_{rms} associated with a fluctuating velocity, whose magnitude is remaining constant, decreases.

Equipment limitations. The operating characteristics of the equipment also affects the microphone and anemometer outputs and, therefore, the response. Phase shifts in the microphone could cause the signal at one frequency to be shifted relative to the signal at the other; hence, the microphone signal which appears on an oscilloscope to be that associated with ϕ_2 equal to zero may actually be associated with another value of ϕ_2. This effect could be why the maximum value of the experimentally determined response occurs at $\phi_2 \approx -45°$ (figure 49) when analytically the maximum value of the response occurs at $\phi_2 = 0$ (figure 50). Some experiments on the microphone system were carried out to determine the phase shifts associated with the frequencies of interest; however, nothing conclusive was obtained from these investigations.

The response of the anemometer may also be inadequate at the low levels of velocity being considered. The anemometer instruction manual [21] contains a graph which shows the amplitude and phase lag as a function of frequency for various time-mean velocities. Using this graph, it can be estimated that there is a phase lag of about ten degrees for a frequency of 1000 Hz and a phase lag of about twenty degrees for a frequency of 2000 Hz. When these phase lags are converted to time delays, the delay time for each signal is the same; hence, the

signal is delayed in time, but not distorted. This time delay effect would cause the peaks of the anemometer signal to be shifted relative to the peaks of the microphone signal. The same graph indicates there may be some amplitude distortion; however, the lowest velocity listed is ten meters per second so an actual value cannot be estimated with accuracy.

The combined effect of both microphone and anemometer phase shifts and/or time lags would result in an uncertainty about the value of ϕ_2, the possibility that the microphone and anemometer signals being correlated do not originate at the same time and distortion of the P' and E' waveforms. All of these factors would tend to reduce the resulting value of $R_{n\ell}$.

Limitations of the theory. In addition to all the above factors, it is also a possibility that the theoretical development itself is not entirely valid. In theory the velocity passes through zero twice during each cycle. The "zero" velocity region during steady-state, steady-flow operation is free convection dominated. The equations were developed for forced convection heat transfer from the wire. Also, the assumption was made that the steady-state, steady-flow calibration equation of a hot wire could be applied to an unsteady situation if the instantaneous values of the fluid properties were used on the calibration equation. This assumption may not be valid for this extreme application of the hot-wire anemometer.

The above discussions present possible explanations of the experimental observations. They are aspects of this study which should be explored during future investigations.

Significance to Rocket Stability

The results obtained indicate why, when an instability occurs in a rocket engine, a sinusoidally varying time-dependent velocity component of the sound-pressure field very rapidly becomes characterized by a fundamental frequency distorted by the second harmonic frequency.

The frequency spectrum analyses of figures 48, 49 and 50 indicate how a feed back mechanism may develop which will allow an initially sinusoidal disturbance to become a distorted sine which can increase in intensity very rapidly. First, the chamber will respond much more strongly to its resonant frequencies than to other frequencies. (This was demonstrated by the resonant frequency analysis performed as part of this research.) It is able to pick out and respond to its resonant frequencies from a spectrum of frequencies which may exist in the chamber. When the chamber responds to f_{100}, a signal with a strong $2f_{100}$ frequency component results from the anemometer. If this signal is fed back into the chamber, the chamber will respond strongly to it since it is at the (202) resonant frequency. The anemometer output resulting from the combined (100) plus (202) acoustic fields has strong components at both the f_{100} and $2f_{100}$ frequencies. If this signal is then fed back into the chamber, the intensity of both the (100) and the (202) acoustic fields will be amplified. This loop, under proper feed-back conditions, would very quickly build up the sound field to a very high intensity.

Whatever secondary effects are found to occur in the chamber studied here would also tend to occur in a rocket combustion chamber. The proposed description of the feedback mechanism for amplifying an instability would also apply to the closed-loop situation in a rocket engine.

Chapter 5

CONCLUSIONS AND RECOMMENDATIONS

INTRODUCTION

An analytical and experimental investigation of the effect of sinusoidal and distorted sinusoidal acoustic perturbations on a Reynolds number dependent process has been made. In both the analysis and the experiment, the Reynolds number dependent process examined was the response of a constant-temperature hot-wire anemometer. Before the experimental investigation of the anemometer's response could be carried out, an experimental system had to be developed and tested to determine if it could produce for the hot wire the same environment examined analytically.

Since there were differences between the analytical and experimental data, some recommendations are made for further studies which may clarify the reasons for the differences. In addition, recommendations are made for extensions of this research.

CONCLUSIONS

1. The results of the analytical investigation of the response of a constant-temperature hot-wire anemometer to a sound field show that the anemometer's response is qualitatively the same as that predicted for vaporization limited combustion -- the addition of distortion to sinusoidal perturbations of the environment of a hot wire can increase

the response significantly, and the relative magnitude and phase of the distortion component are predicted to be the dominant variables in determining the response.

2. The experimental investigation shows that it is possible to set up a physical system which can generate the same acoustic environment for a hot-wire probe that was investigated analytically and which can be used to determine the response of the hot-wire bridge voltage to that environment.

3. Investigations performed with the experimental system show that the relative amplitude and phase of the distortion component of the hot wire's environment very strongly affect the response; the distortion component can increase the response by an order of magnitude above that for the undistorted case.

4. The distorted acoustic fields generated cannot be totally characterized by the equations resulting from the solution of the inviscid wave equation. Viscous effects should be included in the analysis in order to account for acoustic streaming and any other secondary phenomena which may occur.

5. The assumption that the steady-state, steady-flow calibration equation of a hot wire can be applied to an unsteady situation, if the the instantaneous values of the fluid properties are used in the calibration equation, may not be valid.

6. A feedback and amplification process is possible when two resonant frequencies exist in a chamber such that the one resonant frequency is twice that of the other.

RECOMMENDATIONS

1. More extensive investigations of the acoustic fields in a cylindrical chamber need to be performed with special attention being given to acoustic streaming phenomena and temperature fluctuations.

2. An investigation of the limitations on the assumption that the steady-state, steady-flow calibration equation of a hot wire can be applied to an unsteady situation, if the instantaneous values of the fluid properties are used in the calibration equation, needs to be carried out.

3. The dynamic behavior of the anemometer needs to be examined in more detail, especially with regard to E'_{rms}.

4. The dynamic behavior of the microphone needs to be examined in more detail.

5. More data of the type reported herein need to be taken and analyzed.

6. Data should be taken for other wire locations and orientations to establish how the response varies with chamber location.

7. An analytical study of the effect of various length to diameter ratios on the resonant frequencies of the chamber should be performed since the resonant frequencies that are multiples of lower mode frequencies affect the response.

8. A theoretical analysis needs to be done which will quantitatively relate the experimental results obtained for the constant-temperature hot-wire anemometer to the results to be expected for vaporization-limited combustion.

9. A closed-loop system should be designed with which it can be determined if the open-loop predictions of the closed-loop performance are valid.

REFERENCES

LIST OF REFERENCES

1. Priem, R. J. and M. F. Heidmann, "Propellant Vaporization as a Design Criterion for Rocket Engine Combustion Chambers," NASA TR R-67, 1960.

2. Heidmann, M. F., "Amplification by Wave Distortion in Unstable Combustors," AIAA Journal, Vol. 9, No. 2, Feb. 1971, p. 336.

3. Heidmann, M. F., "Amplification by Wave Distortion of the Dynamic Response of Vaporization Limited Combustion," NASA TN D-6287, May, 1971.

4. Sotter, J. C. and G. A. Flandro, "Resonant Combustion in Rockets," Sci. Am., Vol. 219, No. 6, Dec. 1968.

5. Conrad, E. W., H. E. Blommer, J. P. Wanhainen, and D. W. Vincent, "Interim Summary of Liquid Rocket Acoustic-Mode-Instability Studies at a Nominal Thrust of 20,000 Pounds," NASA TN D-4968, Dec. 1968.

6. Harrje, D. T. and F. H. Reardon, editors, Liquid Propellant Rocket Combustion Instability, NASA SP-194, 1972.

7. Rayleigh, J. W. S., The Theory of Sound, Dover, New York, 1945, Vol. 2, p. 226.

8. Hribar, A. E., "The Effect of a Transverse Resonant Acoustic Field Upon Viscous Fluid In a Cylindrical Enclosure," Ph.D. Thesis, Purdue University, 1969.

9. Osborn, J. R. and J. M. Bonnell, "Transverse Modes of Acoustic Oscillations," Jet Propulsion Center, Purdue University, Report No. TM-64-4, June 1964.

10. Osborn, J. R. and J. R. Rahon, "Effects of Radial Energy Releast Variations on Transverse Combustion Pressure Oscillations," Jet Propulsion Center, Purdue University, I-62-3, March 1962.

11. Heidmann, M. F. and P. R. Wieber, "Analysis of Frequency Response Characteristics of Propellant Vaporization," NASA TN D-3749, Dec. 1966.

12. Priem, R. J. and D. C. Guentert, "Combustion Instability Limits Determined by a Nonlinear Theory and a One-Dimensional Model," NASA TN D-1409, 1962.

13. Priem, R. J., "Influence of Combustion Process on Stability," NASA TN D-2957, Aug. 1965.

14. Purdy, K. R., M. B. Ventrice and J. C. Fang, "An Analytical Investigation of the Open-Loop Amplification of Reynolds Number Dependent Processes by Wave Distortion," Proceedings of the Tenth Annual Southeastern Seminar on Thermal Sciences, 1974.

15. King, L. V., "On the Convective Heat Transfer from Small Cylinders in a Stream of Fluid. Determination of Convective Constants of Small Platinum Wires with Application to Hot-Wire Anemometry," Phil. Trans. R. Soc., Vol. 214A, 1914.

16. Andrews, G. E., D. Bradley and G. F. Hundy, "Hot-Wire Anemometer Calibration for Measurements of Small Gas Velocities," Int. J. Heat Mass Transfer, Vol. 15, 1972, pp. 1765-1785.

17. Collis, D. C. and M. J. Williams, "Two Dimensional Convection from Heated Wires at Low Reynolds Numbers," J. of Heat Transfer, Vol. 6, 1969, pp. 357-384.

18. Hilsenrath, J., et. al., Tables of Thermal Properties of Gases, National Bureau of Standards, Circular 564, Nov. 1955.

19. Purdy, K. R., G. W. Simmons, A. E. Hribar and E. I. Griggs, "Acoustically Augmented Convective Drying," Sonochemical Engineering, Vol. 67, 1971, pp. 55-67.

20. Fang, J. C. and K. R. Purdy, "Calibration of a Constant-Temperature Hot-Wire Anemometer for Very Low Reynolds Numbers," ME-44 Report, Department of Mechanical Engineering, Tennessee Technological University, 1973.

21. DISA, "Constant Temperature Anemometer Instruction Manual for Type 55A01."

22. Purdy, K. R., "Viscous Fluid Flow Under the Influence of a Resonant Acoustic Field," Ph.D. Thesis, School of Mechanical Engineering, Georgia Institute of Technology, 1963.

23. Morse, P. M., Vibrations and Sound, Second edition, McGraw-Hill Book Co., Inc., New York, 1948.

24. Abramowitz, M and I. A. Stegun, editors, Handbook of Mathematical Functions, National Bureau of Standards, Applied Mathematics Series No. 55, 1964.

25. DISA, "Instruction and Service Manual for Type 55D41/42 Calibration Equipment."

APPENDICES

APPENDIX A

SOLUTION OF THE INVISCID WAVE EQUATION

PROBLEM STATEMENT

The system being analyzed is shown in figure A1.

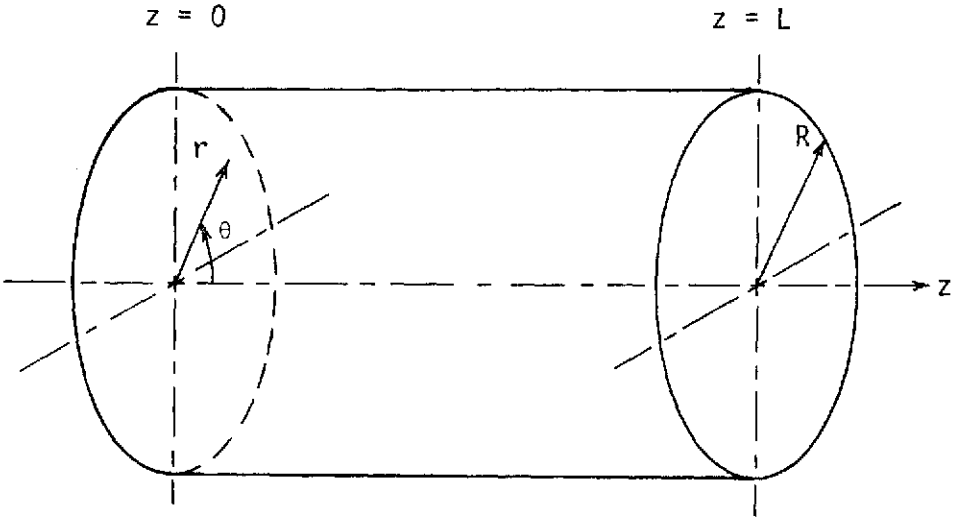

Figure A1. System Model

It consists of a cylinder of length L and radius R which is closed at both ends and contains an ideal gas. The following assumptions are made about the system:

- The gaseous medium is in a uniform state except for weak isentropic fluctuations in the state properties and velocity caused by the acoustic field.
- There is no heat transfer.
- There is no mass flow into or out of the cylindrical enclosure.

The governing equations are:

- Continuity

$$\frac{\partial \rho}{\partial t} + \nabla \cdot (\rho \vec{V}) = 0 \tag{A.1}$$

- Momentum

$$\rho \frac{D\vec{V}}{Dt} = -\nabla P \tag{A.2}$$

- Equation of State

$$P = \rho R_g T \tag{A.3}$$

- Second Law of Thermodynamics

$$s = \text{constant} \tag{A.4}$$

Since the gas is inviscid, a velocity potential can be defined

$$\nabla \Phi \equiv \vec{V} \tag{A.5}$$

Introducing this definition into the governing equations yields a non-homogeneous wave equation for the velocity potential

$$\nabla^2 \Phi - \frac{1}{c_\infty^2} \frac{\partial^2 \Phi}{\partial t^2} = g(\Phi) \tag{A.6}$$

It can be shown that the terms composing $g(\phi)$ are at least an order of magnitude smaller than the left-hand side of equation (A.6). A detailed order of magnitude analysis demonstrating this for the one-dimensional case is given by Purdy [22] and a further discussion can be found in Morse [23].

In accordance with the first assumption, the velocity, density and pressure can be expressed as the sum of a time-mean and a time-

dependent component as follows:

$$\vec{V}(r,\theta,z,t) = \bar{\vec{V}}(r,\theta,z) + \vec{V}'(r,\theta,z,t)$$

$$\rho(r,\theta,z,t) = \bar{\rho}(r,\theta,z) + \rho'(r,\theta,z,t)$$

$$P(r,\theta,z,t) = \bar{P}(r,\theta,z) + P'(r,\theta,z,t) \qquad (A.7)$$

where the bar overscore denotes the time-mean value and the prime denotes the deviation from the mean value.

The isentropic speed of sound for an ideal gas is

$$c^2 \equiv \left.\frac{\partial P}{\partial \rho}\right|_s = \gamma R_g T = \gamma P/\rho \qquad (A.8)$$

The speed of sound in equation (A.6), c_∞, is based on the "undisturbed" property values -- the property values when $\vec{V}(r,\theta,z,t) = 0$.
Thus

$$c_\infty^2 = k P_\infty/\rho_\infty \qquad (A.9)$$

The velocity potential is related to the acoustic velocity, pressure and density such that

$$\vec{V}' = \nabla\Phi \qquad (A.10)$$

$$P' = -\rho_\infty \frac{\partial\Phi}{\partial t} \qquad (A.11)$$

$$\rho' = -\frac{\rho_\infty}{c_\infty^2} \frac{\partial\Phi}{\partial t} \qquad (A.12)$$

The boundary conditions are:

- Acoustic pressure P' is finite at r = 0, or

$$\frac{\partial\phi(0,\theta,z,t)}{\partial t} = \text{finite} \tag{A.13}$$

- Radial acoustic particle velocity is zero at the cylinder walls (r = R), or

$$\frac{\partial\phi(R,\theta,z,t)}{\partial r} = 0 \tag{A.14}$$

- For closed ends the longitudinal acoustic particle velocity is zero at the cylinder ends (z = 0,L), or

$$\frac{\partial\Phi(r,\theta,0,t)}{\partial z} = \frac{\partial\Phi(r,\theta,L,t)}{\partial z} = 0 \tag{A.15}$$

In cylindrical coordinates, the wave equation to be solved is

$$\frac{1}{r}\,\frac{\partial(r\,\frac{\partial\Phi}{\partial r})}{\partial r} + \frac{1}{r^2}\,\frac{\partial^2\Phi}{\partial\theta^2} + \frac{\partial^2\Phi}{\partial z^2} - \frac{1}{c_\infty{}^2}\,\frac{\partial^2\Phi}{\partial t^2} = 0 \tag{A.16}$$

Assuming that the velocity potential can be expressed as

$$\Phi(r,\theta,z,t) = \text{Real}[\phi(r,\theta,z)e^{i\omega t}] \tag{A.17}$$

substituting equation (A.17) into equation (A.16) and simplifying, yields the Helmholtz equation for $\phi(r,\theta,z)$,

$$\nabla^2\phi + k^2\phi = 0 \tag{A.18}$$

where

$$k^2 = \omega^2/c_\infty{}^2 \tag{A.19}$$

Equation (A.18) can be solved using the method of separation

of variables. Assuming that

$$\phi(r,\theta,z) = \Gamma(r,\theta)\Lambda(z) \tag{A.20}$$

substituting equation (A.20) into equation (A.18), separating variables and using the arbitrary constant k_z^2, yields the following two equations:

$$\frac{\partial^2 \Lambda}{\partial z^2} + k_z^2 \Lambda = 0 \tag{A.21}$$

$$r \frac{(r \frac{\partial \Gamma}{\partial r})}{\partial r} + \frac{\partial^2 \Gamma}{\partial \theta^2} + (k^2 - k_z^2) r^2 \Gamma = 0 \tag{A.22}$$

The solution of equation (A.21) is

$$\Lambda(z) = A \cos(k_z z) + B \sin(k_z z) \tag{A.23}$$

Equation (A.22) is a function of two variables. Letting

$$\Gamma(r,\theta) = \Omega(r)T(\theta) \tag{A.24}$$

Substituting equation (A.26) into equation (A.24), separating variables and using the arbitrary constant m^2, yields

$$\frac{\partial^2 T}{\partial \theta^2} + m^2 T = 0 \tag{A.25}$$

and

$$\frac{\partial^2 \Omega}{\partial r^2} + \frac{1}{r} \frac{\partial \Omega}{\partial r} + (k^2 - k_z^2 - \frac{m^2}{r^2})\Omega = 0 \tag{A.26}$$

The solution of equation (A.25) is

$$T(\theta) = C \cos(m\theta) + D \sin(m\theta) \tag{A.27}$$

where m can take on only integer values since otherwise $T(\theta)$ would be multiple valued.

Equation (A.26) can be put in the form of Bessel's equation. Letting

$$k_r^2 = k^2 - k_z^2$$

$$r = x/k_r$$

$$y = \Omega(r) \tag{A.28}$$

equation (A.26) becomes

$$x^2 \frac{\partial^2 y}{\partial x^2} + x \frac{\partial y}{\partial x} + (x^2 - m^2)y = 0 \tag{A.29}$$

which is Bessel's equation of order m. The solution is [24]:

$$y = F\, J_m(x) + G Y_n(x) \text{ for m an integer} \tag{A.30}$$

where

$J_m(x)$ = Bessel functions of the first kind of order m and

$Y_m(x)$ = Bessel functions of the second kind of order m or Weber functions

Converting back to the original variables, equation (A.30) becomes

$$\Omega(r) = F\, J_m(k_r r) + G\, Y_m(k_r r) \tag{A.31}$$

Combining equations (A.17), (A.20), (A.23), (A.27) and (A.31) gives

$$\Phi(r,\theta,z,t) = \text{Real}\left\{[F\,J_m(k_r r) + G\,Y_m(k_r r)][C\cos(m\theta + D\sin(m\theta)] \cdot [A\cos(k_z z) + B\sin(k_z z)]e^{i\omega t}\right\} \tag{A.32}$$

Application of the first boundary condition, equation (A.15), requires that $G = 0$ since $Y_m(k_r r) \to -\infty$ as $r \to 0$.

Application of the second boundary condition, equation (A.16), requires that

$$J_m'(k_r R) = 0 \tag{A.33}$$

J_m' is almost a periodic function; therefore the eigen values of equation (A.33) will be defined as $\alpha_{mn}\,\pi$,

$$k_r R \equiv \alpha_{mn}\,\pi$$

$$k_r = \alpha_{mn}\,\pi/R\,; \quad m,n = 0,1,2,\ldots \tag{A.34}$$

For each value of m, there is a series of solutions which satisfy equation (A.34); the symbol n is used to distinguish these.

Application of the third boundary condition, a pressure node at $z = 0,L$, requires $B = 0$ and $\sin(k_z L) = 0$ -- a solution can be obtained only for the eigenvalues

$$k_z = n_z\,\pi/L\,; \quad n_z = 0,1,2,\ldots \tag{A.35}$$

Substituting the above results into equation (A.32) and combining constants yields

$$\Phi(r,\theta,z,t) = \text{Real}\left\{J_m(\alpha_{mn}\pi r/R)\, C_{mnn_z}\cos(m\theta) + D_{mnn_z}\sin(m\theta)]\cdot \cos(n_z\pi z/L)e^{i\omega t}\right\} \quad (A.36)$$

Extracting the real part of equation (A.36) and recognizing that for a linear equation the sum of the solutions is also a solution and that ω depends on the values of m, n and n_z, the general solution of the inviscid wave equation is

$$\Phi(r,\theta,z,t) = \sum_{m,n,n_z} J_m(\alpha_{mn}\pi r/R)\cos(n_z\pi z/L)[A_{mnn_z}\cos(m\theta + \omega_{mnn_z}t+\zeta_{mnn_z}) + B_{mnn_z}\cos(m\theta-\omega_{mnn_z}t-\eta_{mnn_z})] \quad (A.37)$$

where A_{mnn_z} and B_{mnn_z} are constants which are associated with particular values of m, n and n_z and ζ_{mnn_z} and η_{mnn_z} are arbitrary phase angles also associated with particular values of m, n and n_z.

The resonant frequencies of oscillation are specified by the eigenvalues of the solution. Using the relation $\omega = 2\pi f$, equations (A.19), (A.28), (A.34) and (A.35) yield

$$f_{mnn_z} = \frac{\omega_{mnn_z}}{2\pi} = \frac{c_\infty}{2}\left[\left(\frac{\alpha_{mn}}{R}\right)^2 + \left(\frac{n_z}{L}\right)^2\right]^{0.5} \quad (A.38)$$

This specifies all possible resonant frequencies.

The solution, equation (A.37), can be put in the form of a standing wave or a spinning wave.

STANDING WAVE SOLUTION

In equation (A.37) the last term on the right-hand side is the sum of two traveling waves, one moving in the positive θ direction, the other moving in the negative θ direction. To form a standing wave the amplitudes of the two must either be equal, $A_{mnn_z} = B_{mnn_z}$ with $\zeta_{mnn_z} = \eta_{mnn_z}$ or of opposite sign, $A_{mnn_z} = B_{mnn_z}$ with $\zeta_{mnn_z} = \eta_{mnn_z} \pm \pi$. Assuming $A_{mnn_z} = B_{mnnz}$, equation (A.37) can be put into simpler form, namely

$$\Phi(r,\theta,z,t) = \sum_{mnn_z} G_{mnn_z} J_m(\alpha_{mn}\pi r/R)\cos(n_z\pi z/L)$$

$$\cos(m\theta)\cos(\omega_{mnn_z} t + \beta_{mnn_z}) \qquad (A.39)$$

where G_{mnn_z} are constants and the β_{mnn_z} are arbitrary phase angles associated with particular values of m, n and n_z.

Using equations (A.39) and (A.11) a general term for P' is

$$P'_{mnn_z} = \rho_\infty \omega_{mnn_z} G_{mnn_z} J_m(\alpha_{mn}\pi r/R)\cos(n_z\pi z/L)$$

$$\cos(m\theta)\sin(\omega_{mnn_z} t + \beta_{mnn_z}) \qquad (A.40)$$

Letting the maximum value of P'_{mnn_z} for a particular (mnn_z) mode be $\hat{P}_{mnn_z}$, i.e.,

$$\hat{P}_{mnn_z} = \rho_\infty \omega_{mnn_z} G_{mnn_z} J_m(\alpha_{mn}\pi) \qquad (A.41)$$

solving equation (A.41) for G_{mnn_z}

$$G_{mnn_z} = \frac{\hat{P}_{mnn_z}}{\rho_\infty \omega_{mnn_z} J_m(\alpha_{mn}\pi)} \tag{A.42}$$

and substituting equation (A.42) into equation (A.39), but considering only the general term, gives

$$\Phi_{mnn_z}(r,\theta,z,t) = \frac{\hat{P}_{mnn_z}}{\rho_\infty \omega_{mnn_z}} \frac{J_m(\alpha_{mn}\pi r/R)}{J_m(\alpha_{mn}\pi)} \cos(n_z \pi z/L)$$

$$\cos(m\theta)\cos(\omega_{mnn_z} t + \beta_{mnn_z}) \tag{A.43}$$

Using equation (A.43), general terms for the acoustic pressure, velocity and density are:

$$P'_{mnn_z} = \hat{P}_{mnn_z} \frac{J_m(\alpha_{mn}\pi r/R)}{J_m(\alpha_{mn}\pi)} \cos(n_z \pi z/L)\cos(m\theta)\sin(\omega_{mnn_z} t + \beta_{mnn_z}) \tag{A.44a}$$

$$V'_{r_{mnn_z}} = \frac{\hat{P}_{mnn_z} \alpha_{mn}\pi}{\rho_\infty \omega_{mnn_z} r} \frac{J'_m(\alpha_{mn}\pi r/R)}{J_m(\alpha_{mn}\pi)} \cos(n_z \pi z/L)\cos(m\theta)$$

$$\cos(\omega_{mnn_z} t + \beta_{mnn_z}) \tag{A.44b}$$

$$V'_{\theta_{mnn_z}} = -\frac{\hat{P}_{mnn_z} m}{\rho_\infty \omega_{mnn_z} r} \frac{J_m(\alpha_{mn}\pi r/R)}{J_m(\alpha_{mn}\pi)} \cos(n_z \pi z/L)\sin(m\theta)$$

$$\cos(\omega_{mnn_z} t + \beta_{mnn_z}) \tag{A.44c}$$

$$V'_{z_{mnn_z}} = -\frac{\hat{P}_{mnn_z} n_z \pi}{\rho_\infty \omega_{mnn_z} L} \frac{J_m(\alpha_{mn}\pi r/R)}{J_m(\alpha_{mn}\pi)} \sin(n_z\pi z/L)\cos(m\theta)$$

$$\cos(\omega_{mnn_z} t + \beta_{mnn_z}) \qquad \text{(A.44d)}$$

$$\rho'_{mnn_z} = \frac{\hat{P}_{mnn_z}}{c_\infty^2} \frac{J_m(\alpha_{mn}\pi r/R)}{J_m(\alpha_{mn}\pi)} \cos(n_z\pi z/L)\cos(m\theta)$$

$$\cos(\omega_{mnn_z} t + \beta_{mnn_z}) \qquad \text{(A.44e)}$$

SPINNING WAVE SOLUTION

As stated earlier, the general solution of the inviscid wave equation, equation (A.37), is actually the sum of two traveling waves -- one moving in the positive θ direction, the other in the negative θ direction. Since the waves move tangentially the terminology "spinning" is used. Setting A_{mnn_z} equal to zero in equation (A.37) yields a solution composed of traveling waves which spin in the positive direction, namely

$$\bar{\Phi}(r,\theta,z,t) = \sum_{mnn_z} J_m(\alpha_{mn}\pi r/R)\cos(n_z\pi z/L)$$

$$B_{mnn_z} \cos(m\theta - \omega_{mnn_z} t - \eta_{mnn_z}) \qquad \text{(A.45)}$$

In this form the interchangability of the effect of changes in either time or angular position can be seen.

Trigonometric transformation of the last term of equation (A.45) yields

$$\Phi(r,\theta,z,t) \sum_{mnn_z} J_m(\alpha_{mn}\pi r/R)\cos(n_z\pi z/L)$$

$$B_{mnn_z}[\cos(m\theta)\cos(\omega_{mnn_z}t + \eta_{mnn_z})$$

$$- \sin(m\theta)\sin(\omega_{mnn_z}t + \eta_{mnn_z})] \qquad (A.46)$$

Equation (A.46) is in the form of the sum of two standing waves; hence, a spinning wave can be considered to be composed of two standing waves of equal amplitude, but 90/m degrees out of phase with each other in angular position and 90 degrees out of phase with respect to time. This is a useful concept for experimental work.

Following a procedure similar to that used for the standing case, the general term for the velocity potential is

$$\Phi_{mnn_z}(r,\theta,z,t) = \frac{\hat{P}_{mnn_z}}{\rho_\infty \omega_{mnn_z}} \frac{J_m(\alpha_{mn}\pi r/R)}{J_m(\alpha_{mn}\pi)} \cos(n_z\pi z/L)$$

$$\cos(m\theta - \omega_{mnn_z}t - \eta_{mnn_z}) \qquad (A.47)$$

and the general terms for the acoustic pressure, velocity and density are:

$$P'_{mnn_z} = \hat{P}_{mnn_z} \frac{J_m(\alpha_{mn}\pi r/R)}{J_m(\alpha_{mn}\pi)} \cos(n_z\pi z/L)\sin(m\theta$$

$$- \omega_{mnn_z}t - \eta_{mnn_z}) \qquad (A.48a)$$

$$V'_{r_{mnn_z}} = \frac{\hat{P}_{mnn_z}\alpha_{mn}\pi}{\rho_\infty \omega_{mnn_z} R} \frac{J_m'(\alpha_{mn}\pi r/R)}{J_m(\alpha_{mn}\pi)} \cos(n_z\pi z/L)\cos(m\theta$$

$$- \omega_{mnn_z} t - \eta_{mnn_z}) \qquad \text{(A.48b)}$$

$$V'_{\theta_{mnn_z}} = - \frac{\hat{P}_{mnn_z} m}{\rho_\infty \omega_{mnn_z} r} \frac{J_m(\alpha_{mn}\pi r/R)}{J_m(\alpha_{mn}\pi)} \cos(n_z\pi z/L)\sin(m\theta$$

$$- \omega_{mnn_z} t - \eta_{mnn_z}) \qquad \text{(A.48c)}$$

$$V'_{z_{mnn_z}} = - \frac{\hat{P}_{mnn_z} n_z\pi}{\rho_\infty \omega_{mnn_z} L} \frac{J_m(\alpha_{mn}\pi r/R)}{J_m(\alpha_{mn}\pi)} \sin(n_z\pi z/L)\cos(m\theta$$

$$- \omega_{mnn_z} t - \eta_{mnn_z}) \qquad \text{(A.48d)}$$

$$\rho'_{mnn_z} = \frac{\hat{P}_{mnn_z}}{c_\infty^2} \frac{J_m(\alpha_{mn}\pi r/R)}{J_m(\alpha_{mn}\pi)} \cos(n_z\pi z/L)\sin(m\theta$$

$$- \omega_{mnn_z} t - \eta_{mnn_z}) \qquad \text{(A.48e)}$$

APPENDIX B

SELECTED VALUES OF α_{mn}

The resonant frequencies of a closed-ended cylindrical chamber depend on the eigenvalues of equation (A.33),

$$J_m'(k_r R) = 0 \tag{A.33}$$

Since J_m' is almost a periodic function, the eigenvalues of equation (A.33) are defined as $\alpha_{mn}\pi$; thus

$$k_r R \equiv \alpha_{mn}\pi \tag{A.34}$$

Substituting equation (A.34) into equation (A.33) gives

$$J_m'(\alpha_{mn}\pi) = 0 \tag{B.1}$$

For each value of m there is a series of solutions which satisfy equation (B.1) -- the symbol n is used to distinguish these. Table B.1 lists values of α_{mn}.

Table B.1. α_{mn}

m	n = 0	n = 1	n = 2	n = 3	n = 4
0	0.0000	1.2197	2.2331	3.2383	4.2411
1	0.5861	1.6970	2.7140	3.7261	4.7312
2	0.9722	2.1346	3.1734	4.1923	5.2036
3	1.3373	2.5513	3.6115	4.6428	5.6624
4	1.6926	2.9547	4.0368	5.0815	6.1103
5	2.0421	3.3486	4.4523	5.5108	6.5494
6	2.3877	3.7353	4.8600	5.9325	6.9811
7	2.7304	4.1165	5.2615	6.3477	7.4065
8	3.0709	4.4931	5.6576	6.7574	7.8264

APPENDIX C

HOT WIRE CALIBRATION RESULTS

The equation which relates the velocity of flow over a hot wire to the voltage output from a constant temperature hot-wire anemometer associated with it is given by equation (2.17)

$$E = \left\{\left[\hat{A} + \hat{B}\ Re_{f_1}{}^{N}(\tilde{V}^2)^{N/2}\right]\left[\frac{T_f}{T_\infty}\right]^{0.17}\left[\frac{T_f}{T_o}\right]^{0.877}[T_w - T]\right\}^{0.5} \quad (2.17)$$

For the steady-state, steady-flow conditions which exist during wire calibration, all quantities in equation (2.17) are constant except the velocity; hence, equation (2.17) reduces to

$$E = [A + B\ \tilde{V}^N]^{0.5} \quad (2.18)$$

where

$$A = \hat{A}\left[\frac{T_f}{T_\infty}\right]^{0.17}\left[\frac{T_f}{T_o}\right]^{0.877}[T_w - T] \quad (2.19a)$$

and

$$B = \hat{B}\ Re_{f_1}{}^{N}\left[\frac{T_f}{T_\infty}\right]^{0.17}\left[\frac{T_f}{T_o}\right]^{0.877}[T_w - T] \quad (2.19b)$$

For steady-state, steady-flow conditions, $T = T_\infty$ and $P = P_\infty$.

During the calibration of a wire, the voltage output from the anemometer and the corresponding pressure drop across the nozzle of the

wind tunnel in which the wire is located is obtained. The equipment and procedure used to do this is described in Chapter 3. For the equipment described, the pressure drop across the nozzle of the wind tunnel is measured as the amplified analog voltage of an MKS Baratron pressure transducer. The voltage so obtained is converted, with a calibration constant determined by experiment, to a pressure difference. Table C.1 lists the data and resulting pressure difference obtained during a calibration of the wire. The calibration constant which relates H to ΔP is

$$H/\Delta P = 122.58 \text{ volts/inch-of-water}$$

Table C.1. Hot-Wire Calibration Data

Anemometer Output E (volts)	Baratron Output H (volts)	Pressure Drop ΔP (in. of H_2O)	Velocity V (m/sec)
3.8160	0.0314	0	0
4.0235	0.0472	0.000129	0.235328
4.1374	0.0722	0.000334	0.378676
4.2289	0.1048	0.000601	0.507979
4.2973	0.1386	0.000878	0.613984
4.3823	0.2055	0.001427	0.782736
4.4535	0.2854	0.002082	0.945472
4.5156	0.3825	0.002878	1.111608
4.5755	0.4992	0.003834	1.283022
4.6397	0.6392	0.004982	1.462545
4.6975	0.8254	0.006508	1.671596
4.7459	0.9882	0.007842	1.834936
4.7864	1.1914	0.009508	2.020472
4.8177	1.2817	0.010248	2.097624

The velocity of the air passing over the wire in the nozzle of the wind tunnel can be determined with the following formula [25]:

$$V = \left(\frac{2\gamma}{\gamma-1}\right) R_a \, T\left[1 - \left(1 - \frac{\Delta P}{P}\right)^{(\gamma-1)/\gamma}\right] \tag{3.13}$$

This velocity is also shown in Table C.1.

Using the information given in Table C.1 and the least-squares curve-fitting procedure described in Chapter 3, the constants A, B and N are found to be

$$A = 11.909$$

$$B = 9.0995$$

$$N = 0.444$$

with a goodness-of-fit of 0.99988. (The data at a velocity of zero are not used since the equations were developed for forced-convective heat transfer and, at zero velocity, free-convective heat transfer is dominant.)

The following additional data were also recorded:

$$R_\infty = 4.02\ \Omega$$

$$R_w = 5.42\ \Omega$$

$$T_\infty = 275°K$$

$$P_\infty = 736.79\ \text{mm Hg}$$

$$D_w = 5 \times 10^{-6}\ \text{m}$$

The temperature of the wire T_w can be found from

$$R_w = R_\infty + \alpha\,[T_w - T_\infty] \tag{2.7}$$

where $\alpha = 0.0126\ \Omega/K°$.

The film temperature is determined from its definition

$$T_f = (T_w + T)/2 \tag{C.1}$$

The quantity Re_{f_1} is

$$Re_{f_1} = \frac{\rho\ V_1\ D_w}{R_a\ T_f\ \mu_o [T_f/T_o]^{0.757}} \tag{2.14}$$

From the ideal gas equation

$$\rho = \frac{P}{R_a T} \tag{2.10}$$

where

$$R_a = 287.1\ m^2/sec^2\text{-}K°$$

From Hilsenrath [18]

$$\mu_o = 1.716 \times 10^{-5}\ Kg/m\text{-}sec$$

Combining equations (2.19) with equations (2.7), (C.1), (2.14), (2.10) and the values of A, B, R_∞, R_w, T_∞, P_∞, D_w, α, R_a and μ_o, the values of $\hat{A}$ and $\hat{B}$ become

$$\hat{A} = 0.5205$$

$$\hat{B} = 0.6729$$

Substituting A, B and N into equation (2.17) yields

$$E = \left\{ \left[0.525 + 0.6729\ Re_{f_1}^{0.444} (\tilde{V}^2)^{0.222} \right] \left[\frac{T_f}{T_\infty} \right]^{0.17} \left[\frac{T_f}{T_o} \right]^{0.877} [T_w - T] \right\}^{0.5} \tag{C.2}$$

VITA

The author [redacted] and attended Allentown public schools, graduating from high school in 1958. In the fall of that year she entered the Pennsylvania State University in the mechanical engineering curriculum. In January of 1960 she married Carl A. Ventrice, then became a part-time student and in 1961 quit school completely.

In January of 1965 she returned to school as a full-time student in the Department of Engineering Science of Tennessee Polytechnic Institute (later to become Tennessee Technological University) and graduated from Tech with a Bachelor of Science in Engineering Science in 1966. In January of 1967 she entered Auburn University in the Department of Mechanical Engineering, from which she received a Master of Science degree in June of 1968. She continued as a student at Auburn until August of 1968.

In September of 1968, the author became a post-master's student in the Department of Mechanical Engineering of Tennessee Technological University, and during the following year she was employed as an Instructor in the Department of Engineering Science. In September of 1971 she became a doctoral student and Graduate Instructor in the Department of Mechanical Engineering and in March of 1974 accepted a position as an Assistant Professor in that department.

The author is married to Carl A. Ventrice and has three children, Ruth, Carl, Jr. and James.

REPORT DISTRIBUTION LIST

NASA-Lewis Research Center
Attn: Dr. R. J. Priem/MS 500-204
21000 Brookpark Road
Cleveland, OH 44135
(2 copies)

NASA-Lewis Research Center
Attn: N. T. Musial/MS 500-311
21000 Brookpark Road
Cleveland, OH 44135

NASA-Lewis Research Center
Attn: Library/MS 60-3
21000 Brookpark Road
Cleveland, OH 44135

NASA-Lewis Research Center
Attn: Report Control Office/MS 5-5
2100 Brookpark Road
Cleveland, OH 44135

NASA-Lewis Research Center
Attn: E. A. Bourke/MS 500-205
21000 Brookpark Road
Cleveland, OH 44135

NASA Headquarters
Attn: RPS/Robert A. Wasel
600 Independence Ave., SW, Rm 526
Washington, D. C. 20546

NASA-Lewis Research Center
Attn: Procurement Section
Mail Stop 500-313
21000 Brookpark Road
Cleveland, OH 44135

NASA-Lyndon B. Johnson Space Center
Attn: EP/Joseph G. Thibodaux
Houston, TX 77058

NASA-George C. Marshall Space Flight Center
Attn: S&E-ASTN-PP/R. J. Richmond
Huntsville, AL 35812

NASA Scientific & Technical Information
Facility - Acquisitions Branch
P. O. Box 33
College Park, MD 20740
(10 copies)

Aerojet Liquid Rocket Company
Attn: David A. Fairchild
Bldg. 20001/Sec. 9732
P. O. Box 13222
Sacramento, CA 94813

Aerospace Corporation
Attn: O. W. Dykeman
P. O. Box 92957
Los Angeles, CA 90045

Air Force Rocket Propulsion Lab.
(RPM)
Attn: Library
Edwards, CA 93523

Air Force Office of Scientific
Research
Chief Propulsion Division
Attn: Dr. J. F. Masi (NAE)
1400 Wilson Boulevard
Arlington, VA 22209

Air Force Rocket Propulsion
Laboratory
Attn: Daweel George
Edwards, CA 93523

Air Force Rocket Propulsion
Laboratory
Attn: Richard R. Weiss
Edwards, CA 93523

AFAPL
Attn: Frank D. Stull (RJT)
Wright Patterson AFB, OH 45433

Bell Aerospace Company
Attn: T. F. Ferger
Post Office Box 1
Mail Zone, J-81
Buffalo, NY 14205

Bureau of Naval Weapons
Department of the Navy
Attn: Library
Washington, DC

Brooklyn Polytechnic Institute
Long Island Graduate Center
Attn: V. D. Agosta
Route 110
Farmingdale, NY 11735

California Institute of Technology
Jet Propulsion Laboratory
Attn: Fred E. C. Culick
4800 Oak Grove Drive
Pasadena, CA 91103

California Institute of Technology
Jet Propulsion Laboratory
Attn: Jack H. Rupe
4800 Oak Grove Drive
Pasadena, CA 91103

California State University Sacramento
School of Engineering
Attn: Frederick H. Reardon
600 J. Street
Sacramento, CA 95819

Chemical Propulsion Information Agency
Johns Hopkins University/APL
Attn: T. W. Christian
8621 Georgia Avenue
Silver Spring, MD 20910

Colorado State University
Attn: Charles E. Mitchell
Fort Collins, CO 80521

Georgia Institute of Technology
Georgia Tech. Res. Inst.
Attn: Warren C. Strahle
Atlanta, GA 30332

Georgia Institute of Technology
Georgia Tech. Res. Inst.
Attn: Ben T. Zinn
Atlanta, GA 30332

Melvin Gerstein
P. O. Box 452
Atladena, CA 91001

Massachusetts Institute of Technology
Department of Mechanical Engineering
Attn: T. Y. Toong
77 Massachusetts Avenue
Cambridge, MA 02139

McDonald Douglas Corporation
McDonnell Douglas Astronautics Co.
Attn: William T. Webber
5301 Bolsa Ave.
Huntington Beach, CA 92647

D. E. Mock
Advanced Research Projects Agency
Washington, DC 20525

Naval Postgraduate School
Department of Aeronautics
Attn: David W. Netzer
Monterey, CA 93940

Naval Weapons Center
Attn: Edward W. Price
Code 608
China Lake, CA 93555

Pennsylvania State University
Mechanical Engineering Department
Attn: G. M. Faeth
207 Mechanical Engineering Bldg.
University Park, PA 16802

Princeton University
Forrestal Campus Library
Attn: Irvin Glassman
P. O. Box 710
Princeton, NJ 08450

Princeton University
Forrestal Campus Library
Attn: David T. Harrje
P. O. Box 710
Princeton, NJ 08540

Princeton University
Forrestal Campus Library
Attn: Martin Summerfield
P. O. Box 710
Princeton, NJ 08540

Propulsion Sciences, Inc.
Attn: Vito Agosta
P. O. Box 814
Melville, NY 11746

Purdue University Res. Foundation
School of Mechanical Engineering
Attn: John R. Osborn
Thermal Sci. Propulsion Center
West Lafayette, IN 47906

Rockwell International Corp.
Rocketdyne Division
Attn: L. P. Combs, D/991-350
Zone 11
6633 Canoga Avenue
Canoga Park, CA 91304

Rockwell International Corp.
Rocketdyne Division
Attn: James A Nestlerode
Dept. 596-124, AC46
6633 Canoga Ave.
Canoga Park, CA 91304

Rockwell International Corp.
Rocketdyne Division
Attn: Carl L. Oberg
Dept. 589-197-SS11
6633 Canoga Ave.
Canoga Park, CA 91304

TISIA
Defense Documentation Center
Cameron Station, Bldg. 5
5010 Duke Street
Alexandria, VA 22314

United Aircraft Corporation
Attn: R. H. Woodward Waesche
400 Main Street
East Hartford, CT 06108

University of California
Aerospace Engineering Dept.
Attn: F. A. Williams
Post Office Box 109
LaJolla, CA 92037

University of Illinois
Aeronautics/Astronautic Engr. Dept.
Attn: R. A. Strehlow
Transportation Bldg., Room 101
Urbana, IL 61801

University of Michigan
Attn: James A. Nicholls
P. O. Box 622
Ann Arbor, MI 48107

Tennessee Technological University
Department of Mechanical Engineering
Attn: Kenneth R. Purdy
P. O. Box 5014
Cookeville, TN 38501

Textron, Inc.
Bell Aerospace, Div.
Research Department
Attn: John H. Morgenthaler, C-84
P. O. Box One
Buffalo, NY 14240

TRW Systems
Attn: G. W. Elverun
One Space Park
Redondo Beach, CA 90278

Tulane University
Attn: J. C. O'Hara
6823 St. Charles Ave.
New Orleans, LA 70118

University of Utah
Department of Chemical Engineering
Attn: Alva D. Baer
Park Bldg., Room 307
Salt Lake City, UT 84112

University of Wisconsin
Mechanical Engineering Dept.
Attn: P. S. Myers
1513 University Avenue
Madison, WI 53706

Virginia Polytechnic Institute State
University
Attn: J. A. Schetz
Blacksburg, VA 24061

Office of Assistant Director
(Chemical Technician)
Office of the Director of Defense
Research & Engineering
Washington, DC 20301